Quasi-phase-matched High-Harmonic Generation in Gas-filled Hollow-core Photonic Crystal Fibre

Amnueporn Florian Carl Lebrecht Wiegandt

Merton College, Oxford



A thesis presented for the degree of

Doctor of Philosophy

Trinity Term 2020

Supervised by

Prof. Ian A. Walmsley

Prof. Simon M. Hooker

Department of Atomic and Laser Physics

University of Oxford

United Kingdom

Quasi-phase-matched High-Harmonic Generation in Gas-filled Hollow-core Photonic Crystal Fibre

Florian Wiegandt

Merton College, Oxford

Abstract

High-order harmonic generation (HHG) provides a promising tabletop source of coherent short wavelength radiation. However, the low generation efficiency limits the mean photon flux of HHG sources when driven with low average power, kHz repetition rate lasers. The HHG flux could be increased by employing MHz repetition rate driving lasers. However, the low pulse energy necessitates tight focusing, which limits the effective interaction volume. Generating harmonics in a gas-filled photonic crystal fiber (PCF) mitigates this problem, but for both free focus and PCF targets, the HHG conversion efficiency is optimized at technologically challenging multi-bar gas pressures. In this thesis, HHG is performed with µJ-level driving pulses in hollow-core PCFs. Dramatic 160-fold enhancement of the HHG flux through a novel, time-multiplexed multi-modal quasi-phasematching technique is observed at low gas-pressures. Non-phase-matched generation of high-harmonic photon energies up to 61.6 eV with continuous spectral tunability made possible by controlled ionization-induced blue-shifting of the driving laser is presented and fully phase-matched HHG in an argon-filled PCF is explored.

Synthesized, multi-colour ultrashort pulses of light open the door to a new class of interesting experiments in atomic, molecular and optical science. Characterization of these pulses is not possible using established pulse characterization techniques, if the spectrum of the synthesized pulse exhibits extended intensity nulls, since the relative spectral phase of different spectral regions cannot be determined. In this thesis, a spectral-gap-immune pulse characterization technique is demonstrated. Two mutually coherent ultrafast pulses are derived from a Ti:Sapphire laser. An extended spectral gap is introduced into the spectrum of one pulse using an amplitude-only pulse shaper. The pulse is then spectrally sheared and subsequently interfered with the other uncharacterised pulse. By using the MICE technique, the spectral intensities and phases of the two fields are retrieved from a series of interferograms. The experimental results presented in this thesis show that SPICE is capable of reconstructing the spectral phase across an extended spectral gap enabling temporal characterization of multi-colour light pulses.

Author's Publications

Parts of this thesis have been published in the following articles

1. **F. Wiegandt**, P. N. Anderson, F. Yu, D. J. Treacher, D. T. Lloyd, P. J. Mosley, S. M. Hooker, and Ian A. Walmsley, "Quasi-phase-matched high-harmonic generation in gas-filled hollow-core photonic crystal fiber," Optica 6, 442-447 (2019)

2. **F. Wiegandt**, P. N. Anderson, Fei Yu, D. J. Treacher, D. T. Lloyd, P. J. Mosley, S. M. Hooker, Ia. A. Walmsley, "High-harmonic generation in gas-filled photonic crystal fibers" 2017 Conference on Lasers and Electro-Optics Europe European Quantum Electronics Conference (CLEO/Europe-EQEC)

3. Patrick N. Anderson, **F. Wiegandt**, Daniel J. Treacher, Matthias M. Mang, Ilaria Gianani, Andrea Schiavi, David T.Lloyd, Kevin, O'Keeffe, Simon M. Hooker, and Ian A. Walmsley, "Blind digital holographic microscopy" Practical Holography XXXI: Materials and Applications, Proceedings Vol. 10127, 101270H (2017)

Other Publications

1. **F. Wiegandt**, F. Trinter, K. Henrichs, D. Metz, M. Pitzer, M. Waitz, E. Jabbour al Maalouf, C. Janke, J. Rist, N. Wechselberger, T. Miteva, S. Kazandjian, M. Schöffler, N. Sisourat, T. Jahnke, and R. Dörner, "Direct observation of interatomic Coulombic decay and subsequent ion-atom scattering in helium nanodroplets," Phys. Rev. A 100, 022707 (2019)

2. D. J. Treacher, D. T. Lloyd, **F. Wiegandt**, K. O'Keeffe, and S. M. Hooker, "Optimised XUV holography using spatially shaped high-harmonic beams," Optics Express 27, 29016-29025 (2019)

3. S. Kazandjian, J. Rist, M. Weller, **F. Wiegandt**, D. Aslitürk, S. Grundmann, M. Kircher, G. Nalin, D. Pitters, I. Vela Pérez, M. Waitz, G. Schiwietz, B. Griffin, J. B. Williams, R. Dörner, M. Schöffler, T. Miteva, F. Trinter, T. Jahnke, and N. Sisourat, "Frustrated Coulomb explosion of small helium clusters" Phys. Rev. A 98, 050701(R) (2018)

To my Father

Contents

1 Introduction **1**

1.1 Thesis motivation 6

1.2 Thesis outline 7

2 Ultrashort optical pulses **9**

2.1 Light pulses 9

2.1.1 Spectral and temporal phase 12

2.2 Nonlinear optical effects 16

2.2.1 Second Harmonic Generation 17

2.2.2 Self phase modulation 20

2.3 Guided laser beams 22

2.3.1 Waveguides 22

2.3.2 Photonic Crystal Fibres 26

3 High-harmonic generation **29**

3.1 The single-atom response 30

3.1.1 Semi-classical treatment of HHG 30

3.1.2 Quantum description of HHG 35

3.2 Macroscopic effects and phase matching 40

3.2.1 Ionization model 41

3.2.2 Phase matching HHG in a waveguide 42

4 HHG in Photonic Crystal Fibres **60**

4.1 Concept . . . 60

4.1.1 Background . . . 60

4.1.2 Experimental Setup . . . 63

4.2 Non-phase-matched HHG in a PCF . . . 67

4.3 Quasi-phase-matched HHG in a PCF . . . 69

4.4 HHG efficiency . . . 72

4.5 Phase-matched HHG in a PCF . . . 76

5 IDC-QPM with orthogonal polarization **79**

5.1 Concept . . . 79

5.1.1 Background . . . 79

5.1.2 HHG build-up . . . 81

5.1.3 Method . . . 85

5.2 Results . . . 86

5.2.1 Enhancement . . . 89

5.3 Conclusion . . . 91

6 Metrology of ultrashort pulses **92**

6.1 Optical Correlation . . . 93

6.1.1 Intensity autocorrelation . . . 93

6.1.2 Interferometric autocorrelation . . . 95

6.2 FROG . . . 96

6.3 SPIDER . . . 99

6.4 Discussion . . . 105

6.4.1 Multi-Colour Pulses . . . 105

7 Characterization of multi-colour pulses **108**

7.1 Background . . . 108

7.1.1 MICE 109
7.2 Applications of MICE 111
7.2.1 Application to SEA-CAR-SPIDER 112
7.2.2 SPICE 115
7.3 Experimental Method 117
7.3.1 Test pulse preparation 119
7.3.2 Shear Calibration 120
7.3.3 SPICE interferogram 121
7.4 Results 122
7.5 Conclusion 127

8 Conclusion **129**

8.1 Summary 129
8.2 Outlook 131
8.2.1 HHG driven with high-average power 131
8.2.2 XUV-MICE 132
8.2.3 Blind digital holographic microscopy 135

Chapter 1

Introduction

The universe hides its sheer infinite mysteries on an unimaginable bounty of length scales, time scales, and energy scales. From the most weakly bound structures such as the helium dimer ($E_{\text{bind}} \approx 95 \times 10^{-9}\,\text{eV}$) to cosmic gamma-ray bursts ($\sim 1 \times 10^{63}\,\text{eV}$), from the size of atomic nuclei ($\sim 1 \times 10^{-15}\,\text{m}$) to the most distant quasars ($\sim 1.2 \times 10^{26}\,\text{m}$), and from the beginning of time (more than 13.8 billion years ago, $\sim 4.3 \times 10^{17}\,\text{s}$) to the time scale of the microscopic quantum world, the attosecond domain ($1\,\text{as} = 1 \times 10^{-18}\,\text{s}$), their understanding relies on the appropriate tools of observation.

It was beleived at the middle of the 20th century that knowing the structure of molecules would ultimately answer the question of their function. "If you want to understand function, study structure" (Francis Crick, 1962). However, in the following decades it was realized that the static picture alone cannot answer fundamental question about the processes in the microscopic world and that instead the time-dependent structure, the nuclear and electronic dynamics had to be studied. These dynamics evolve on a natural time scale of femtoseconds and attoseconds. A significant step towards developing a tool to answer these questions was the invention of the laser in 1960 [1]. This first laser source based on chromium doped corundum (Ruby) as a gain material was inherently a pulsed light source, capa-

ble of generating light pulses of millisecond duration. Soon after, pulsed laser sources enabled generation of very short bursts of light in the nanosecond and picosecond range and opened up the door to the investigation of the behaviour of matter under extreme conditions such as high energy density ($> 1\,\mathrm{Mbar}$), extreme light intensity and also enabled studying the microscopic, *ultrafast* dynamics in the femtosecond and attosecond domain. The development of modelocked, pulsed laser sources was brought forward by the invention of the dye laser. Solutions of some fluorescent dyes, such as rhodamine 6G, exhibit a broad gain bandwidth and enabled generation of laser pulses with a spectrum broader than that of continuous wave (CW) lasers supporting shorter pulse duration. The nanosecond and picosecond light pulses generated with this type of laser system enabled studying many non-linear interactions between light and matter. In the late 1980s, the role of fluorescent dyes as an active gain medium was taken over by the titanium-doped sapphire (corundum) crystal (Ti:Sapphire) [2] which enabled the generation of light pulses as short as a few femtoseconds at a central wavelength of 800 nm. The Ti:Sapphire laser paved the way to the investigation of nuclear motion in molecules. The short light pulses, commonly referred to as *ultrafast* laser pulses, allowed unblurred snapshots of the nuclear motion to be recorded. These still pictures, when stitched together in a sequence, form so called *molecular movies*. However, a fundamental limitation to the duration of such light pulses, and hence to the temporal resolution of such movies, is set by their fundamental wavelength. A pulse of light cannot be shorter than one optical cycle of the carrier wave, which in case of a Ti:Sapphire laser is 2.7 fs. Per se, this is often not sufficiently short to record the electronic dynamics in molecules.

Gain media capable of generating pulses shorter than in Ti:Sapphire have yet to be identified. However, the invention of the chirped pulse amplifier (CPA) in 1985 enabled short laser pulses to be amplified to higher pulse energies. The invention of this groundbreaking technique by Gérard Mourou and Donna Strickland has been

recognized with the Nobel prize in physics in 2018 [3]. The light pulses generated by such CPA give better access to regimes of high light intensities and nonlinear optical processes such as optical high-order harmonic generation. The discovery of optical harmonic generation dates back as far as 1961, only one year after the invention of the ruby laser by Theodore Maiman. Then, it was discovered that the millisecond-pulses of light from just these newly invented ruby lasers with a central wavelength of 649.3 nm, focussed into a quartz crystal, can generate radiation at a wavelength of 324.65 nm, the wavelength of the second harmonic. Ever since, second harmonic generation has played an important role in science and technological applications, ranging from second-harmonic generation microscopy to green laser pointers. However, the generation of higher order harmonics is challenging, since the generation efficiency drops exponentially with the harmonic order.

In the late 1980, scientists discovered that higher order harmonics can indeed be generated with acceptable efficiency from intense femtosecond laser pulses. High-order harmonic generation (HHG) then allowed for coherent generation of light at wavelengths much shorter than the driver wavelength, in the ultraviolet (UV) and extreme UV (XUV). The emitted spectra comprised of individual harmonic lines, and it was realized that the spectral bandwidth was broad enough to support pulses with much shorter duration than one optical cycle of the driving laser, as short as several hundred attoseconds. At present, attosecond light pulses play a key role as a tool for investigation of fundamental processes such as ionization dynamics in atoms and molecules, and to record these dynamics with high temporal resolution.

In times of shrinking computer chip-size, the static structure on a nanometre scale also becomes more and more important. It is predicted by Moore's law, with remarkable consistency, that the number of transistors fitted onto a dense, electronic integrated circuit (IC) doubles approximately every 24 months. Since the

early 1970s, the size of transistors on ICs has been decreasing steadily from tens of micrometres in the beginning to several nanometres to date. Manufacturing such electronic components by using lithographic processes requires exceptional high precision and optical resolution. The standard definition of diffraction limited lateral resolution in optics is called Rayleigh diffraction limit which essentially depends on the wavelength of light used for imaging. A higher resolution requires using light with shorter wavelength while sub-wavelength resolution is not achievable under normal circumstances. Lithographic and microscopic processes which require few-nanometre resolution therefore require light sources which emit light in the XUV wavelength range. The demand for bright, coherent XUV sources for applications such as coherent imaging has been increasing. To date, few techniques exist to generate light at such short wavelengths with a high spatial and temporal coherence. One commonly used source is a synchrotron light source in which short wavelength radiation is generated by high-energy electron beams travelling in a circular electron storage ring. Usually, these facilities are large (hundreds of meters in diameter) and their operation is very complex and costly. Additionally, the temporal coherence of these synchrotron sources is low and the shortest pulse length achievable is in the order of hundreds of picoseconds. In the recent years, free electron lasers (FEL) gained more and more significance, since they are capable of generating short wavelength light with unprecedented high brilliance and high spatial and temporal coherence. These light sources deliver pulses with durations in the order of tens of femtoseconds. However, FELs are even more costly and have to be built on an even larger scale than synchrotron facilities.

In contrast, the spatial and temporal coherence of HHG sources is, at the expense of brilliance, unbeaten by these types of light sources. Additionally, HHG sources can be build with much smaller footprints of only a few square metres and can be operated at a small fraction of the costs of FELs or synchrotron facilities.

A fundamental drawback to HHG is the low conversion efficiency of NIR driv-

ing laser power to power in the XUV wavelength range. Despite all efforts, the conversion efficiency remains below 10^{-5}. At the same time, the required light intensities to drive HHG are high, demanding the use of ultrashort pulses. High-harmonics can be generated by two types of visible or infra-red laser: (i) high-pulse-energy lasers, which typically operate at relatively low pulse repetition rates ($f_{\mathrm{rep}} = 1 - 10\,\mathrm{kHz}$) and provide pulse energies of typically a few mJ; and (ii) high repetition rate systems which operate at $f_{\mathrm{rep}} \sim 1\,\mathrm{MHz}$, but which provide pulse energies of typically a few µJ. Currently, HHG is commonly driven employing low repetition rate, low average power laser amplifiers. The high drive pulse energy enables generating a high XUV photon yield per laser shot. However, for many applications such as XUV lithography or coherent diffraction microscopy, the average flux is more relevant than the number of XUV photons generated per driving laser shot. Unfortunately, scaling Ti:Sapphire amplifier systems to a high average power by increasing the pulse repetition rate is problematic due to heating of the laser gain medium.

In the recent years, the range of ultrafast laser sources capable of delivering powerful, ultrafast laser pulses at a high repetition rate has grown significantly. The development of thin-disk lasers, Yb-doped fibre lasers and optical parametric chirped pulse amplifiers (OPCPA) promise a route towards ultrafast driving sources with average powers ranging up to tens or even to hundreds of Watts of average laser power. These sources usually operate at a significantly higher pulse repetition rate of a few MHz and provide pulse energies of a few µJ. The resulting low pulse peak power necessitates new schemes of HHG in order to enable efficient conversion of NIR driving power into XUV flux. One such scheme is generating high-order harmonics in capillary waveguides [4]. In order to keep the pulse peak intensity sufficiently high for HHG, the core size of these waveguides has to be small which results in higher guiding losses. However, modern photonic crystal fibre waveguides (PCF) provide much lower attenuation and mitigate this prob-

lem. In the past, HHG in PCF has been successfully demonstrated but with poor efficiency [5].

One other challenge in the field of ultrafast physics is measuring the temporal duration and shape of very short light pulses. Since femtosecond and attosceond pulses are the shortest known artificially generated events, the temporal shape of these pulses cannot be sampled using shorter instances. However, the pulses themselves can serve as a sampling reference. Over the years, many techniques have been developed to measure the temporal shape including autocorrelation measurements, interferometric techniques such as spectral phase interferometry for direct electric field reconstruction (SPIDER) and alternative techniques such as frequency resolved optical gating (FROG) which set out to measure the spectral intensity and spectral phase of a pulse, hence enabling full reconstruction of the temporal shape. Despite having been applied very reliably in the past decades, these techniques run up against limits when applied to ultrafast pulses which exhibit exotic spectral shapes such as extended spectral intensity nulls. In the past, spectral-gap immune characterization of electric fields (SPICE) has been attempted using mutual interferometric characterization of two electric fields (MICE), an iterative phase reconstruction technique [6]. However, experiments suffered from ambiguities which could not be resolved unobjectionably.

1.1 Thesis motivation

The motivation of the present thesis is to demonstrate new schemes aiming for efficient high-harmonic generation with few-microjoule driving laser pulses. This opens up a new prospect of constructing bright sources of coherent extreme ultraviolet radiation for microscopy and lithography capable of generating photon fluxes of 10^{12} photons per second at short wavelength of a few tens of nanometres. Furthermore, it is demonstrated that photonic crystal fibres can serve as waveguides

to aid the nonlinear interaction between microjoule-level driving pulses and the generating medium while offering the opportunity of performing multi-mode quasi-phase-matching to increase the efficiency of HHG process. Full-phase-matched HHG will be demonstrated for the first time in a photonic crystal fibre with multi-microjoule driving laser pulses. Furthermore, a multi-shot SPICE technique is demonstrated and applied to the characterization of the spectral phase of an ultrashort pulse exhibiting a spectrum with large spectral gap. This demonstrates that this technique would enable characterization of multi-colour, femtosecond laser pules which could have potential applications in high-harmonic generation and different fields of nonlinear optics.

1.2 Thesis outline

The thesis is organized as follows:

Chapter 2 introduces light pulses and the concept of waveguides. Firstly, a mathematical description is presented to describe short electromagnetic pulses and the conjunction of frequency domain and time domain is introduced. Secondly, it is set forth how waveguides, and in particular PCF, aid the investigation of nonlinear interaction between light and matter.

Chapter 3 presents high-order harmonic generation as a product of a extremely nonlinear interaction of light with a generating medium. A brief historical introduction of high-order harmonic generation is given and both, a semi-classical and a quantum description of the microscopic HHG process is introduced for a single dipole oscillator. The chapter proceeds in describing the macroscopic response of the material and introduces the concept of phase matching and multi-mode quasi-phase-matching. A mathematical model is developed to describe the build-up of the harmonic field in the presence of a waveguide and material dispersion, material inhomogeneity, and driver field amplitude modulation.

Chapter 4 presents the experimental investigation of high-harmonic generation in photonic crystal fibres. In the first half, the scientific background is presented, including relevant experiments carried out in the past, and the main experimental challenges are highlighted. Intermodal-delay-controlled quasi-phase-matching (IDC-QPM) is introduced as a concept capable of substantially increasing the efficiency of high-harmonic generation in photonic crystal fibres. Furthermore, the experimental setup used in the experiment work is described in detail. In the second half of the chapter, the experimental results are presented. First, non-phase-matched high-harmonic generation in a photonic crystal fibre and generation of record-high photon energies in a PCF is discussed. Second, quasi-phase-matched generation is demonstrated and the increased generation efficiency is discussed in the context of the previous achieved generation efficiencies. Third, fully-phase-matched high-harmonic generation is demonstrated in a photonic crystal fibre.

Chapter 5 presents a novel concept of increasing the performance of intermodal-delay-controlled quasi-phase-matching by using pairs of orthogonally polarized laser pulses (XIDC-QPM). The theoretical background and experimental results are presented and discussed in the context of the experimental results presented in the preceding chapter.

Chapter 6 introduces different metrology techniques for measuring the temporal shape of ultrashort laser pulses. The problem of measuring the spectral phase across a spectrum with extended intensity nulls is set forth.

Chapter 7 presents the experimental results of the SPICE experiment and the results are discussed in the context of previous SPICE experiments.

Chapter 8 summarizes the experimental findings presented in this thesis and gives a brief outlook.

Chapter 2

Ultrashort optical pulses

This chapter introduces the theoretical framework describing ultrashort femtosecond pulses. In the first section, the mathematical description of propagating electromagnetic pulses is defined. Starting from Maxwell's equation, monocromatic electromagnetic waves are described. Continuing with polychromatic wave packets, the relation of time domain and frequency domain is introduced and the relevance of temporal and spectral phase is discussed. In the subsequent section, guided laser pulses and optical waveguides are described.

2.1 Light pulses

Electric and magnetic fields can be described using Maxwell's equations:

$$\vec{\nabla} \cdot \vec{B} = 0 \tag{2.1}$$

$$\vec{\nabla} \cdot \vec{D} = \rho \tag{2.2}$$

$$\vec{\nabla} \times \vec{H} = \frac{\partial \vec{D}}{\partial t} + \vec{j} \tag{2.3}$$

$$\vec{\nabla} \times \vec{E} = -\frac{\partial \vec{B}}{\partial t} \tag{2.4}$$

where $\vec{B} = \mu_0(\vec{H}+\vec{M})$ is the magnetic flux density with the material magnetization $\vec{M}$, $\vec{D} = \varepsilon_0\vec{E}+\vec{P}$ is the electric displacement field with the material polarization $\vec{P}$, ρ is the charge density, and $\vec{H}$ is the magnetic field strength. The constants ε_0 and μ_0 are the vacuum permittivity and permeability. The speed of light in vacuum ($c = 299\,792\,458\,\mathrm{m\,s^{-1}}$) can be derived from these constants as $c = 1/\sqrt{\varepsilon_0\mu_0}$. Taking the curl of the curl equations (2.3) and (2.4) yields wave equations for electric and magnetic field:

$$\varepsilon_0\mu_0\frac{\partial^2\vec{E}}{\partial t^2} - \nabla^2\vec{E} = 0 \tag{2.5}$$

$$\varepsilon_0\mu_0\frac{\partial^2\vec{B}}{\partial t^2} - \nabla^2\vec{B} = 0 \tag{2.6}$$

The solution to these equations are plane waves:

$$\vec{E}(\vec{r},t) = \vec{E}_0\exp\left[i(\omega t - \vec{k}\vec{r}) + i\phi_0\right] \tag{2.7}$$

where the real-valued electric field $\mathcal{E}(t) = 2Re[E(t)]$, ω is the angular frequency and ϕ_0 is a phase constant. Inserting the solution (2.7) into the the wave equation (2.5) yields the dispersion relation:

$$k = \frac{\omega}{c} \tag{2.8}$$

where the wavenumber is defined as $k = |\vec{k}|$. Equation (2.7) describes monochromatic, plane waves with an infinite energy content and spatial extent. Equations (2.5) and (2.6) are linear second order differential equations. Therefore, any linear superposition of solutions to these equations are also solutions. In nature, these polychromatic superpositions of plane waves, so called *wave packets*, are a more

physical solution:

$$\vec{E}(\vec{r},t) = \int d\omega \int d^3k \vec{E}_0(\omega,\vec{k}) \exp\left[i(\omega t - \vec{k}\vec{r}) + i\phi_0\right] \tag{2.9}$$

These wavepackets represent pulses of light which propagate in space and time. As a pulse of light is a superposition of monochromatic waves, it has a finite frequency content. Since the time domain and the frequency domain are linked by a Fourier transform, the wave packet can be represented by the Fourier transform and inverse Fourier transform (FT, FT^{-1}):

$$E(\omega) = \int_{-\infty}^{\infty} dt E(t) \exp(-i\omega t) = FT\left[E(t)\right] \tag{2.10}$$

$$E(t) = \frac{1}{2\pi}\int_{-\infty}^{\infty} d\omega E(\omega) \exp(i\omega t) = FT^{-1}\left[E(\omega)\right] \tag{2.11}$$

From (2.10) it follows that the shape of the light pulse is represented in the frequency domain by the Fourier transform of the temporal electric field. The spectrum of the light pulse can be measured in a spectrometer and is the squared modulus of the Fourier transformed spatio-temporal electric field:

$$I(\vec{r},\omega) = |FT[E(\vec{r},t)\exp(-i\phi(\vec{r},t))]|^2 \tag{2.12}$$

where the spatio-temporal electric field has been written as a product of a spatio-temporal amplitude term and a phase term. Figure 2.1 illustrates the concept of wave packets. A monochromatic wave in the time domain is represented by a single frequency in the spectral domain. Coherently adding more spectral components or modes to the left and right sidebands, modulates the carrier wave. The spacing between the teeth of the resulting frequency comb determines the pulse repetition rate of the created pulse train. Decreasing the spacing of the spectral lines to the limit of a continuous spectrum, isolates a single optical pulse. The temporal

duration of the pulse is determined by the spectral bandwidth of the pulse. A short pulse in the time domain corresponds to a large frequency content in the frequency domain. Hence, the light pulse exhibits a broad spectrum. If all spectral components have the same phase, the resulting pulse of light has the shortest possible duration and is said to be *Fourier-limited* or *bandwidth-limited*. For a given pulse shape, the Fourier limited duration Δt at full-width half-maximum (FWHM) can be calculated using the time-bandwidth product:

$$\Delta\omega \cdot \Delta t = \alpha \tag{2.13}$$

where α is a constant corresponding to the pulse shape. For a Gaussian pulse $\alpha = 0.441$. The degree of which the spectral components of the pulse are in phase is determined by the *spectral phase*. To understand this, the role of the spectral phase will be discussed in the subsequent section.

2.1.1 Spectral and temporal phase

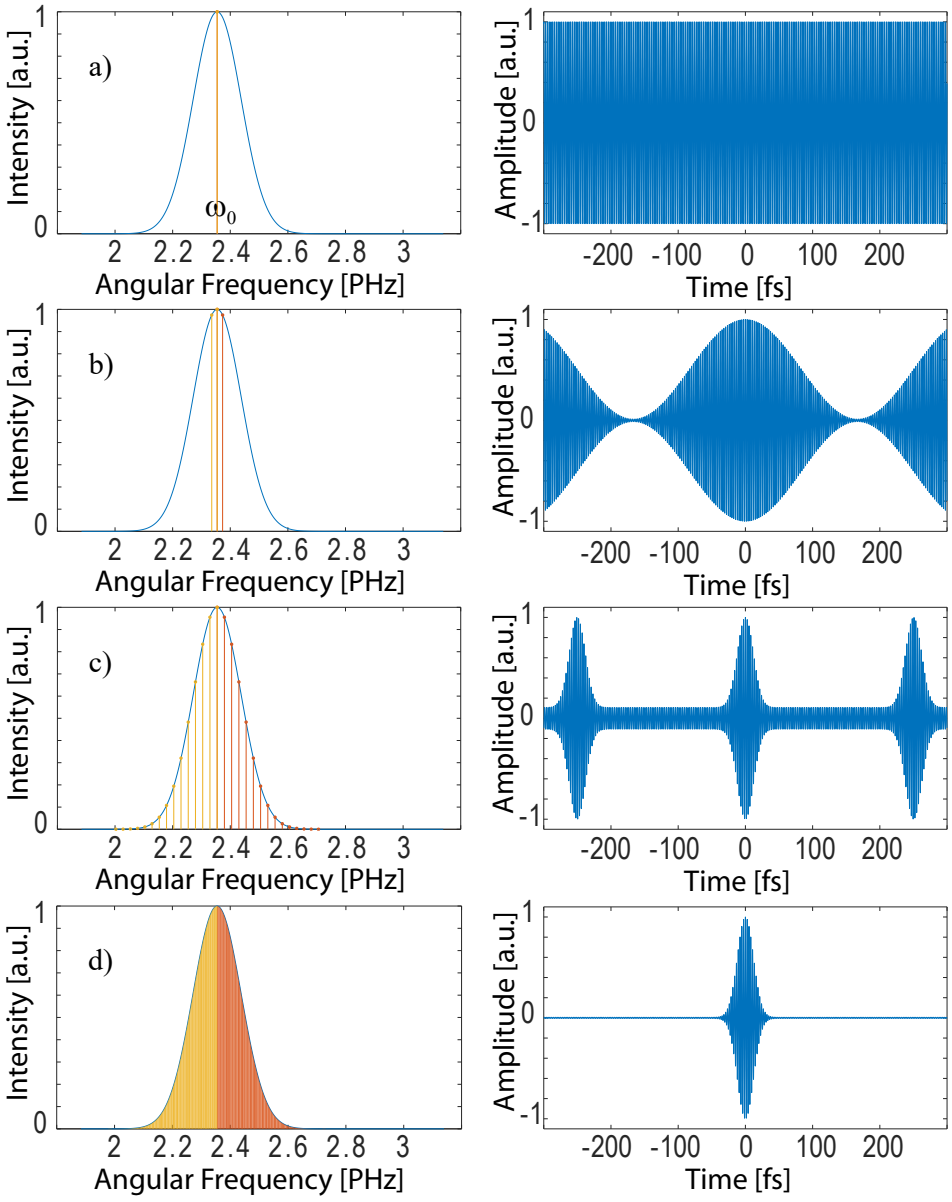
Expressing the spectral and temporal phase as a Taylor series permits breaking down the different contributions to the spectral phase:

$$\phi(\omega) = \sum_n \frac{1}{n!}\phi^{(n)}(\omega_0)(\omega - \omega_0)^n \tag{2.14}$$

$$\psi(t) = \sum_n \frac{1}{n!}\psi^{(n)}(t_0)(t - t_0)^n \tag{2.15}$$

where $\phi^{(n)}, \psi^{(n)}$ is the n^{th} derivative of the phase. The zero-th order phase $\phi^{(0)}, \psi^{(0)}$ represents the phase acquired at the frequency $\omega = \omega_0$, $t = t_0$ respectively. For light pulses this phase determines the offset between the phase of the carrier wave and the intensity envelope of the pulse. Therefore, this quantity is also known as the carrier-envelope-phase (CEP); this is illustrated in Fig. 2.2.

Figure 2.2a shows a Gaussian frequency comb. The teeth of the comb are



[h!]

Figure 2.1: **Gaussian frequency comb.**a) A monochromatic light wave with vacuum wavelength $\lambda = 800\,\mathrm{nm}$ is represented by a single spectral line located at $\omega_0 \approx 2.35\,\mathrm{PHz}$. b) Adding frequency components creates a temporal beating pattern. c) The spacing of the comb teeth determines the pulse repetition rate of the pulse train. d) Increasing the amount of spectral components isolates a single optical pulse in the limit of a continuous spectrum.

shown in orange and have an equal spacing which, extrapolated to the origin, exhibits a frequency offset, the carrier-envelope frequency-offset f_{CEO}. This results in a carrier-envelope phase-offset in the time domain which is illustrated in Fig. 2.2b. For pulses containing many optical cycles, the CEP is less significant. However, for experiments which involve few-cycle optical pulses, such as many HHG experiments, it is often desirable that the intensity maximum of the light pulse envelope coincides with a maximum of the oscillating electric field.

The first order derivative of the spectral phase $\partial\phi/\partial\omega$ is referred to as group delay. The group delay quantifies the relative delay for each spectral component of the pulse. In a uniform medium of length L, group delay and group velocity v_g are closely related:

$$\phi^{(1)}(\omega_0) = \left.\frac{\partial\phi}{\partial\omega}\right|_{\omega_0} = L \left.\frac{\partial k}{\partial\omega}\right|_{\omega_0} = \frac{L}{v_g} \tag{2.16}$$

In the time domain, a phase with a linear dependency in the Taylor expansion (2.14) corresponds to a shift of the pulse envelope in time with respect to an arbitrary time reference. The phenomenon that a linear phase in the spectral domain results in a shift in the time domain, and vice versa, is an example of the shift theorem for Fourier transforms. However, the absolute arrival time of the light pulse is often of no significant interest for many experiments.

The second order derivative of the spectral phase $\phi^{(2)}$ corresponds to the group delay dispersion (GDD) and is related to the group velocity dispersion (GVD):

$$GVD = \left.\frac{d}{d\omega}\left(\frac{\partial k}{\partial\omega}\right)\right|_{\omega_0} = \left.\frac{1}{L}\frac{\partial^2\phi}{\partial\omega^2}\right|_{\omega_0} = -\left.\frac{1}{v_g^2}\frac{dv_g}{d\omega}\right|_{\omega_0} \tag{2.17}$$

The group velocity dispersion has the effect that, in a medium, frequency components of the pulse propagate with different velocities. For a positive GVD, the redder wavelength components of the pulse propagate with a higher velocity than the bluer components resulting in a linear increase in frequency with time for a fixed point (a positive chirp), and a temporal broadening of the pulse. This can

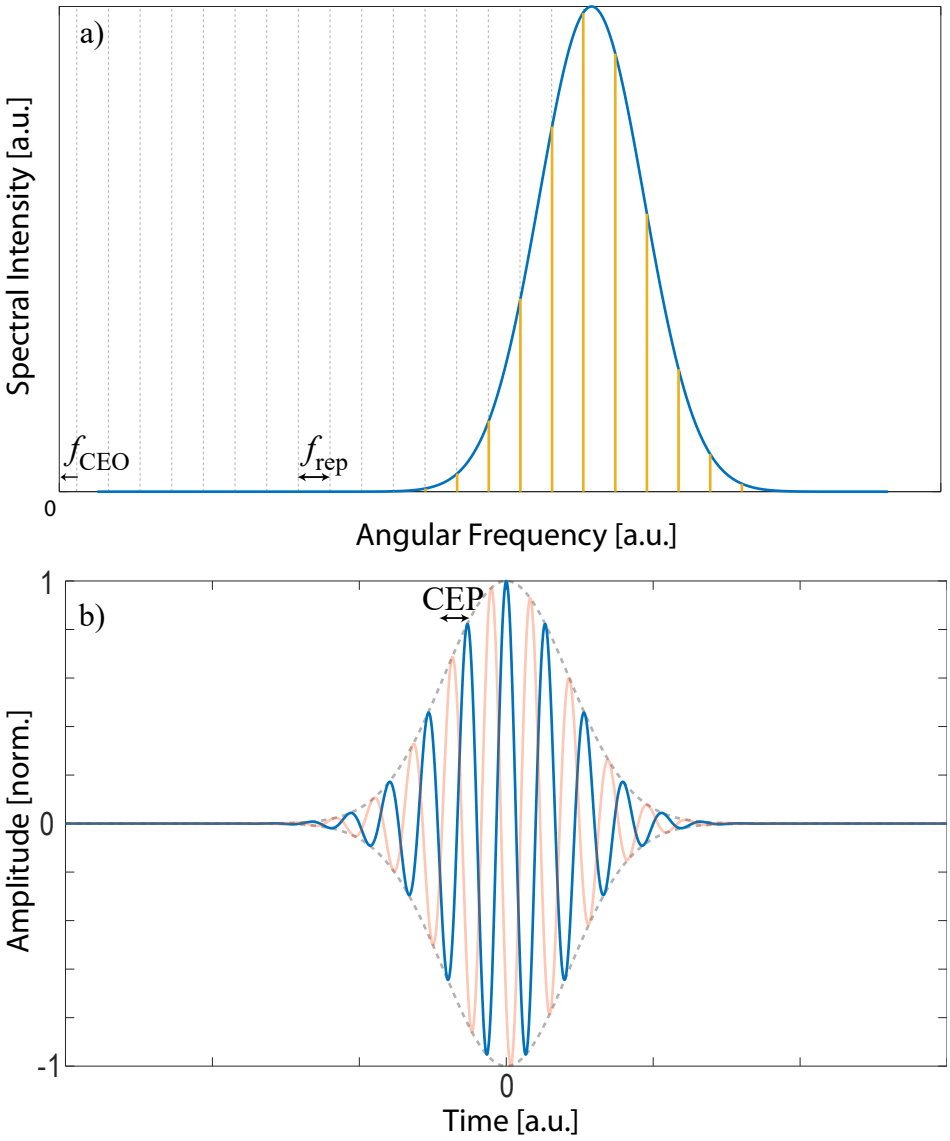


Figure 2.2: **Carrier Envelope Offset.** a) The frequency spacing between the teeth of the frequency comb, f_{rep}, determines the pulse repetition rate. The carrier-envelope offset frequency f_{CEO} is the frequency offset of the first comb tooth relative to $f = 0$. b) Carrier-envelope-phase (CEP) for a single light pulse of a pulse train.

be seen in the right column of Fig. 2.3b. When a light pulse propagates through a medium, it experiences GVD. For most materials this GVD is positive, and the material is said to have *normal dispersion*. Vice versa, if the pulse experiences a negative GVD, the material is said to have *anomalous dispersion*. Similarly, the higher order phase derivatives determine more complex characteristics of the light pulse in the temporal domain, the spectral domain respectively. A more detailed

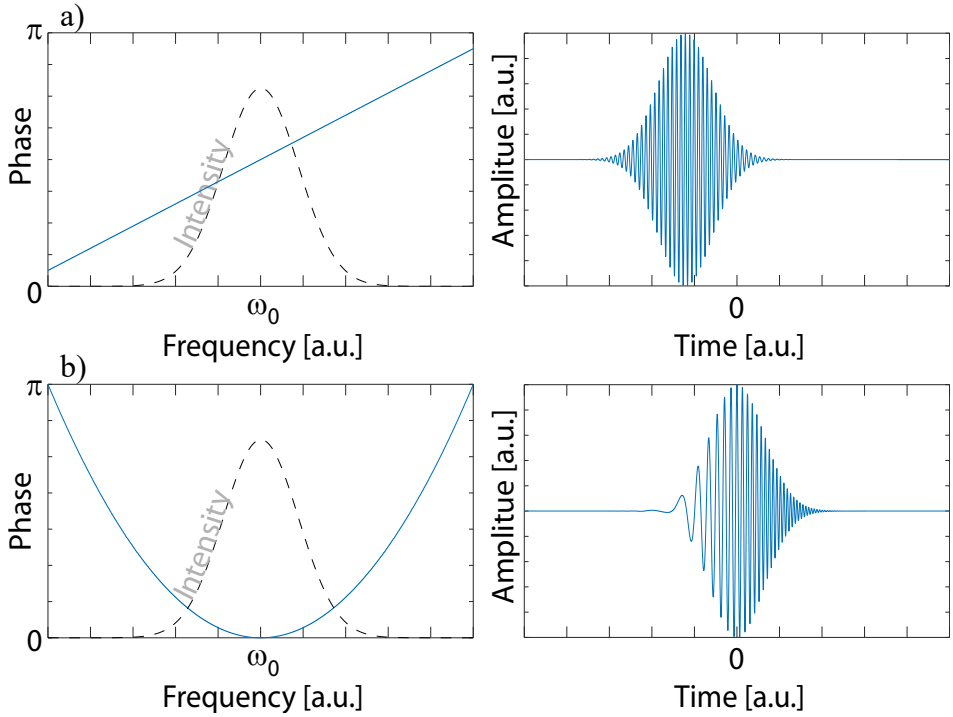


Figure 2.3: **Spectral phase.** a) Group delay determined by the first order derivative of the spectral phase. b) The group delay dispersion determined by the second order derivative of the spectral phase. Spectral intensity and spectral phase (left column) and corresponding time-dependent electric field (right column).

review of the aspects of spectral phase discussed above can be found in [7, 8].

In an experimental context, the GDD is the most relevant contribution since it is introduced by many optical elements such as glass prisms and lenses. If it is desired to keep the temporal duration of a pulse to a minimum, the Fourier limit permitting, the GDD introduced by optical elements in an experimental setup may be pre-compensated by generating light pulses which initially exhibit a negative GDD.

2.2 Nonlinear optical effects

The interaction between light and matter can be described in terms of a time-dependent polarization of the medium when it is illuminated with an oscillating electric field $E(t)$. In a perturbative treatment, the time-dependent polarization

$P(t)$ can be expressed as a Taylor series [9]:

$$\frac{P(t)}{\varepsilon_0} = \chi^{(1)}E(t) + \chi^{(2)}E^2(t) + \chi^{(3)}E^3(t)... \tag{2.18}$$

In this polynomial expansion the term proportional to the first order susceptibility $\chi^{(1)}$ describes a linear response to the incident field whereas the high-order terms account for nonlinear effects which gain significance at high field amplitudes. In general, the $\chi^{(n)}$ is a tensor representing the polarization-dependent nature of the interaction and the optical symmetries of the material. Many nonlinear optical effects such as second harmonic generation [10], self-focusing [11], four-wave mixing [12] or two-photon absorption [13] are associated with high-order terms in this expansion.

2.2.1 Second Harmonic Generation

Second-harmonic generation (SHG) was the first nonlinear optical effect that was observed [14]; it is governed by the second order susceptibility $\chi^{(2)}$. In SHG, two photons of the same angular frequency ω can combine, creating a single photon of frequency 2ω. This also holds for the case when the two incident photons have different frequencies, resulting in the emission of a photon with a frequency equal to the sum of the two input frequencies. This case is called sum-frequency generation (SFG).

In classical physics, light propagation in a medium is described as a coherent emission by electronic dipoles in the material which are set to oscillate by the incident light field. At high oscillation amplitudes, the oscillation of the electronic dipole oscillators becomes increasingly anharmonic. In this case, the dipoles can emit electromagnetic radiation at integer multiples of the ground oscillation frequency. In the dipole approximation of the electron-photon interaction, $\chi^{(2)}$ is a third-order tensor which is equal to zero in case of materials with a structure that

exhibits an inversion symmetry. In materials with no inversion symmetry such as β barium borate (BBO), second-harmonics can be generated. In the generation process, energy and momentum are conserved, demanding:

$$\omega_3 = \omega_1 + \omega_2 \tag{2.19}$$

$$k_3 = k_1 + k_2 \tag{2.20}$$

In an alternative picture, the second condition can be seen as *phase-matching*. The de-phasing quantity, the *phase-mismatch* $\Delta k = k_2 - 2k_1$, must be zero. This phase-mismatch accounts for propagation during SHG. At a given point along the propagation axis in the material, the electronic oscillators driven by the incident light field (*driver field*) radiate at frequency ω and 2ω. After propagation over a distance L, the driver generates second-harmonic radiation with the phase $k_1 L$, while the previously generated second-harmonic radiation reaches L with a phase $k_2 L$. If the distance L is such that ΔkL is zero, the two contributions can interfere constructively. This condition can only be met if the index of refraction for the driver and for the second-harmonic radiation are equal. For materials which exhibit normal dispersion, i.e. where the refractive index increases with the light frequency, this condition cannot be fulfilled. However, birefringent materials exhibit a refractive index which depends on the polarization and propagation direction of light through the material. In uniaxial crystals, the extraordinary index of refraction $\mathbf{n}_e(\omega)$ at the fundamental frequency may equal the ordinary index $\mathbf{n}_o(2\omega)$ at the second-harmonic frequency or vice versa. (To distinguish numeric indices n and index of refraction, the refractive index $\mathbf{n}$ will be written in bold characters.) The phase-matching angle θ_c between the propagation direction measured orthogonally to the surface of the crystal and the c-axis of the crystal can

Type	Positive ($\mathbf{n}_e > \mathbf{n}_o$)	Negative ($\mathbf{n}_e < \mathbf{n}_o$)
Type I	$ee \rightarrow o$	$oo \rightarrow e$
Type II	$oe \rightarrow o$	$oe \rightarrow e$

Table 2.1: Phase matching scheme for uniaxial crystals [6].

be calculated using [15]:

$$\left(\frac{1}{\mathbf{n}_e^{2\omega}(\theta)}\right)^2 = \frac{\sin^2(\theta)}{(\mathbf{n}_e^{2\omega})^2} + \frac{\cos^2(\theta)}{(\mathbf{n}_o^{2\omega})^2} = \left(\frac{1}{\mathbf{n}_o^{\omega}(\theta)}\right)^2 \tag{2.21}$$

In positive uniaxial crystals, such as quartz, the extraordinary index of refraction is higher than the ordinary index while the situation is reversed in negative uniaxial crystals such as calcite. There exist two phase matching categories, type I and type II, which are listed in Table 2.1. In case of type I phase-matching, the two mixing photons have the same polarization. In type II phase-matching, the two incident photons have orthogonal polarization. The intensity of the generated second harmonic can be calculated [15]:

$$I(2\omega) = \frac{2^7\pi^3\omega^2{\chi_{\text{eff}}}^2L^2}{\mathbf{n}^3c^3}I^2(\omega)\left(\frac{\sin(\Delta kL/2)}{\Delta kL/2}\right)^2 \tag{2.22}$$

where L is the length of the crystal and χ_{eff} is the effective susceptibility of the crystal for the given direction.

Ultrashort light pulses have a large spectral bandwidth. Therefore, frequency doubling of such pulses require a sufficiently large doubling bandwidth of the crystal. For negative uniaxial crystals, the doubling bandwidth (FWHM) is [15, 16]:

$$d\lambda_1 = \frac{\pm 1.39\lambda_1}{2\pi L}\left(\frac{\partial \mathbf{n}_o^{\omega}}{\partial \lambda_1} - \frac{1}{2}\frac{\partial \mathbf{n}_e^{2\omega}}{\partial \lambda_2}\right)^{-1} \tag{2.23}$$

where $\lambda_{1,2}$ are the wavelength of fundamental and frequency-doubled light. It can be seen by comparing equations (2.22) and (2.23) that the doubling bandwidth can be increased in expense of SHG yield by decreasing the thickness L of the

crystal.

2.2.2 Self phase modulation

Similar to effects governed by $\chi^{(2)}$, the third-order susceptibility $\chi^{(3)}$ governs higher-order nonlinear effects such as the Kerr-lens effect and self-phase-modulation (SPM).

The index of refraction can be written as a sum of a linear refractive index $\mathbf{n}_0$ and a nonlinear contribution $\mathbf{n}_2$:

$$\mathbf{n} = \mathbf{n}_0 + \mathbf{n}_2 I(t) \tag{2.24}$$

where $I(t)$ is the time-dependent intensity. For a plane electromagnetic wave $E(t,x) = E_0 \exp[i(\omega_0 t - kx)] = E_0 \exp[i\Phi(t,x)]$ propagating in a non-linear medium with the propagation vector $k = \mathbf{n}(t)\omega_0/c$, the instantaneous frequency can be written as the time derivative of the temporal phase:

$$\omega(t) = \frac{\partial}{\partial t}\Phi(t,x) = \omega_0 - \frac{\omega_0}{c}\frac{\partial \mathbf{n}(t)}{\partial t}x \tag{2.25}$$

It can be seen, that the instantaneous frequency depends on the temporal variation of the refractive index and hence on the instantaneous intensity of the input signal. The change in refractive index over time causes a phase modulation of the input field and the generation of new frequency components in the frequency sidebands of the input signal. The frequency variation can then be written as:

$$\delta\omega(t) = \omega(t) - \omega_0 = -\frac{\omega_0 \mathbf{n}_2}{c}x\frac{\partial I(t)}{\partial t} \tag{2.26}$$

If a light pulse propagates in a medium with a positive $\mathbf{n}_2$, low frequency components are generated in the leading edge of the input pulse while high frequency

components are generated in the trailing edge of the pulse. This leads to a red-shift of the leading edge and a blue-shift of the of the trailing edge, as illustrated in Fig. 2.4. Self-phase-modulation is commonly used as a technique for coherent

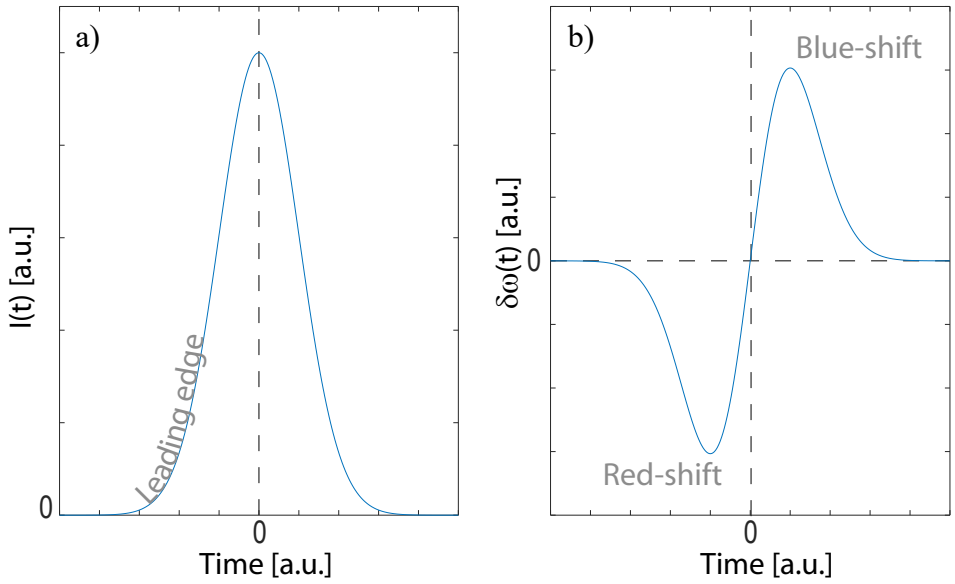


Figure 2.4: **Frequency shift due to SPM.** a) Instantaneous intensity of a Gaussian light pulse. b) Instantaneous frequency shift of the light pulse.

spectral broadening of ultrashort pulses [17].

SPM in a plasma

At high field intensities, optical-field-induced ionization can cause a rapid change in the free electron density in the material, and hence a change in the refractive index. The resulting SPM leads to spectral broadening. The ionization-induced SPM differs from SPM at lower pulse intensities where material ionization can be neglected. At high light intensities, the free electrons in the generated plasma exhibit a high polarizability while the ionization rate and the change in refractive index are a highly nonlinear function of the light intensity. As the average recombination time for the liberated electrons is much longer than the drive pulse duration, ionization can be regarded as an irreversible process which increases the free electron density over the duration of the light pulse. This causes an asym-

metric spectral broadening due to more wavelength components being generated at the blue end of the pulse spectrum. This results in an overall blue-shift (*plasma blue-shift*) of the pulse spectrum which is proportional to the ionization rate dZ/dt of the medium [18, 19]:

$$\delta\lambda = -\frac{e^2 N_i \lambda_0^3 L}{8\pi^2 m_e \varepsilon_0 c^3}\frac{dZ}{dt} \tag{2.27}$$

where e is the electron charge, N_i is the ion density, L is the length of the ionized medium, m_e is the electron mass, ε_0 is the vacuum permittivity, c is the speed of light in vacuum, and Z is the degree of ionization. Plasma blue-shift is frequently observed in experiments involving intense light pulses which are focussed into a gas such as in high-harmonic generation [18, 19, 20].

2.3 Guided laser beams

2.3.1 Waveguides

Waveguides are structures which are capable of guiding electromagnetic waves. The electromagnetic wave is confined in the core of such waveguides in which it propagates along the longidudinal axis. Waveguides can be (for instance) cylindrical or rectangular, metallic tubes which are commonly used for guiding microwaves. For light, dielectric waveguides such as step-index optical fibres or hollow-core waveguides (HCF) can serve as waveguides. HCF were studied theoretically by Carson et al. in the early sixties [21]. In 1964, Marcatili and Schmeltzer studied, in a pioneering work, the feasibility of using the dielectric hollow fibre waveguides (capillary waveguides) in optical telecommunications [22]. Later on, Miyagi and Karasawa studied the bending losses in HCF [23]. It was found that the optical attenuation constant α in HCFs scales with the core radius of the HCF

a and the bending radius R approximately with:

$$\alpha \propto \frac{1}{a^3} \tag{2.28}$$

$$\alpha \propto \frac{1}{R} \tag{2.29}$$

These early studies came to the conclusion that the trade-off between leaky loss and bending loss would ultimately prevent the application of such fibres for long-haul telecommunication.

Nevertheless, HCFs have since been successfully applied to guiding light in the near- and mid-infrared (NIR and MIR) for delivering high-power laser beams in industrial applications. In the late 1990s, the applicability of HCFs were extended to HHG, where they were found useful for overcoming beam divergence which would otherwise occur in a free focus generation geometry [4].

In waveguides, light propagates in eigenmodes (*modes*) which are solutions to Maxwell's equations within the boundary conditions set by the waveguide geometry. For capillary waveguides, Marcatilli and Schmeltzer categorized these solutions into three separate sets, namely transverse circular electric modes (TE_{0m}), transverse circular magnetic modes (TM_{0m}) for which the transverse magnetic or electric field component vanishes, and hybrid modes (EH_{nm}, $n \geq 1$) where all field components are non-zero. The radial and azimuthal electric field components $E_{\theta,nm}$, $E_{r,nm}$ of a capillary with the radius a are given by [22]:

$$E_{\theta,nm} = J_{n-1}\left[u_{nm}\frac{r}{a}\cos(n\theta+\phi)\right] \tag{2.30}$$

$$E_{r,nm} = J_{n-1}\left[u_{nm}\frac{r}{a}\sin(n\theta+\phi)\right] \tag{2.31}$$

where J_{n-1} is the $(n-1)^{\text{th}}$ order Bessel function of the first kind, u_{nm} is the m^{th} root of the equation $J_{n-1}(u_{nm}) = 0$ and ϕ is an arbitrary constant. Due to the vanishing transverse field components of TE and TM modes, linear polarized

light can only propagate in hybrid modes. For weakly guiding waveguides such as capillaries, the leaky mode solution can be approximated by a complete set of linearly polarized hybrid eigenmodes (LP modes), given that $\lambda_0/a \ll 1$ [24]. The normalized, transverse electric field of these modes inside the hollow core can be written as [25]:

$$E_{nm}(r) = J_{n-1}\left(u_{nm}\frac{r}{a}\right)\cos(n\theta) \tag{2.32}$$

When a free-space propagating, radially syemmetric laser beam is coupled into a HCF, radially symmetric azimuthal LP_{0m} modes are preferentially excited. The strength of excitation depends on the value of the spatial overlap integral between shape of the laser beam and shape of the eigenmode. For instance, the coupling efficiency η_m of a gaussian mode with a $1/e^2$ waist of w_0 into the EH_{1m} eigenmodes can be written as [26]:

$$\eta_m = \frac{\left[\int_0^a dr \exp(-r^2/w_0^2) J_0\left(u_{1m}\frac{r}{a}\right) r\right]^2}{\int_0^\infty dr \exp(-2r^2/w_0^2) r \int_0^a dr J_0^2\left(u_{1m}\frac{r}{a}\right) r} \tag{2.33}$$

For a linear polarized TEM_{00} Gaussian laser beam, optimal coupling efficiency into the fundamental LP_{01} eigenmode of a capillary with radius a, is $\eta_1 = 98.1\%$, is achieved for a coupling parameter χ of [26]:

$$\chi = \frac{w_0}{a} \approx 0.64 \tag{2.34}$$

For a given χ, the coupling efficiency into higher order modes decreases with the order of the mode (e.g. $\eta_2 = 0.5\%$) [26, 28]. For $\chi \neq 0.64$ or for an input mode which is transversally misaligned with respect to the modes of the fibre, more optical power can be coupled into higher order modes. This can be seen in Fig.

2.5. The radial intensity profile $I(r) = |E(r)|^2$ in the HCF can then be written as:

$$I(r) = \left| \sum_{n,m=1}^{\infty} \eta_m J_{n-1}\left(u_{nm}\frac{r}{a}\right) \right|^2 \tag{2.35}$$

Due to the lower refractive index in the hollow core, light in capillary fibres is not guided by total internal reflections at the core-cladding boundary. Instead, light is guided by partial Fresnel reflection which leads to an attenuation of the guided light since some light is transmitted into the capillary wall. The mode attenuation and propagation constants for the EH_{nm} modes at wavelength λ_0 in a straight, evacuated, hollow-core, dielectric waveguide with bore radius a can be

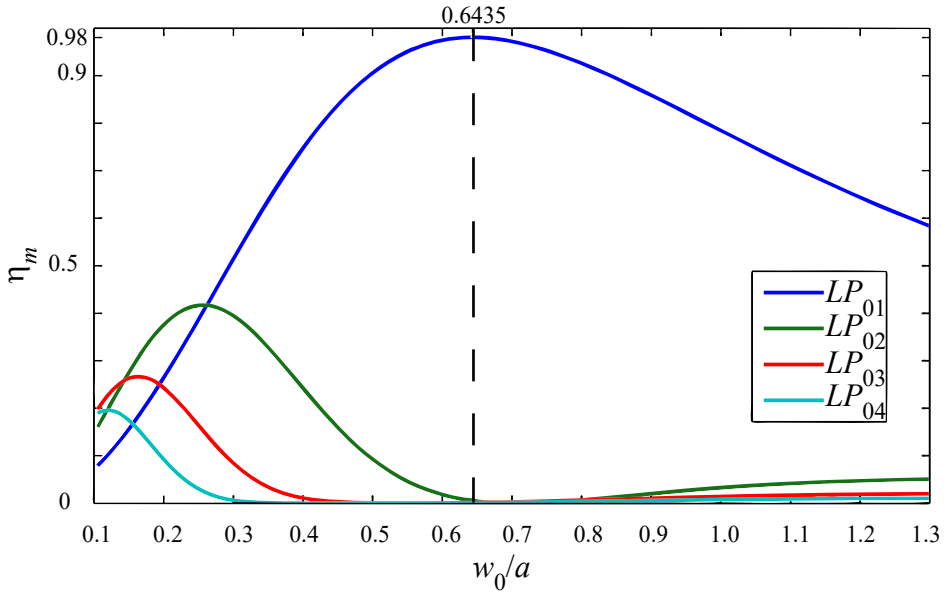


Figure 2.5: **Coupling efficiency η_m into different modes of order m for a gaussian beam** (adapted from [27]). The optimal coupling of a Gaussian mode with a beam radius w_0 into a capillary with radius a is achieved for $w_0/a \approx 0.64$. The coupling efficiency in this case is approximately 98%.

written as [22]:

$$\alpha_{nm} = \frac{\lambda_0^2}{a^3}\left(\frac{u_{nm}}{2\pi}\right)^2\left(\frac{\frac{1}{2}(\mathbf{n}^2+1)}{\sqrt{\mathbf{n}-1}}\right) \tag{2.36}$$

$$\beta_{nm} = \frac{2\pi}{\lambda_0}\left[1-\frac{\lambda_0^2}{2a^2}\left(\frac{u_{nm}}{2\pi}\right)^2\right] \tag{2.37}$$

where $\mathbf{n}$ is the refractive index of the cladding, α, β are the imaginary and real part of the propagation constants. For the radially symmetric EH_{1m} modes which correspond to the LP_{0m} modes, the intensity along the fibre can then be expressed as:

$$I(r,z) = \left|\sum_{m=1}^{\infty}\eta_m J_0\left(u_{1m}\frac{r}{a}\right)\exp\left[z(\alpha_{1m}+i\beta_{1m})\right]\right|^2 \tag{2.38}$$

2.3.2 Photonic Crystal Fibres

Hollow-core negative-curvature photonic crystal fibres (NC-PCF) represent a novel type of leaky mode optical waveguide with periodic cladding structure and an inverted curvature of the core-cladding boundary. In contrast to fibres which possess a photonic bandgap cladding, light propagates in eigenmodes of the NC-PCF which are not entirely confined in the hollow core. The guidance mechanism is most commonly explained with the model proposed by Marcatili and Schmerltzer [22], combined with antiresonant reflecting optical guidance [29], and the coupled-mode theory [30]. In a PCF, the propagation constant β is similar to that of a capillary [31]. However, the attenuation constant α might differ significantly from that of a capillary if a complex structure is introduced in the cladding. In fibres with a structured cladding of alternating high and low refractive index material $\mathbf{n}_2$, $\mathbf{n}_1$ each high-$\mathbf{n}$ layer with thickness d can be considered as a Fabry-Perot etalon. At wavelengths away from integer multiples q of the resonant wavelength given by λ_r (see equation (2.39)) these layers reduce the leakage of the core mode

into the cladding and therefore their attenuation.

$$\lambda_r = \frac{2\mathbf{n}_1 d}{q}\sqrt{\left(\frac{\mathbf{n}_2}{\mathbf{n}_1}\right)^2 - 1} \tag{2.39}$$

Recent theoretical studies [32] found that, in contrast to capillary waveguides where transmission loss scales with (λ_0^2/a^3) (see equation (2.36)), the loss of anti-resonant PCF scales with the number N of added anti-resonant layers $(\lambda_0/a)^{N+3}$. However, the modes of the inner core can couple to modes propagating within the structured cladding, resulting in loss outside specific transmission bands. The coupled-mode model takes account of this coupling and gives an explanation for the emergence of transmission bands and the core wall shape-dependent band characteristics in NC-PCF [33]. The core wall structure and shape have shown to significantly alter the fibre transmission loss by changing the spatial overlap between core and cladding modes [34]. Currently, the modelling of NC-PCF heavily relies on numerical simulations. The attenuation constants for different modes can be extracted from numerical solution of Maxwell's equations by means of finite element analysis, for instance using the softwave package *COMSOL* [35].

In the present experiment, NC-PCF with 22.5 µm and 53 µm core diameter were used. Figure 2.6 shows two microscope pictures of the NC-PCFs. The first type (*type I*) was used for demonstration of quasi-phase-matched (QPM) HHG with low pulse energies. The second type (*type II*, GLOphotonics PMC-C-650/2000-7C), shown in Fig. 2.6b, was used for demonstration of fully-phase-matched HHG in a NC-PCF.

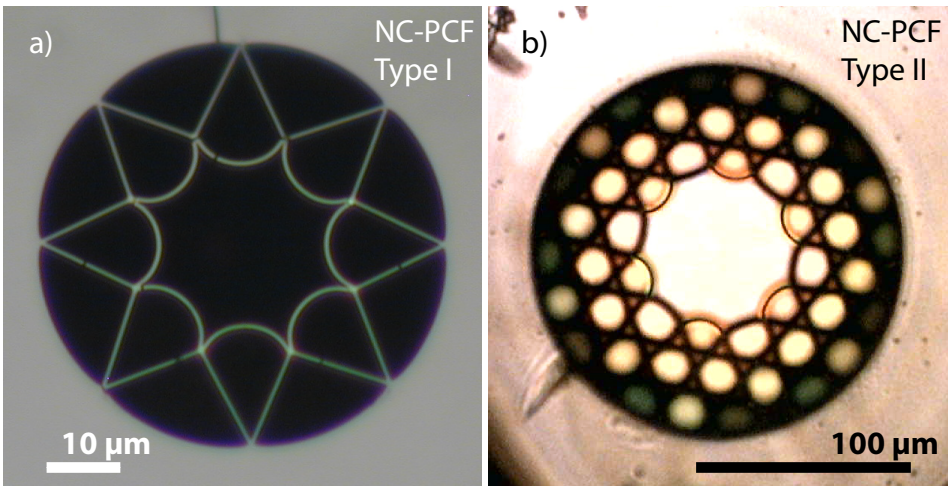


Figure 2.6: **Optical microscope images of the NC-PCFs used in experiment**). a) NC-PCF type I, $d = 22.5\,\mu\text{m}$. b) NC-PCF type II, $d = 53\,\mu\text{m}$.

Chapter 3

High-harmonic generation

Nonlinear optical phenomena such as sum-frequency generation or second harmonic generation play a key role in many scientific experiments and technological inventions. In this context, high-order harmonic generation (HHG) is often applied to generate coherent extreme ultraviolet (XUV) light for applications that include attoscience [36, 37] and high resolution coherent imaging [38].

At the end of the 1980s, scientists observerd a spectrum consisting of weak, odd order harmonics when focusing pulsed infrared and ultraviolet laser light into a noble gas target [39, 40, 41]. They discovered that after a rapid decrease for low order harmonics, the generation efficiency for higher harmonic orders stays approximately constant over an extended plateau region in the harmonic spectrum which can span tens of octaves before reaching a cutoff. In the early 1990s, it was realized that the bandwidth of the emitted harmonic spectrum was broad enough to support attosecond light pulses, opening a door to the investigation of fundamental physical processes on a sub-femtosecond time scale [42]. In 1993, the underlying physical mechanism which lead to the emission of the high-order harmonics were explained with a semiclassical model proposed by Paul Corkum [43]. One year later, Maciej Lewenstein developed a quantum mechanical description of the generation process [44].

The efficiency of HHG and its extension to shorter wavelength depends on a variety of parameters such as the ionization characteristics of the atom species involved in the generation process, the fundamental laser frequency, beam polarization, pulse duration, and peak intensity. As HHG is a coherent process, the macroscopic yield of XUV radiation relies not only on the single-atom response to the fundamental driving field, but additionally depends on collective effects. For instance, the optical properties and density of the generating medium determines the degree to which XUV radiation emitted by individual atoms can interfere constructively.

To date, HHG is most commonly generated by focusing intense near-infrared (NIR) to mid-infrared (MIR) femtosecond driving laser pulses into a noble gas. However, new generation media have been used recently, such as liquids [45]. Traditionally, two geometries have been used for HHG, namely a free-focus geometry and a guided geometry. Both situations take advantage of different macroscopic responses of the generating medium to the incident driving field.

3.1 The single-atom response

3.1.1 Semi-classical treatment of HHG

The interaction between light and matter can be described in terms of a time-dependent polarization of the medium when it is illuminated with an oscillating electric field E. In a perturbative treatment, the time-dependent polarization P can be expressed as a Taylor series (cf. equation (2.18)). Many nonlinear optical effects such as second harmonic generation [10], self-focusing [11], four-wave mixing [12] or two-photon absorption [13] are associated with high-order terms in this expansion. However, the presence of a plateau region in high-harmonic spectra is a clear signature that the interaction is *not* perturbative.

When an intense laser field of the form $E(t) = E_0 \cos(\omega_0 t)$ interacts with an atom, where ω_0 is the laser frequency and E_0 is the electric field amplitude, the effective potential $V(x)$ along the axis of laser polarization x is the sum of the atomic potential and the laser potential and can be written as:

$$V(x) = \frac{-e}{4\pi\epsilon_0 x} + E_0 \cos(\omega_0 t)x \tag{3.1}$$

At lower intensities, ionization may occur either through multi-photon absorption or tunneling ionization. The Keldysh-parameter γ is often used to describe which one of both ionization processes is predominant. This is given by [46]:

$$\gamma = \frac{\omega\sqrt{2m_e I_p}}{eE} = \sqrt{\frac{I_p}{2U_p}} \tag{3.2}$$

where

$$U_p = \frac{e^2 E_0^2}{2m_e\omega^2} \tag{3.3}$$

is the ponderomotive energy which corresponds to the average kinetic energy of a free and initially static electron oscillating in an electric field with frequency ω, E the field strength, and E_0 peak electric field amplitude. The known ionization energies I_p of the rare gases are listed in Table 3.1.

In the regime where $\gamma > 1$, bound electrons are mainly ionized through N-photon absorption, in case $N\hbar\omega = I_p$ [47]. The case where $N\hbar\omega > I_p$ is called above threshold ionization. It should be noted, that the N-photon ionization probability scales with the N^{th} power of the optical intensity.

At very high light intensities ($> 1 \times 10^{16}\,\mathrm{W/cm^2}$), the electric field amplitude of light incident on an atom becomes comparable to the atomic field strength (1 a.u. $\approx 5.14 \times 10^{11}\,\mathrm{V\,m^{-1}}$) and is capable of suppressing the atomic potential causing over-the-barrier ionization [48]. In the intermediate regime, where $\gamma < 1$ and at intensities around $1 \times 10^{14}\,\mathrm{W/cm^2}$, the electric field is high enough

Element	I_p
He	24.59 eV
Ne	21.56 eV
Ar	15.75 eV
Kr	13.99 eV
Xe	12.13 eV
Rn	10.75 eV

Table 3.1: Ionization potentials of some noble gases.

to promote tunnel-ionization where bound valence electrons can tunnel through the lowered atomic potential barrier and are released into the continuum. For quasistatic electric fields, the regime where $\gamma < 1$ is attributed to tunnel-ionization with the so called *tunneling limit* $\gamma \to 0$. However, it is discussed in literature, for instance in [49, 50], that in light fields the tunneling concept cannot be applied in the limits $\gamma \ll 1$ and $\gamma \gg 1$, and that γ alone cannot serve as a universal parameter identifying the nature of the ionization process. Instead, three independent quantities determine the regime of ionization: (1) the binding energy I_p, (2) the light frequency ω, and (3) the light intensity I. On the one hand, the dipole approximation is no longer valid when the intensity parameters $z \equiv U_p/\hbar\omega$ becomes too large, since the magnetic field component of the radiation has to be taken into account. Additionally, relativistic effects become significant when U_p becomes comparable to the electron rest mass energy and the intensity parameter $z_f \equiv 2U_p/m_e c^2 \geq 1$. On the other hand, the dipole approximation is also no longer valid when ω becomes large enough that the phase of a plane light wave cannot be regarded as approximately constant over the size of the atom. Taking into account these aspects, upper and lower bounds for γ can be found, beyond which a tunneling theory is no longer applicable [50].

In the NIR and at intensities around $1 \times 10^{14}\,\mathrm{W/cm^2}$, the electric field is high enough to promote tunnel-ionization. In the limit of $\hbar\omega \leq I_p \approx U_p$, tunnel-ionization forms the first step of the semi-classical model of HHG proposed by Corkum [43]. In this model, illustrated in Fig. 3.1, an electron is released into the

continuum with vanishing initial kinetic energy and follows a classical trajectory in the oscillating electric field. The motion of the freed electron can be described by the classical equation of motion:

$$m_e\ddot{x}(t) = -eE_0\cos(\omega_0 t) \tag{3.4}$$

By assuming that, at the instance of ionization t_i, the electron is located at the origin and has a vanishing initial kinetic energy, $x(t_i) = 0$ and $\dot{x}(t_i) = 0$, equation (3.4) can be solved and the resulting electron trajectories can be written as:

$$\dot{x}(t) = \frac{eE_0}{m_e\omega_0}\sin(\omega_0 t) - \frac{eE_0}{m_e\omega_0}\sin(\omega_0 t_i) \tag{3.5}$$

$$x(t) = \frac{eE_0}{m_e\omega_0^2}[\cos(\omega_0 t - \cos(\omega_0 t_i)] + \frac{eE_0}{m_e\omega_0}\sin(\omega_0 t_i)t - t_i \tag{3.6}$$

It can be seen in equation (3.6) that, driven by the laser field, the electrons follow an oscillating motion in the continuum. The classical trajectory the electron follows is determined by the instance of ionization t_i. Electron trajectories for various t_i are illustrated in Fig. 3.2.

On the continuum flight, the electron might be driven back into vicinity of the parent ion at position $x = 0$, whereupon it may recombine with the parent ion. When recombining, a total excess energy consisting of binding energy I_p and instantaneous kinetic energy of the electron is released by emission of a photon. The time spent by the electron in the continuum and the kinetic energy upon recombination are dependent on the trajectory, hence on t_i. However, the relation between the final kinetic energy and t_i is degenerate as can be seen in the red box of Fig. 3.2, since the electron can gain the same amount of energy on two different trajectories, namely a *long* and a *short* trajectory. The trajectory with the highest return kinetic energy of the electron is depicted in Fig. 3.2 as a orange, dashed

line corresponding to $t_i = 0.05T$, where $T = 2\pi/\omega_0$. On this trajectory the kinetic energy of the electron when recombining with the ion is $E_{kin} = 3.17U_p$ leading to the emission of a photon of energy:

$$\hbar\omega = I_p + 3.17U_p \tag{3.7}$$

This is in good agreement with the experimentally observed harmonic cut-off energy $E_c = I_p + 3.17Up$ [51].

The probability of ionization is much greater near the peaks of the electric field. Due to the spatial symmetry of the atomic potential, this results in a periodic burst of harmonics radiation every half optical cycle $T_0/2$ of the driving laser pulse. A quantum mechanical treatment of the electron transition from the bound state into the continuum, evolution of the wave packet in the continuum and final back transition to the bound state will be provided in the next section and shows that the emission is not only periodic but also phase-locked to the fundamental laser field which makes the generation process coherent [44]. Due to the coherence of the generation process, the sign of the harmonics field also changes with $T_0/2$ resulting in a real periodicity of the harmonics emission of T_0 with an anti-periodicity of $T_0/2$. By summing over n half optical cycles the total emitted field is:

$$E(t) = \sum_n A(-1)^n \exp\left[-i\omega_q(t + n\frac{\tau_0}{2}) + \phi\right] \tag{3.8}$$

$$= A\exp\left(-i\omega_q t + \phi\right)\sum_n \exp\left[-i\omega_q(n\frac{\tau_0}{2}) + n\pi\right] \tag{3.9}$$

The first term in equation (3.8) corresponds to an oscillating electric field with constant amplitude A and the harmonic frequency $\omega_q = q\omega_0$. The phase ϕ is proportional to the laser intensity and is known as the atomic dipole phase which accounts for the phase accumulated by the electron wave packet during evolution in

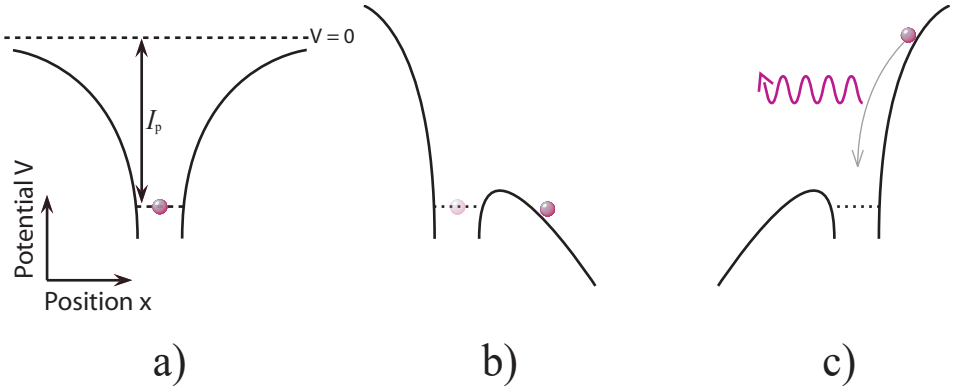


Figure 3.1: Three Step Model. a) The electron is bound in the atomic potential with the binding energy I_p. b) The driving field bends the atomic potential and the electron can tunnel through the lowered potential barrier. Once it enters the continuum, the initially static electron is accelerated and follows the electric field of the laser on a classical trajectory. c) When the electric field changes sign, the electron is driven back into vicinity of the parent ion and recombines. A photon of energy $\hbar\omega = I_p + E_kin$ is emitted.

the continuum [44]. The sum term which corresponds to the amplitude of the total electric field after n half cycles is divergent (i.e. the harmonics radiation interferes constructively) only for odd-integer multiples of ω_0 explaining the observation that HHG spectra are composed of odd-integer multiples q of the fundamental frequency.

$$\omega_q = q\omega_0 = (2\mathbb{N} + 1)\omega_0 \tag{3.10}$$

3.1.2 Quantum description of HHG

The semi-classical picture of HHG described above gives reasonably accurate predictions of features such as the cutoff energy of the harmonic spectrum. However, it fails at explaining important observations such as the driver wavelength dependent conversion efficiency [52], quantum path interference of the ionized electrons [53] and the presence of below-threshold harmonics [54] which can only be understood by applying a more accurate model of the microscopic dynamics. Such a

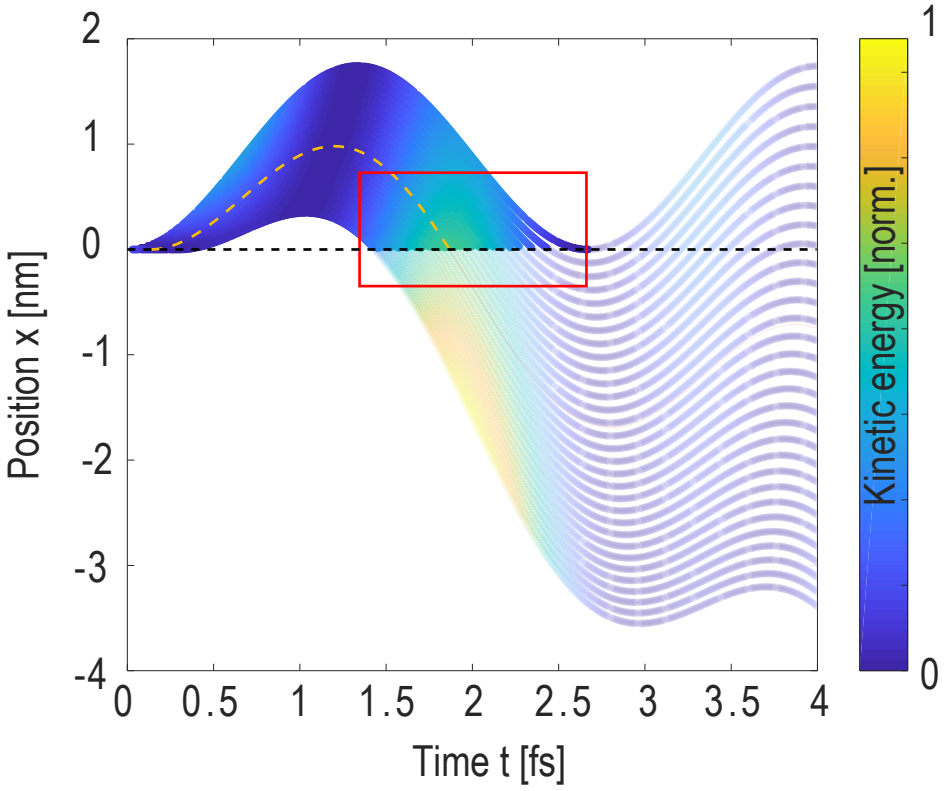


Figure 3.2: **Classical electron trajectories for different ionisation times** t_i. Tunnelling ionization is promoted by a laser field with peakintensity $I_0 = 1 \times 10^{14}\,\mathrm{W/cm^2}$ and $\lambda = 800\,\mathrm{nm}$. An electron is ionized with vanishing initial kinetic energy close to the peak electric field and is accelerated in the laser field. The colour scale represents the instantaneous kinetic energy of the electron during the flight in the continuum and has been normalized to the peak kinetic energy. After a half optical cycle of the driving laser field, the electron might re-collide with the parent ion at $x = 0$ (red box). It can be seen that the final kinetic energy of the electron depends on the trajectory, and hence on the ionization time t_i. The relation between final kinetic energy and the electron trajectory is degenerate, since the electron can gain the same amount of kinetic energy on two different trajectories, namely a *long* and a *short* trajectory. On the trajectory shown in dashed orange, the electron returns with a maximum kinetic energy of $\sim 3.17U_p$ corresponding to $t_i = 0.05T$, where $T = 2\pi/\omega_0$.

description has to be quantum mechanical.

A generic quantum mechanical description aims at solving the time-dependent Schroedinger equation (TDSE) which, in the length gauge and by using the electric dipole approximation, is given in a.u. by [55]:

$$i\frac{\partial\left|\Psi(t)\right\rangle}{\partial t}=\left[-\frac{\nabla^2}{2}+V_0(x)+E(t)x\right]\left|\Psi(t)\right\rangle \tag{3.11}$$

However, solving the full TDSE for the HHG process [55, 56] is computationally costly, hence a priori approximations are useful. In 1994, Maciej Lewenstein [44] proposed a model involving the so called strong field approximation which is based on three assumptions: (1) The strong light field couples only to the ground state and only the ground state and the states in the continuum (scattering states), have to be taken into account. (2) The amplitude of the ground state is known and ground state depletion can be neglected. (3) In the continuum, $V(x)$ can be neglected and the electron occupies a scattering state. In the tunnelling ionization and over-the-barrier ionization regimes where $\gamma < 1$, these three assumptions generally hold. Using this approximation, equation (3.11) can be solved exactly and the time-dependent dipole moment $x(t)=\langle\Psi(t)|\,x\,|\Psi(t)\rangle$ can be written as:

$$\begin{aligned}x(t)=&i\int_0^t dt_i\int d^3\vec{p}E(t_i)d_x(\vec{p}-\vec{A}(t_i))\\&\times d_x^*(\vec{p}-\vec{A}(t))\\&\times exp[-iS(\vec{p},t,t_i)]+c.c.\end{aligned} \tag{3.12}$$

The first term in the integral $E(t_i)d_x(\vec{p}-\vec{A}(t_i))=E_0\cos(t_i)d_x(\vec{p}-\vec{A}(t_i))$ is the transition probability amplitude for the electron to the continuum at the ionization time t_i, where $\vec{p}=\vec{v}+\vec{A}(t)$ is the canonical momentum and $\vec{A}$ is the vector potential of the driving field. The dipole matrix element depends on the shape of the binding potential. For the case of a single atom, the hydrogen s-orbital is a

good approximation.

$$d_x(\vec{p}) = i\frac{8\sqrt{2}(2I_p)^{5/4}}{\pi}\frac{\vec{p}}{(\vec{p}^2+2I_p)^3}. \tag{3.13}$$

The last term in the integral of (3.12), $e^{-iS(\vec{p},t_i,t)}$, represents the phase which is accumulated in the continuum by the freely propagating electron between ionization at t_i and t, where S is the quasi-classical action:

$$S(\vec{p},t_i,t) = \int_{t_i}^{t} dt' \left(\frac{[\vec{p}-\vec{A}(t')]^2}{2} + I_p\right). \tag{3.14}$$

The term $d_x^*(\vec{p}-\vec{A}(t))$ represents the probability amplitude for the back transition of the electron to a bound state of the atom at time t.

In (3.12), the contribution of the phase term governed by (3.14) is dominant as the quasi-classical action exhibits the fastest variation for $t-t_i$ in the order of one driving field cycle $T = 2\pi/\omega_0$. Therefore, from the infinitely many possible paths the electron can take in the continuum, constructive interference only occurs for those paths for which the phase is stationary, hence (3.14) is constant:

$$\nabla_{\vec{p}} S(\vec{p},t_i,t) = \vec{x}(t) - \vec{x}(t_i) = 0 \tag{3.15}$$

This implies that only electrons with momenta $\vec{p}$, liberated at time t_i contribute to the harmonic emission for which the electron returns to the origin after time t.

By using the saddle-point method, the inner integral in (3.12) can be evaluated yielding the electric dipole moment:

$$\begin{aligned}\vec{x}(t) =& i\int_0^\infty d\tau \left(\frac{\pi}{\epsilon + i\tau/2}\right)^{3/2} \\ & \times \vec{d}_x^*(\vec{p}_{st}(t,\tau) - \vec{A}(t)) \\ & \times \vec{d}_x(\vec{p}_{st}(t,\tau) - \vec{A}(t-\tau))E\cos(t-\tau)\end{aligned} \tag{3.16}$$

where $\tau = t - t_i$. The first factor in (3.16) is a regularization constant with respect to the spread of the electron wavepacket with time spend in the continuum and cuts off the contributions for long return times $\tau \gg T$, as the spread of the electron wavepacket becomes large, significantly reducing the recombination probability upon re-collision.

Further congruences between the semi-classical model and the model proposed by Lewenstein can be found by looking at the saddle point of the integral over τ of equation (3.16). Differentiation of the quasi-classical action (3.14) yields:

$$\frac{\left[\vec{p}_{st}(t,\tau) - \vec{A}(t-\tau)\right]^2}{2} + I_p = 0 \tag{3.17}$$

$$\frac{\left[\vec{p}_{st}(t,\tau) - \vec{A}(t)\right]^2}{2} + I_p = E_{kin}(t) + I_p = 2K + 1 \tag{3.18}$$

Equation (3.17) reflects the fact that for vanishing I_p, the electron liberated at $t - \tau$ are lifted into the continuum without kinetic energy. This is one of the basic assumptions of the semi-classical model of HHG. However, in the vicinity of an atom where $I_p \neq 0$, this implied that for non-imaginary τ, the electron must do this with a negative kinetic energy which is non-physical. An alternative interpretation is that the imaginary part of τ can be seen as the tunneling time of the electron. Recently experimental studies on helium and hydrogen, employing the 'attoclock' technique set out to measure the tunneling time and found it to be quasi-instantaneous [57, 58]. Equation (3.18) reflects the law of energy conservation and gives an expression for the final kinetic energy of the electron when returning to the parent ion causing emission of a photon at the $(2K+1)^{\text{th}}$ harmonic frequency. The physical interpretation is that the $(2K+1)^{\text{th}}$ harmonic is only emitted for t at which the electrons returning to their origin have appropriate kinetic energy.

Therefore, (3.15) together with, (3.17) and (3.18) confirm the basic assump-

tions of the semi-classical model. Maximization of the real part of (3.18) finally leads to a modified cutoff scaling law:

$$(2K+1)_{max} \simeq 3.17U_p + F(I_p/U_p)I_p \approx 3.17U_p + 1.3I_p \tag{3.19}$$

The cutoff law (3.19) takes account of quantum effects such as electron wavepacket diffusion. For strong driving pulses, where $I_p \ll U_p$, the small correction of $F(I_p/U_p) \approx 1.3$ is insignificant. However, at lower intensities where I_p is more comparable to U_p, this correction becomes more important.

3.2 Macroscopic effects and phase matching

So far, only the non-linear response of a single dipole oscillator has been described. However, the exact shape of the emitted harmonic spectrum and the macroscopic yield of XUV radiation are governed by the coherent superposition of the emission of all atoms or molecules in the generating volume. For instance, the optical properties and density of the generating medium determines the degree to which the harmonic radiation can be phase-matched to the fundamental driving field, enabling an efficient build-up of radiation and a high conversion efficiency.

A full description of the macroscopic response involves first calculating the single-atom response followed by propagating the driving field and the harmonic field through the interaction volume while taking the optical properties of the generating medium and the features of the generating geometry into account. Phase-matching the harmonic radiation with the driving field relies essentially on the optical properties of the generation medium, namely the refractive index. At the high laser intensities required for HHG, the generation medium is usually a plasma.

3.2.1 Ionization model

The theory of ionization of atoms in a strong oscillating electromagnetic field is well covered in literature. The most frequently applied theories in modelling HHG are the theories of the Russian physicists Leonid Keldysh [46, 59] and the Ammosov-Delone-Krainov ('ADK') theory [60]. Both theories give similar results. Tunnelling ionization is the dominant ionization effect in the regime where $\gamma < 1$. For the example of argon, the field strength for which $\gamma = 1$ is $3.2 \times 10^{10}\,\mathrm{V\,m^{-1}}$ corresponding to a pulse peak intensity of $I_{\mathrm{peak}} \approx 1 \times 10^{14}\,\mathrm{W/cm^2}$. Hence, for the experimental parameters in the present work, tunnelling ionization of the generating medium is the most relevant ionization mechanism.

According to Keldysh's theory, the tunnel ionization rate can be written in units of frequency in a.u. as:

$$\begin{aligned} w(F,\omega) =& \kappa^2 C_{kl}^2 \sqrt{\frac{3}{\pi}}(2l+1)\frac{(l+m)!}{2^m m!(l-m)!}\times \\ & 2^{2n^*-m} F^{m+1.5-2n^*} exp\left[-\frac{2}{3F}\left(1-\frac{1}{10}\gamma^2\right)\right] \end{aligned} \tag{3.20}$$

with

$$\begin{aligned} \kappa &= \sqrt{I_p/I_{pH}} \\ n^* &= Z/\kappa = Z\sqrt{\frac{I_{pH}}{I_p}} \\ F &= E/\kappa^3 E_a \end{aligned}$$

where Z is the charge of the ion, I_{pH} is the ionization energy for hydrogen, $E_a \approx 5.14 \times 10^9\,\mathrm{V\,m^{-1}}$ is the atomic unit of field strength, l and m are the atomic orbital and magnetic quantum numbers, n^* is the effective principal quantum number, and C_{kl} is dimensionless coefficient for the atomic wavefunction away from the

nucleus, modifying the ionization rate according to the geometry of the bound electronic wavefunction at large distances.

The instantaneous ionization rate $w(t)$ in an oscillating field $E(t)$ can be written as [60]:

$$w(t) = \omega_p |C_{n^*}|^2 \left(\frac{4\omega_p}{\omega_t}\right)^{2n^*-1} exp\left(-\frac{4\omega_p}{3\omega_t}\right) \tag{3.21}$$

with:

$$\begin{aligned} \omega_p &= \frac{I_p}{\hbar} \\ \omega_t &= \frac{eE(t)}{\sqrt{2mI_p}} \\ |C_{n^*}|^2 &= 2^{2n^*}[n^*\Gamma(n^*+1)\Gamma(n^*)]^{-1} \end{aligned}$$

The ionization rate determines the fraction of the atoms in the generating medium which is ionized. For the case of argon interacting with a 40 fs-laser pulse at wavelength $\lambda = 800\,\text{nm}$ and with peak intensity $I_{\text{peak}} = 2.75 \times 10^{14}\,\text{W/cm}^2$, the time-dependent ionization fraction $\eta(t)$ can be seen in Figure 3.3.

$$\eta(t) = 1 - exp\left[\int_{-\infty}^{t} dt' w(t')\right] \tag{3.22}$$

Keldysh's theory is generally applicable to atoms only. Nonetheless, a method has been proposed to extend Keldysh's model to molecules [61].

3.2.2 Phase matching HHG in a waveguide

As a macroscopic ensemble of atoms in the generating medium is irradiated by a laser field, spatial coherence of the driving beam is transferred to the harmonic beam. In order to maximize the total harmonic yield, the radiation emitted by the individual atoms must interfere constructively. Therefore, the mismatch between the propagation constants of the q^{th} harmonic at freqeuncy ω_q and the q^{th} multiple

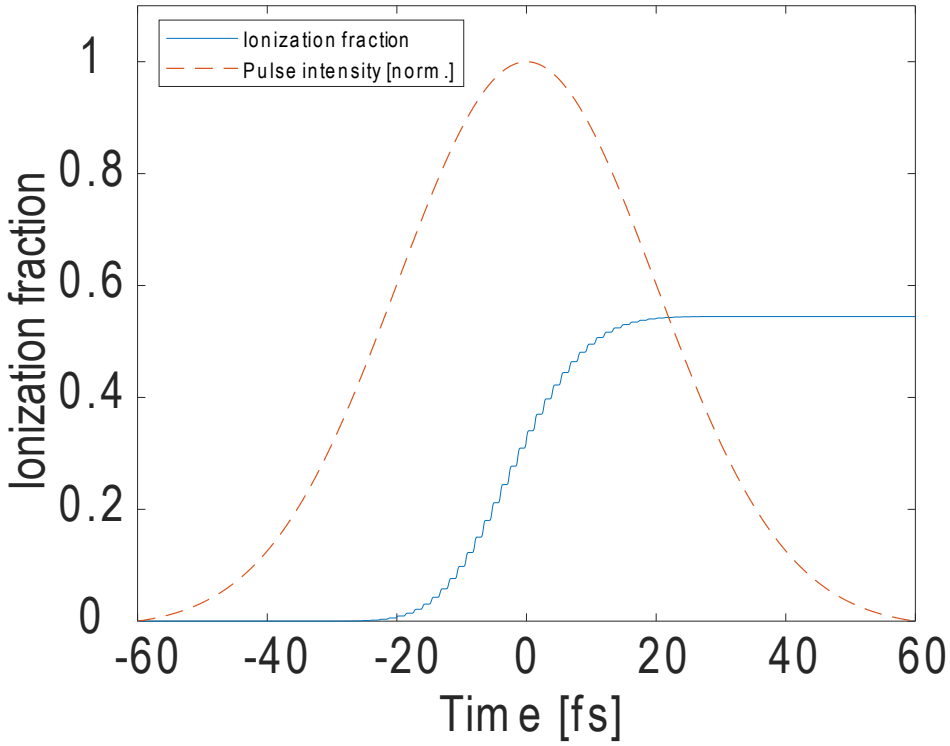


Figure 3.3: **Calculated ionization fraction**. The blue line shows the ionization fraction $\eta(t)$ calculated for argon according to Keldysh's theory for a pulse with $\lambda = 800\,\mathrm{nm}$, $I_{\mathrm{peak}} = 2.75 \times 10^{14}\,\mathrm{W/cm^2}$ and a pulse duration of 40 fs. The dashed line shows the normalized intensity of the laser pulse.

of the propagation constant of the driver at frequency ω_0 has to be zero. This condition is called phase-matching. In free space and vacuum, phase-matching is always given, since the phase velocity is the same for all wavelength. However for light propagating in a waveguide or through a material, this is in general not the case. There, the wavevector k, i.e. the velocity of light propagation, is determined by the frequency dependent refractive index $\mathbf{n}(\omega)$ of the material.

$$k = \frac{\sqrt{\epsilon(\omega)\mu(\omega)}}{\sqrt{\epsilon_0\mu_0}} k_0 = \mathbf{n}(\omega) k_0 \tag{3.23}$$

where $k_0 = 2\pi/\lambda_0 = \omega/c$ is the wavevector of light in the vacuum and $\epsilon(\omega)$, $\mu(\omega)$ are the complex, frequency-dependent permittivity and permeability of the material.

In a guided geometry, the propagation of light additionally depends on the shape of the waveguide. The refractive index is then replaced by $\mathbf{n}_{\text{eff}}$ and the propagation constant of a specific waveguide mode β determines the propagation velocity.

$$\beta = \mathbf{n}_{\text{eff}} k_0 \tag{3.24}$$

For HHG, phase-matching of the harmonic radiation and the driving field can be achieved by choosing the right generation geometry and the material properties in order to match $\mathbf{n}(\omega_0)$ and $\mathbf{n}(\omega_q)$.

Phase matching

Consider the simplified case of third harmonic generation illustrated in Fig. 3.4 where a driver field at the fundamental frequency ω_0 generates a harmonic signal at frequency $\omega_q = 3\omega_0$. If driver and harmonic field propagate through a dispersive medium, the harmonic signal generated at different spots along the propagation axis of the driver cannot interfere constructively. This is illustrated in Fig. 3.4a. However, if the refractive indices at the two frequencies match, $\mathbf{n}(\omega_0) = \mathbf{n}(3\omega_0)$,

harmonic signal generated at different locations along the z-axis can interfere constructively, resulting in efficient build-up of harmonic signal. In the optical domain, phase-matching is the consequence of conservation of momentum. Hence, for the conversion of N photons of momentum $\vec{p}_i = \hbar\vec{k}_i$ into M photons of momentum $\vec{p}_j$, where $\vec{k}_{i,j} = 1/\lambda_{i,j}$ are the wave vectors of the photons with wavelength $\lambda_{i,j}$, it follows that:

$$\sum_{i=1}^{N} \vec{k}_i = \sum_{j=1}^{M} \vec{k}_j \tag{3.25}$$

Optical harmonic generation can be viewed as the generation of one photon with the wave vector $\vec{k}_q$ from q photons of the fundamental driving field with wave vector $\vec{k}_0$. For phase-matching, momentum is conserved and

$$\vec{k}_q = q\vec{k}_0 \tag{3.26}$$

The phase mismatch Δk is a measure of the quality of phase-matching.

$$\Delta\vec{k} = \vec{k}_q - q\vec{k}_0 \tag{3.27}$$

The coherence length is defined as the length over which the accumulated phase difference is π:

$$L_c = \frac{\pi}{|\Delta\vec{k}|} \tag{3.28}$$

For the present work, phase-matching along the propagation axis of the driver beam inside a waveguide is most relevant. In this one-dimensional case, equations (3.26) and (3.27) reduce to the scalar form.

As the driving field propagates in a waveguide of length L, it partly ionizes the gas. The driving field and the harmonics generated in the plasma propagate along the z-axis of the waveguide. The refractive index of the plasma can be written as

[62]:

$$\mathbf{n} = 1 + P\left((1-\eta)\delta(\lambda) - \frac{\eta N_{\text{atm}} r_e \lambda^2}{2\pi} + (1-\eta)\mathbf{n}_2 I\right) \tag{3.29}$$

where P is the gas pressure and N_{atm} is the number density of atoms at atmospheric pressure. At driving field intensities in the order of $1 \times 10^{14}\,\text{W/cm}^2$ used for HHG in the experiment described in present thesis, the contribution from the non-linear refractive index of the gas $\mathbf{n}_2 I$ is small compared to the other terms in (3.29) and can be neglected: $\mathbf{n}_2 = 9.8 \times 10^{-24}\,\text{cm}^2/\text{W}$ for argon at 1 bar [63]. The wave vector of light propagating in the waveguide can then be written as [64]:

$$\begin{aligned} k &= \mathbf{n}\beta_{mn} \\ &= \mathbf{n}\left(k_0 - \frac{u_{mn}^2 \lambda}{4\pi a^2}\right) \\ &= (1+\delta)\left(k_0 - \frac{u_{mn}^2 \lambda}{4\pi a^2}\right) \\ &= k_0 + \delta k_0 + \frac{u_{mn}^2 \lambda}{4\pi a^2} + \delta \frac{u_{mn}^2 \lambda}{4\pi a^2} \\ &\approx k_0 + \delta k_0 + \frac{u_{mn}^2 \lambda}{4\pi a^2} \end{aligned}$$

where β_{mn} is the propagation constant for the mn^{th} mode as defined previously, a is the radius of the waveguide, u_{mn} is the m^{th} zero of the Bessel function J_{n-1} and $\delta = \Re(\mathbf{n}) - 1$. The contribution from the term $\delta \frac{u_{mn}^2 \lambda}{4\pi a^2}$ is small and can be neglected. The propagation constants of the fundamental driving field k_f can then be written as:

$$k_f \approx \frac{2\pi}{\lambda_0} + \frac{2\pi(1-\eta)P\delta_0}{\lambda_0} - P\eta N_{\text{atm}} r_e \lambda_0 - \frac{u_{mn}^2 \lambda_0}{4\pi a^2} \tag{3.30}$$

where the last term $\frac{u_{mn}^2 \lambda_0}{4\pi r^2}$ is the *waveguide dispersion* which affects only light guided in the waveguide.

Unlike the driving field, the high-harmonic radiation is not affected by waveg-

uide dispersion, since it is essentially not guided. The propagation constant for the q^{th} harmonic can then be approximated as:

$$k_q \approx \frac{2\pi}{\lambda_q} + \frac{2\pi(1-\eta)P\delta_q}{\lambda_q} - P\eta N_{\text{atm}} r_e \lambda_q \tag{3.31}$$

The on-axis wave vector mismatch between the driving field and the q^{th} harmonic can then be written as:

$$\begin{aligned} \Delta k &= k_q - q k_f & (3.32)\\ &\approx q\frac{u_{mn}^2 \lambda_0}{4\pi a^2} + \eta P N_{\text{atm}} r_e (q\lambda_0 - \lambda_q) - \frac{2\pi P}{\lambda_q}(\delta_0 - \delta_q) & (3.33) \end{aligned}$$

In equation (3.33), waveguide dispersion, the dispersion of the plasma and the neutral gas contribute to the phase-mismatch:

$$\Delta k = \Delta k_{\text{waveguide}} + \Delta k_{\text{plasma}} - \Delta k_{\text{gas}} \tag{3.34}$$

It can be seen that the contribution of the plasma dispersion and the dispersion of the neutral gas have opposite sign. In many experiments, phase-matching can be achieved, by tuning P in order to balance all contributions [62].

Quasi-phase-matching

Below a critical ionization level, Δk can be minimized by adjusting the gas density while carefully balancing the contributions of waveguide dispersion, plasma dispersion, and dispersion of the neutral gas to the phase mismatch (3.33). However, requirement of high driver peak intensities for HHG often necessitates employing waveguides with small core sizes. Due to the comparatively high waveguide dispersion in waveguides with small core diameter d, phase-matching would require multi-atmosphere gas pressures resulting in strong XUV reabsorption and high gas loads onto the generation setup [65]. An alternative approach is quasi-phase-

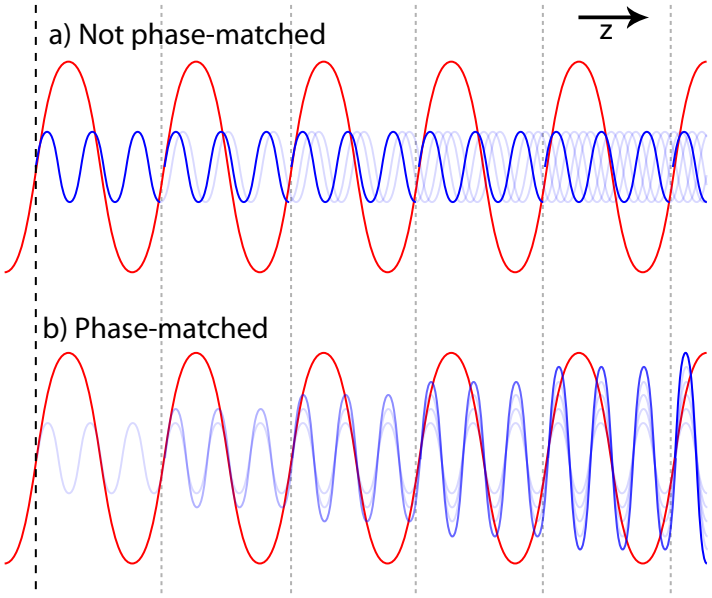


Figure 3.4: **Illustration of phase-matching**. For the purpose of illustration, a harmonic signal (blue) is generated every full cycle (horizontal lines) of a driver field (red) while the driver field phase is transferred to the harmonic signal. Both fields propagate along the z-axis while in case of a) both fields propagate with different phase velocities, leading to a phase shift between the harmonics generated at different spots along z. This causes destructive interference. In b) both fields propagate with the same phase velocity, causing phase-matching and constructive interference resulting in a build-up of harmonic radiation.

matching (QPM) in which destructive interference of harmonic radiation emitted at different locations is inhibited by suppressing HHG periodically along the propagation axis. This can be achieved, for instance, through longitudinal intensity modulation of the driving laser with a period:

$$L_{QPM} = \frac{2\pi j}{|\Delta k|} \tag{3.35}$$

where j is the odd integer order of QPM. This allows for more efficient intensity build-up even when $\Delta k \neq 0$ at comparatively low gas pressures. Several different schemes have been developed for on-axis amplitude modulation of the driving laser in a capillary waveguide including periodically modulating the waveguide diameter or employing mode beating [66, 67, 68]. In the experiment presented in this chapter, QPM is realized by a variation of the MM-QPM scheme demonstrated

in [69, 66]. Intensity modulation is achieved through beating of LP_{mn} waveguide modes [28] with different propagation constants β_{mn} and $\beta_{\mu\nu}$ (cf. equation (2.36)). This is illustrated in figure 3.5. The beating period is given by:

$$L_B = \frac{2\pi}{|\beta_{mn} - \beta_{\mu\nu}|} \approx \frac{2\pi^2 d^2}{|\lambda_0 u_{mn}^2 - u_{\mu\nu}^2|} \tag{3.36}$$

where u_{mn} is the n^{th} zero of the Bessel function of order $m-1$. Optimal MM-QPM is achieved if the gas density and pulse peak intensity are chosen such that $L_{QPM} = L_B$.

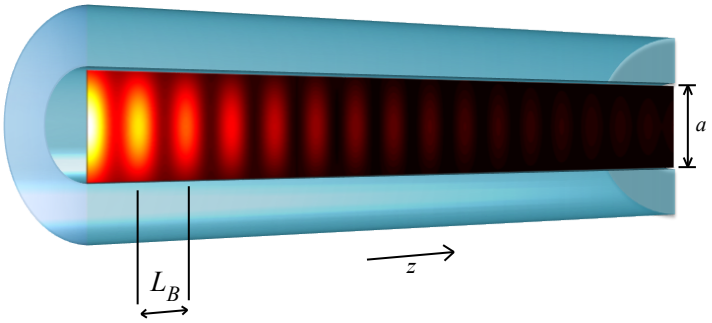


Figure 3.5: **Beating of two modes of a capillary waveguide**. As a laser beam propagates in two eigenmodes (LP_{01} and LP_{02}) of a capillary with core diameter a. The laser beam suffers from propagation attenuation while the intensity is modulated along the z-axis due to mode beating. The beat length L_B is the distance between two longitudinal beating (anti)nodes.

In practice, exciting only two specific waveguide modes is difficult and the beating of a large number of modes results in complex longitudinal beating patterns [69, 66]. This reduces the efficiency of MM-QPM. In order to set more controllable experimental framework conditions for the test of MM-QPM, an innovative concept to induce modebeating between pairs of waveguide modes has been developed: The intermodal delay dispersion is used to separate temporally the modes excited by a pair of femtosecond pulses; this allows selected, isolated modes to be temporally overlapped at the exit of the NC-PCF. The concept of this intermodal delay-controlled QPM (IDC-QPM) is illustrated in Fig. 4.5a together with the results of a numerical unidirectional pulse propagation simulation [70] in

Fig. 4.5b, limited to the five lowest order LP_{0n} modes of the NC-PCF used in the experiment. A pair of identical NIR laser pulses, termed "control" and "drive", is generated in a Mach-Zehnder interferometer fitted with a variable delay stage in one interferometer arm. First, the control pulse is launched into a section of the NC-PCF exciting a set of LP modes. As the pulse propagates a distance z into the NC-PCF, modal dispersion causes the different modes to walk-off temporally. At the exit of the NC-PCF ($z = L$), the group delay between the fundamental mode LP_{01} and a given higher order mode LP_{mn} can be expressed as:

$$\tau_{mn} = \frac{2\pi L c}{\lambda_0 \left(\frac{\partial^2 \beta_{mn}}{\partial \omega^2} - \frac{\partial^2 \beta_{01}}{\partial \omega^2} \right)} \tag{3.37}$$

where c is the speed of light and ω is the angular frequency. The propagation constants α_{mn} of the core modes in the NC-PCF used in this experiment are calculated numerically by using commercial finite-element method software (COMSOL) following the approach reported in [71]. However, the propagation constants β_{mn} are similar to those of a capillary with similar diameter and can be approximated using equation (2.36) [31]. When the drive pulse is coupled into the fibre with a delay $\tau = \tau_{mn}$, the fundamental mode of the drive pulse overlaps with a higher order mode of the control pulse close to the exit of the fibre. In the overlap region, the carrier waves of both pulses interfere and cause amplitude modulation (AM) of the electric field (Inset, figure 4.5b).

Refractive index in the NIR

The refractive index **n** of a material is a dimensionless number that describes by which factor the phase velocity of light v_{ph} inside the material differs form the speed of light in vacuum c_0. The refractive index depends on the relative permittivity ε

and the relative permeability μ of the material which can be frequency dependent.

$$\mathbf{n} = \frac{c_0}{v_{ph}} = \sqrt{\varepsilon\mu}$$

A frequency-dependent refractive index gives rise to *chromatic dispersion*. In contrast to the XUV regime, the refractive index in the visible and NIR regime typically increases with the optical frequency. This behaviour is called *normal dispersion*.

The real part or the refractive indices of various gases in the visible spectrum and in the NIR have been measured in the past and semi-empirical models were applied in the literature to fit the experimental data. In the NIR and for atomic rare gases, the imaginary part of the refractive index, i.e. the absorption coefficient, are taken to be zero and the refractive index model applied in [72] can be used.

$$\mathbf{n}^2 = 1 + A\left(1 + \frac{B}{\lambda^2} + \frac{C}{\lambda^4} + \frac{D}{\lambda^6} + \frac{E}{\lambda^8} + \frac{F}{\lambda^{10}}\right)$$

where λ is the wavelength of light in Angstrom. The Coefficients $A - F$ are listed in table 3.2. The refractive index of a gas varies with density. To scale the refractive index with pressure it is assumed that $\delta = \Re(\mathbf{n}) - 1$ and $\alpha = \Im(\mathbf{n})$ are proportional to the number density of gas atoms present and that the gas behaves like an ideal gas. For the noble gases at room temperature and pressures comparable to atmospheric pressure, this assumption is a good approximation.

	A	B	C	D	E	F
He	6.927×10^{-5}	2.24×10^{5}	5.94×10^{10}	1.72×10^{16}	0	0
Ne	1.335×10^{-4}	2.24×10^{5}	8.09×10^{10}	3.56×10^{16}	0	0
Ar	5.547×10^{-4}	5.15×10^{5}	4.19×10^{11}	4.09×10^{17}	4.32×10^{23}	0
Kr	8.377×10^{-4}	6.70×10^{5}	8.84×10^{11}	1.49×10^{18}	2.27×10^{24}	5.1×10^{30}
Xe	1.366×10^{-3}	9.02×10^{5}	1.81×10^{12}	4.89×10^{18}	1.45×10^{25}	4.34×10^{31}

Table 3.2: Coefficients to calculate the refractive index of rare gases [72]

Refractive index in the XUV

In contrast to the situation for the NIR region, the refractive indices of rare gases in the XUV and x-ray region are less well known. The refractive index in this wavelength region is linked to the ability of the atoms to interact with short wavelength radiation. This can be characterized by the atomic scattering factors f_1 and f_2. In explicit, f_2 describes how strongly the material absorbs the radiation while f_1 describes the non-absorptive characteristics which lead to dispersion.

The atomic scattering factors for various elements are given in the literature, for instance in [73, 74, 75]. In [73] Henke *et al.* define the scattering factor $f = f_1 + if_2$ for an atom exposed to an electric field E_0 as the factor by which the field amplitude of radiation scattered by a single free electron must be multiplied to yield the total amplitude coherently scattered by a particular atom.

$$E = -E_0 \frac{r_e}{r} P(\Phi) f \tag{3.38}$$

where E_0 is the amplitude of the incident field, r is the distance from the atom to the observation point, $r_e = \frac{1}{4\pi\epsilon_0}\frac{e^2}{m_e c^2}$ is the classical electron radius, and $P(\Phi)$ is a polarization factor. For incident electromagnetic fields, polarized perpendicular to the scattering plane, $P(\Phi) = 1$ whereas $P(\Phi) = \cos(\Phi)$ for the case of a polarization vector in the plane of scattering. For wavelength long compared to the size of an atom, atoms scatter electromagnetic radiations as dipoles. The complex index of refraction $\mathbf{n}$ of an ensemble of atom can be derived from the scattering factors by [73]:

$$\mathbf{n} = 1 - \frac{r_e}{2\pi}\lambda^2 \sum_j n_j f_j \tag{3.39}$$

where n_j and f_i are the number of atoms of type j per unit volume and their forward scattering factor respectively. The refractive indices of various molecules

and chemical elements can be looked up conveniently through web resource [76].

Density of the generating medium in a gas-filled capillary

The complex refractive index depends on the number density of atoms. In a gas-filled waveguide, the number density of atoms inside the waveguide depends on the temperature and pressure of the gas. In the experiments presented in this thesis, the waveguides were filled in two different ways. For the experimental investigation of quasi-phase-matching, the waveguide is filled with gas at room temperature from one end while the other end is held at a high vacuum 3.6a. The different gas pressures at the entrance and exit of the waveguide, P_0 and P_L, then lead to a longitudinal pressure profile along the spatial coordinate z, illustrated in figure 3.7, which can be approximated as [77, 78]:

$$P(z) \approx \sqrt{P_0^2 + \frac{z}{L}(P_L^2 - P_0^2)} \tag{3.40}$$

For the experiments exploring fully phase-matched HHG, a homogeneous gas density is created by filling the waveguide with gas from two inlet points creating a region of constant pressure in between (Fig. 3.6b).

HHG build-up

The longitudinal on-axis build-up of the q^{th} harmonic in a waveguide is the coherent sum over the fields generated at each point along the z-axis of the waveguide. Assuming plane waves, the harmonic signal at the exit of the waveguide ($z = L$) can be written as [64]:

$$I_q(L) \propto \left| \int_0^L dz S_q P \exp\left[-i \left(\int_0^z dz' q k_f(z') + \int_z^L dz' k_q(z') \right) \right] \exp\left[\alpha\,(L - z)\right] \right|^2 \tag{3.41}$$

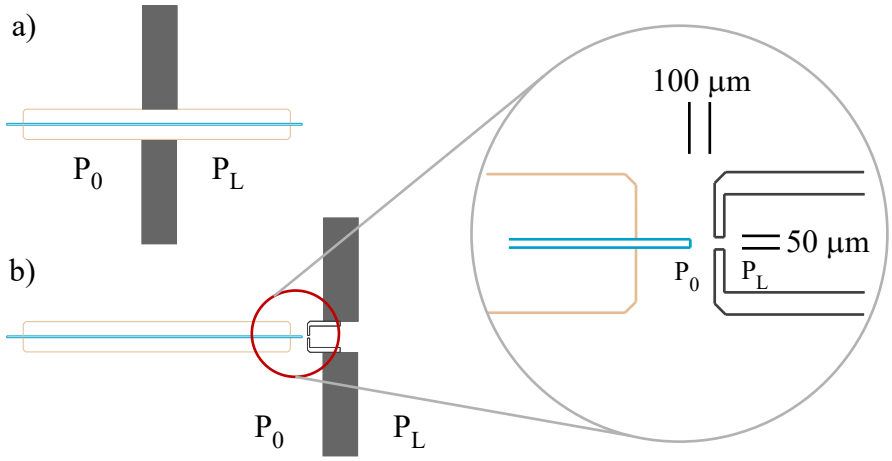


Figure 3.6: **Fibremount.** a) Sections of PCF glued into a zirconium dioxide ceramic ferrule are mounted in between two vacuum chambers. The first chamber (left side) is filled with gas at a high pressure (e.g. Argon at a pressure of $P_0 = 800\,\text{mbar}$) while the second chamber is held at a high vacuum ($P_L = 1 \times 10^{-2}\,\text{mbar}$). In this geometry, the gas pressure inside the fibre varies between P_0 and P_L. b) A section of PCF is mounted in front of a pinhole with a diameter of 50 µm which separates two vacuum cambers. The first chamber is filled with gas at a pressure of P_0 while a good vacuum is maintained in the second chamber. Due to the large flow of gas through the pinhole, P_0 is restricted to lower values than in (a).

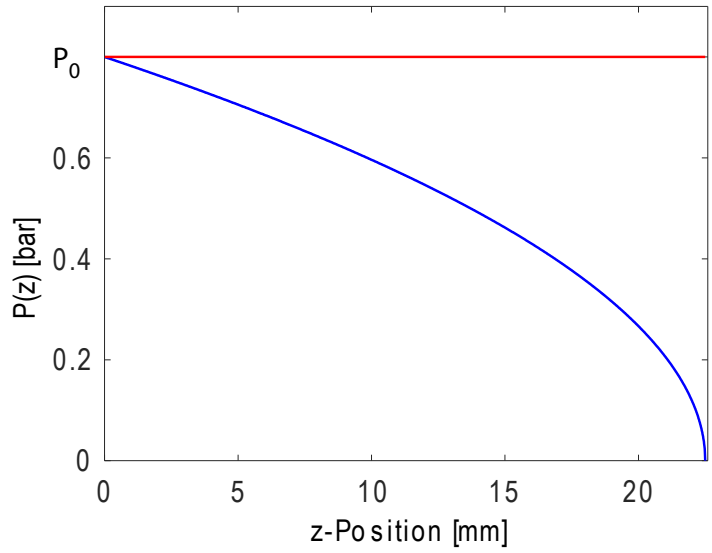


Figure 3.7: **Longitudinal pressure profile**. A cylindrical hollow-core waveguide with $L = 22\,\text{mm}$ is filled with gas at a pressure $P_0 = 0.8\,\text{bar}$ from both ends (red graph) and from one end at $z = 0\,\text{mm}$ while the other end at $z = L$ is held at a high vacuum (blue graph).

where $S_q(z)$ is the nonlinear source term, $P(z)$ is the gas pressure, $k_f(z)$ and $k_q(z)$ are the propagation constants of fundamental and harmonic field, and $\alpha(z)$ is the attenuation constant for the q^{th} harmonic order in the gas. In case of a uniform gas-fill and a constant longitudinal driver amplitude, S_q, P, k_f, k_q and α are constants and (3.41) simplifies to the form:

$$\begin{aligned} I_q(L) &\propto \left| \int_0^L S_q P \exp[-iqk_f z - i(k_q L - k_q z)] \exp[\alpha(L-z)] dz \right|^2 && (3.42) \\ &= \left| S_q P \exp(-ik_q L) \exp(\alpha L) \int_0^L \exp(i\Delta k z) \exp(-\alpha z) dz \right|^2 && (3.43) \\ &= \left| S_q P \exp(\alpha L) \int_0^L \exp(i\Delta k z) \exp(-\alpha z) dz \right|^2 && (3.44) \end{aligned}$$

where all constant phase factors have been dropped. The build-up of the harmonic in a homogeneous absorptive medium can then simply be approximated as:

$$I_q(L) \approx N_a^2 \left| \chi^{(q)} E_0^\gamma \right|^2 \left(\frac{1 + e^{-2\alpha L} - 2e^{-\alpha L} \cos \Delta k L}{\alpha^2 + \Delta k^2} \right) \tag{3.45}$$

The nonlinear source term scales with $S_q = \left| \chi^{(q)} E^\gamma \right|^2$ where $\gamma \approx 5$ [41, 62]. The nonlinearity $\chi^{(q)}$ is a function of the harmonic order q and can be set to 1 for a qualitative evaluation of the HHG build-up. In the experiments presented in this thesis, where high-harmonics are generated in a gas-filled waveguide with a z-dependent gas density and driver field amplitude, equation (3.41) has to be approximated numerically. This is straightforward under a few assumptions. The first assumption is that most of the high order harmonics are generated from parts of the driver beam propagating in a finite number of waveguide eigenmodes. In fact, since the propagation loss in eigenmodes of a capillary waveguides or a PCF increases with the order and scales with u_{mn}^2, it can be assumed that harmonics are, to a large extent, generated from parts of the driver beam propagating in the fundamental mode, if the driver beam is preferentially coupled into the funda-

mental waveguide mode. For the experiments described in this chapter, this was ensured by choosing the correct coupling parameters for launching the driving laser beam into the NC-PCF as described in the methods section. Since the nonlinear source term S_q scales approximately as E^7, it can also be assumed for a qualitative evaluation of the build-up that high-harmonics are generated close to the longitudinal axis of the waveguide where the intensity of the fundamental LP_{01} mode is maximal. Hence, the on-axis buid-up of harmonic radiation is most significant and the radial density gradient in the waveguide can be neglected. Furthermore, it can also be assumed under the same argument that most of the harmonics are generated at instances close to the peak field amplitude of the driver pulses. Under this assumption, the temporal variation of the ionization fraction can be neglected and can be replaced by an approximated ionization fraction $\eta \approx \eta(t_0)$. For the assumed longitudinal pressure distribution described by equation (3.40), the inner integrals in equation (3.41) can be calculated exactly. The outer integral can then be approximated numerically by using the global adaptive quadrature method.

The intensity build-up $I_{21}(z)$ of H21 at the entrance of the NC-PCF is illustrated in Fig. 3.8. In order to illustrate the HHG build-up in NC-PCF type I with a uniform gas-fill at different pressures $P_0 = P_L$, it is assumed that a single driver pulse excites a single or a pair of mode(s) at the entrance of the NC-PCF. The build-up model indicates that phase-matched HHG is possible at $P_0 = P_L = 970\,\text{mbar}$ in case the driver pulse propagates in a single waveguide mode figure 3.8a. In case of mode beating between the LP_{01} and LP_{13} mode a strong increase in the build-up efficiency as a result of MM-QPM is observed for $P_0 = 200\,\text{mbar}$ (Fig. 3.8b). The phase-matched build-up at $P_0 = 970\,\text{mbar}$ is less efficient in this case since the driver pulse intensity is modulated longitudinally and regions with beating nodes don't contribute to the build-up. Figure 3.8c/d shows the integrated HHG build-up at the exit of the NC-PCF for case of Fig. 3.8a/b. Three different line-outs of Fig. 3.8a/b at different pressures are shown in

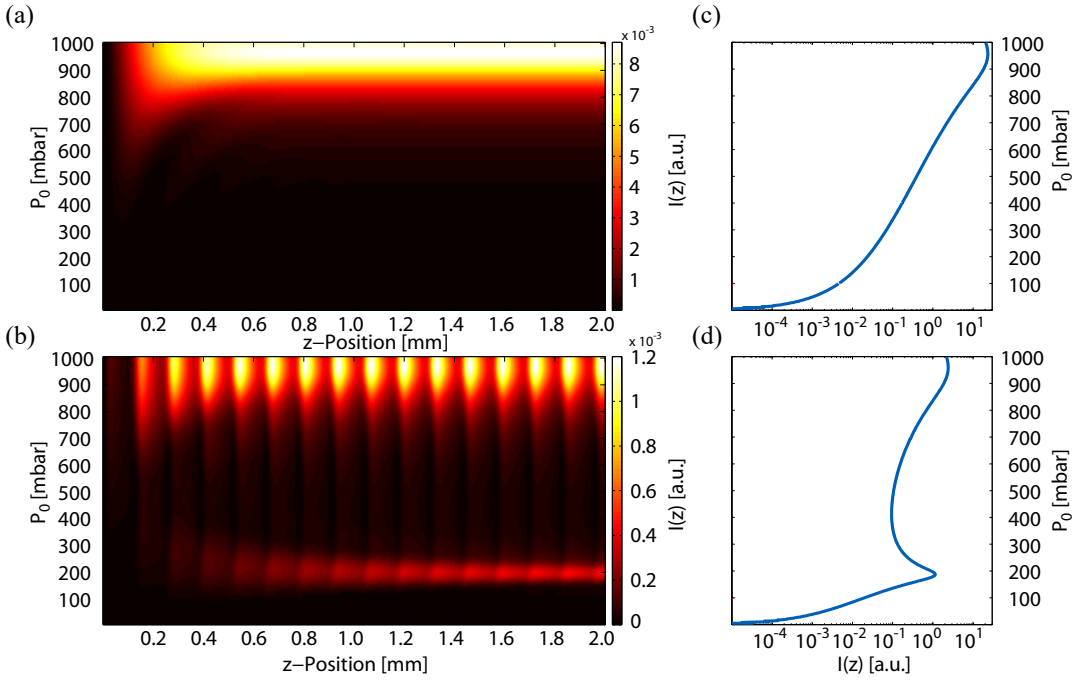


Figure 3.8: **Modeled on-axis HHG build-up as a function of gas pressure for a uniform gas-fill** $P_0 = P_L$. Build-up of harmonic H21 is simulated in a capillary waveguide with a core diameter of $a = 22.5\,\mu m$. (a) Intensity build-up of H21 at different pressures without MM-QPM. Phase matching of H21 is possible at $P_0 = 970\,mbar$. (b) Build-up of H21 at different pressures in case of beating between the LP_{01} and LP_{13} mode. The enhanced HHG efficiency around $P_0 = 200\,mbar$ is the result of MM-QPM. (c) Integral on-axis build-up of H21 at the exit of the NC-PCF without MM-QPM. (d) Integral on-axis build-up of H21 at the exit of the NC-PCF with MM-QPM settings as in (b).

Fig. 3.9 for the case of phase-matched and absorption limited HHG, for the case of HHG with MM-QPM and the non phase-matched case at $P_0 = 200\,mbar$. The green curve in figure 3.9 shows the HHG build-up expected for QPM [79].

Influence of the pressure gradient

In order to understand the influence of the pressugre gradient, the HHG build up is simulated by integrating equation (3.41) while assuming that the density gradient inside the NC-PCF type I is of the form (3.40). Figure 3.10 shows the on-axis HHG yield for different input pressures P_0 for two situations: Figure 3.10a corresponds to figure 3.8b while figure 3.10b shows the situation with a varying gas density

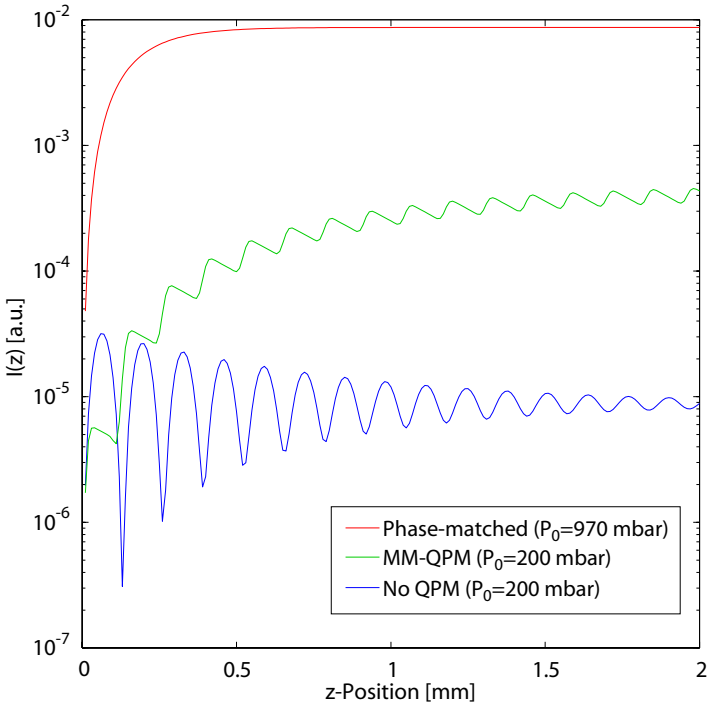


Figure 3.9: **Modeled on-axis build-up of H21 as a function gas pressure for a uniform gas-fill** $P_0 = P_L$. Non-phase-matched build-up of H21 at $P_0 =$ 200 mbar without mode beating (blue curve). At the same pressure and with MM-QPM, the build-up efficiency is strongly enhanced (green curve). The red curve shows the build-up of H21 in case of phase-matched HHG.

inside the NC-PCF. It can be seen that the z-Position inside the NC-PCF where the HHG build-up is enhanced varies according to the applied input pressure P_0 at the entrance of the NC-PCF. In order to localize the region where MM-QPM is achievable in the NC-PCF type I section at position $z = L = 22.5\,\text{mm}$, the input pressure had to be set to around 800 mbar indicated by the green box in Fig. 3.10.

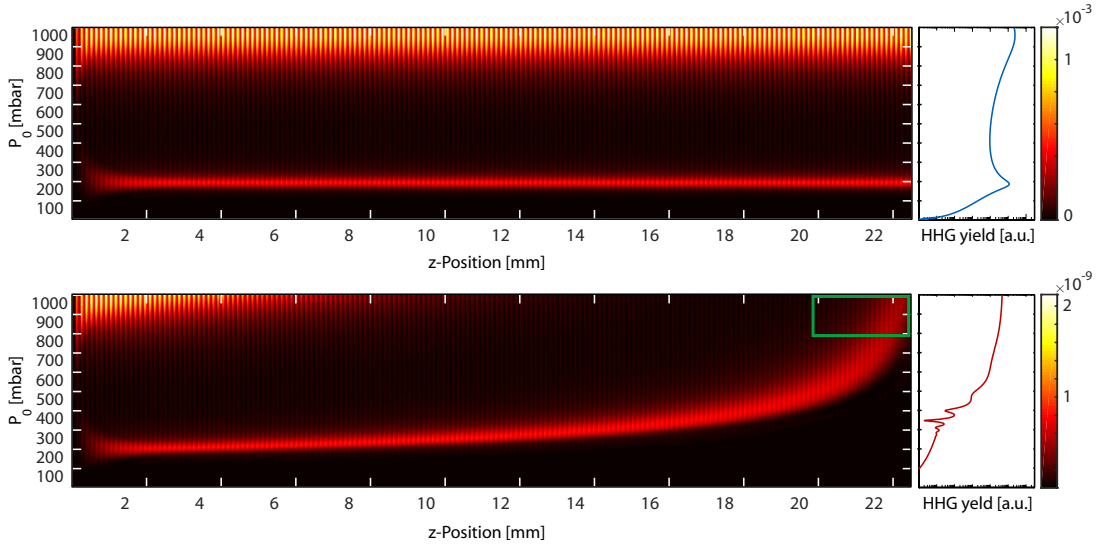


Figure 3.10: **Modeled on-axis HHG build-up as a function of gas pressure**. Build-up of H21 in a PCF type I. a) Intensity build-up of H21 at different pressures with MM-QPM and a constant gas density along the NC-PCF. Phase matching of H21 is possible at $P_0 = 970\,\text{mbar}$. b) On-axis build-up of H21 in the presence of density gradient. For a fixed P_0, MM-QPM is achieved at a specific z-position in the NC-PCF. For the length of the NC-PCF section in the present experiment (22.5 mm), enhancement due to MM-QPM at the NC-PCF output $z = 22.5\,\text{mm}$ is predicted for $P_0 > 800\,\text{mbar}$ (green box).

Chapter 4

HHG in Photonic Crystal Fibres

4.1 Concept

4.1.1 Background

Compact, bright sources of coherent extreme ultraviolet (XUV) radiation open new opportunities for applications which require a high average photon flux such as lithography and coherent imaging. One approach for generating such light sources is high-harmonic generation (HHG) [41, 43] in which femtosecond-duration laser pulses from high repetition rate, high average power near-infrared (NIR) lasers are focused into a noble gas. Efficient operation of HHG sources demands a sufficiently high peak intensity. When using mJ-level NIR driving pulses at low repetition rates, conversion efficiencies of $10^{-6} - 10^{-5}$ have been reached [69, 80, 81] corresponding to a XUV photon flux per harmonic of 10^9 photons s^{-1}. When using high pulse repetition rate laser systems, pulse post-compression and stronger focusing of the driving pulses is necessary due to the comparatively low pulse energy (in the range of tens of microjoules) currently deliverable from ultrafast, high average power laser systems such as thin-disk [82], fibre-lasers [83] or optical parametric chirped-pulse amplifiers (OPCPA) [84]. As a result of tight focusing

the interaction volume, and hence the number of high-harminic photons which can be generated, is greatly reduced [85]. In the presence of phase-matching, re-absorption of generated high-harmonic photons in the generation medium is the predominant limiting factor to the conversion efficiency, since it limits the useful generating medium length [80]. Studies have shown that in the tight-focus regime the so-called HHG absorption limit can be reached [86, 65] but elaborate target geometries and high pumping speeds are required to maintain high vacuum elsewhere in the beamline. In cases where the density required for absorption-limited generation cannot be reached, the HHG efficiency can drop below 10^{-10} [87]. These limitations can be mitigated by coupling the laser into a gas-filled hollow core optical waveguide with a small core diameter d in which the light propagates in confined waveguide eigenmodes [22]. However, the transmission loss of the driving laser at wavelength λ_0 in conventional capillary waveguides scales as λ_0^2/d^3 (cf. equation (2.36)) and quickly becomes a limiting factor. Hollow-core PCF (HC-PCF) such as the "Kagome" type PCF or NC-PCF [88] exhibit significant lower guiding losses compared to a capillary with similar d due to antiresonant guiding [29].

It has recently been demonstrated that nonlinear compression of pulses from a Ti:Sapphire laser can be performed in helium-filled Kagome-PCF ($d = 46\,\mu m$) yielding 15 fs, 50 µJ pulses which were subsequently used to generate high-order harmonics up to the 29^{th} order (H29, $q = 29$) in an argon gas-jet, placed directly behind the exit of the PCF [19]. High-harmonic generation up to H13 of an 800 nm driving laser has also been demonstrated with 4.2 µJ, 30 fs pulses inside a Kagome-PCF ($d = 15\,\mu m$) in a proof of principle experiment [5]. However, in this case the conversion efficiency (10^{-9}) was low due to imperfect phase matching and low coupling efficiency of the driver into the PCF.

In this chapter, HHG driven with few-µJ-level NIR pulses in NC-PCF is investigated. The conversion of NIR driving radiation into photons of energies up to

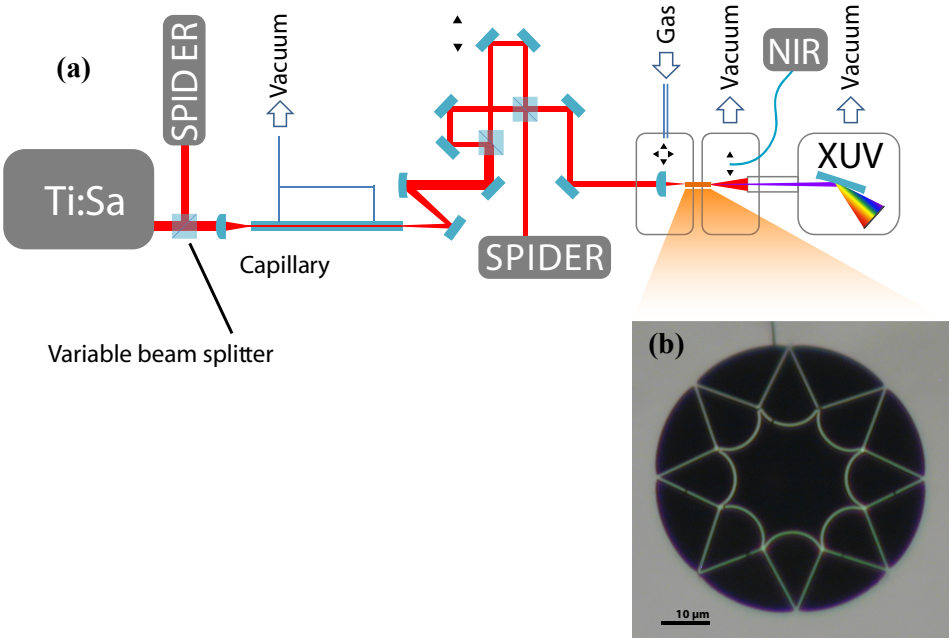


Figure 4.1: Experimental setup. (a) A Ti:Saphire laser (KMLabs) delivers 1 mJ, 30 fs pulses at a repetition rate of 1 kHz and a central wavelength of 785 nm. The pulse duration is measured with spectral phase interferometry for direct electric field reconstruction (SPIDER). The pulse energy is reduced to between 1 µJ and 15 µJ by means of a variable beam splitter. After spatial filtering in an evacuated capillary, a pair of pulses is generated in a Mach-Zehnder interferometer fitted with a variable delay stage in one beam path. The pulses are then coupled into a section of a NC-PCF($L = 22.5$ mm) by means of a lens mounted on a XYZ-stage. The NC-PCF is filled with Ar or Ne gas at various pressures. The high-harmonic beam is analyzed in a flat-field XUV spectrometer (XUV) and the residual driving laser is analyzed in a fibre-coupled near-infrared spectrometer (NIR). (b) Microscope image of the NC-PCF used in the present experiment. The diameter of the hollow core (shortest distance between two opposite hypocycloids) is 22.5 µm.

61.6 eV is presented. Furthermore, it is demonstrated experimentlally that multi-mode quasi-phase-matching (MM-QPM) [66, 89] of HHG in a NC-PCF leads to enhancement of the HHG signal by almost two orders of magnitude. Additionally, Phase-matched HHG in a NC-PCF is demonstrated using $30 - 50$ µJ driving pulses.

4.1.2 Experimental Setup

Figure 4.1 shows, schematically, the setup employed for the experiments presented in this chapter. Harmonics are generated in gas-filled NC-PCF with different core diameters and at different pulse energy regimes of the NIR driver pulses. The specifications of the different NC-PCF types can be found in table 4.1. In the pulse energy regime below 15 µJ, HHG is performed in an argon and neon filled NC-PCF (type I, $d = 22.5\,\mu m$). This type of antiresonant guiding PCF, shown in Fig. 4.1b, has a minimum attenuation of $0.06\,dB\,m^{-1}$ at 690 nm with attenuation below $0.3\,dB\,m^{-1}$ for wavelengths between 610 nm and 840 nm [90]. Non-phase-matched HHG was explored with an argon and neon filling and the generated XUV harmonic spectra were measured for different driver pulse energies together with the NIR spectra of the residual driving pulses after transmission through the gas-filled NC-PCF section. Furthermore, IDC-QPM was employed to enhance the HHG conversion efficiency in NC-PCF of type I filled with argon gas. HHG employing NIR laser pulses with higher pulse energy of greater than 30 µJ was explored in a different type of NC-PCF (type II, GLOphotonics PMC-C-650/2000-7C, $d = 53\,\mu m$), which provides low loss transmission of less than $0.15\,dB\,m^{-1}$ for wavelength around 800 nm. This NC-PCF has a larger core size and allows phase-matching of the harmonics around H23 in argon at pressures of approximately 150 mbar due to the lower waveguide dispersion. For the different experiments, the NC-PCF were mounted as illustrated in Fig. 3.6.

	Type I	Type II
Diameter d	22.5 µm	53 µm
Transmission window	610 nm − 840 nm	500 nm − 1700 nm
Attenuation	$0.06\,dB\,m^{-1}$	$< 0.15\,dB\,m^{-1}$
Drive pulse energy	5 µJ − 15 µJ	30 µJ − 50 µJ
Gas	Neon, Argon	Argon
Pressure	$P_L < P_0 = 800$ mbar	$P_L = P_0 < 200$ mbar

Table 4.1: Types of NC-PCF used in the experiments.

.

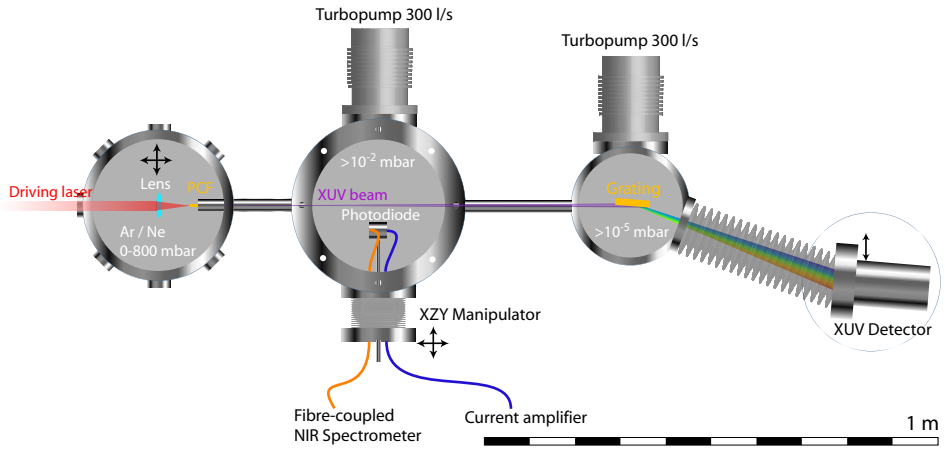


Figure 4.2: Experimental setup for HHG.

High-harmonic generation was driven with $25 - 30\,\mathrm{fs}$ (FWHM) pulses from a Ti:Saphire laser system operating at a pulse repetition rate of 1 kHz. The pulse duration was measured by using spectral phase interferometry for direct electric field reconstruction (SPIDER). Two commercial spider devices (A.P.E, FX and FC SPIDER) were used for pulse characterization. The driver pulses were characterized for the first time directly behind the output of the driving laser using a FX SPIDER. In order to pre-compensate for the group delay dispersion (GDD) of the optical setup, the group delay of the pulses was measured and set to approx. $-600\,\mathrm{fs}^2$ by adjusting the grating compressor of the Ti:Sapphire chirped-pulse amplifier (CPA). The pulses where then characterized for as second time further downstream using an FC SPIDER. The experimental setup is shown in figure 4.1a.

Linearly polarized laser pulses from the CPA were attenuated to an energy of 5–50 µJ and spatially filtered in a one meter long, evacuated glass capillary fibre with a diameter of 150 µm. A pair of pulses was then generated using a delay line in the configuration of a Mach-Zehnder interferometer. One arm of the interferometer was equipped with a retro-reflector mounted onto a motorized translation stage. The arm could also be blocked in order to drive HHG with only a single laser pulse. The relative delay could be adjusted by changing the position

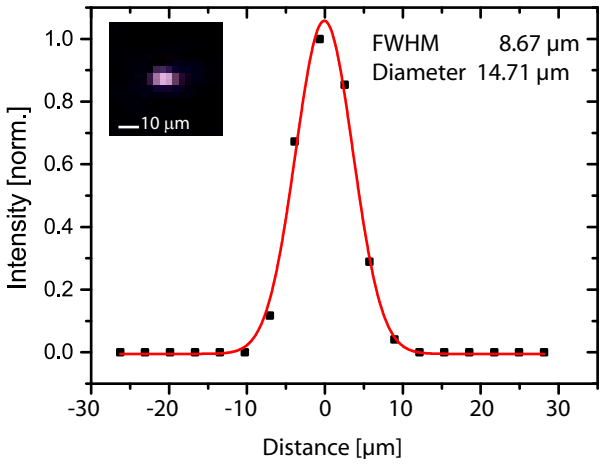


Figure 4.3: Focus characterization. Measured transverse fluence profile of the driving laser at the focus of a $f = 75\,\text{mm}$ lens along an axis passing through the peak of the focal spot. The transverse beam profile was measured using a CCD camera. The measured $1/e^2$ beam diameter was $w_0 = 14.71\,\mu\text{m}$. This spotsize meets the optimal coupling conditions $\chi = 0.64$ of the gaussian beam into the fundamental mode of the NC-PCF.

of the retro-reflector. The position accuracy of the servo motor (Thorlabs Z825B) was $\pm 1\,\mu\text{m}$. The laser pulses were then coupled into a section of NC-PCF type I by means of a lens ($f = 75\,\text{mm}$) mounted on an XYZ translation stage. This focal length was selected in order to meet the optimal coupling conditions of the laser beam into the fundamental waveguide mode of the NC-PCF. For NC-PCF type I, this is given for a beam waist at the entrance to the NC-PCF of $w_0 \approx 14.4\,\mu\text{m}$. The focal spot size at the entrance of the NC-PCF was characterized both, using a CCD camera and the knife-edge method. Figure 4.3 shows a measured spot size of $14.71\,\mu\text{m}$ of the driving laser beam focused into the entrance of NC-PCF type I. In order to optimize the coupling of laser power into NC-PCF type II, a lens with $f = 150\,\text{mm}$ was used resulting in a larger spot size of approximately $33\,\mu\text{m}$.

A high coupling efficiency and a resulting transmission of approximately 90% of driver power through the NC-PCF sections was achieved. The section of PCF type I was mounted between two vacuum chambers as illustrated in Fig. 3.6a. The first chamber was filled with Ar or Ne gas at room temperature and pressures between $0\,\text{mbar}$ and $800\,\text{mbar}$ while a vacuum of $(1 \times 10^{-2}\,\text{mbar} - 1 \times 10^{-5}\,\text{mbar})$ was

maintained throughout the second by using two $300\,\mathrm{l\,s^{-1}}$ turbomolecular pumps. The HHG setup is depicted in Fig. 4.2. The first to the left side is filled with gas and hosts the lens used to couple the laser beam into the NC-PCF section which was mounted between first and second chamber. The second chamber in the middle of the setup was evacuated using a turbomolecumlar pump. A XUV photodiode and a multi-mode optical fibre were mounted on a linear translation stage and could be extended into the beamline in order to measure the XUV flux and the spectrum of the NIR driving beam after propagation in the NC-PCF. The second and third chamber were separated by an apperture and an approximately 40 cm long vacuum tube which acted as a differential pumping stage.

Since gas was introduced into only one end of the PCF, the density of gas varied within it. The variation of this density can be calculated, assuming that the flow is turbulent and isothermal. In this case, the gas flow through the core resembles the flow of a compressible gas through a cylindrical pipe with diameter d and length L [78]. In this regime the different gas pressures at the entrance and exit of the NC-PCF, P_0 and P_L lead to a longitudinal pressure profile along the spatial coordinate z of the form approximated by equation (3.40) and illustrated in Fig. 3.7. This pressure gradient causes the coherence length to vary continuously along the fibre as described in chapter 3.2.2. Furthermore, the strength of the XUV emission along z depends on the number of XUV emitters present at the position z, whereas the reabsorption of the radiation obeys Beer-Lambert's law and decreases with decreasing gas density. Since a high entrance pressure $P_0 = 0.8\,\mathrm{bar}$ was used in the present experiment, the absorption length is less than 100 µm throughout 95% of the fibre length [76]. Hence, most of the observed XUV radiation was generated close to the exit of the NC-PCF.

The XUV output of the NC-PCF was analyzed using a flat field XUV spectrometer. The spectrometer comprised an aberration-corrected concave grating (Hitachi grating model 001-0640) and a XUV detector. The detector consisted of

two stacked microchannel plates (MCP) mounted in front of a phosphorous screen which was imaged by using a CCD camera. Details of the spectrometer used in the present experiment are given in [8]. The average photon flux was measured with a XUV photodiode which was mounted behind a 400 nm thick Al-filter to block the residual driving laser (also refer to chapter 4.4). Additionally, a fibre-coupled NIR spectrometer (Ocean Optics USB 2000) was used to measure the spectrum of residual driving laser beam after propagation through the NC-PCF sections. For the experimental investigation of phase-matched HHG in a NC-PCF, the NC-PCF with $d = 53\,\mu m$ was mounted in front of a pinhole. This method enabled separating the high pressure in the first experimental chamber from the high vacuum of the second and third vacuum chamber while enabling filling the NC-PCF with a constant pressure and allowing for transmission of the generated harmonic radiation into the XUV spectrometer. The larger core diameter of the NC-PCF allowed for phase-matching at low gas pressures of around 150 mbar. However, even at this low pressure, the gas leaking though the 50 µm pinhole aperture into the second and third vacuum chambers caused a substantial gas load onto the pumping system and as a result, the gas filling pressure P_0 could not be increased significantly beyond the phase-matching pressure.

4.2 Non-phase-matched HHG in a PCF

Using an argon gas fill, harmonics between H19 and H23 were observed when single, 30 fs, 5 µJ drive pulses were launched into the NC-PCF. For neon gas, the threshold pulse energy at which the same harmonic orders were observed lies at 10 µJ, and increasing the drive pulse energy to 15 µJ yielded harmonics with energies up to 61.6 eV as shown in Fig. 4.4a. These are, to the author's knowledge, the highest photon energies reported to date for HHG in a NC-PCF. Figure 4.4a shows a typical spectrum with peaks located at high-order odd-integer fractions of

the fundamental driver wavelength, which is a clear signature of HHG [41]. The cut-off energy of 61.6 eV is in good agreement with the cut-off predicted by the semi-classical model of HHG [51] for a driver peak intensitiy of $2.3 \times 10^{14}\,\mathrm{W/cm^2}$. The harmonic spectrum and the spectrum of the driving laser at the exit of the Ar-filled NC-PCF are shown in Fig. 4.4b/c for a range of pulse energies. Spectral shaping of the driver pulse spectrum was observed for driver pulse energies above 7 µJ. This effect is caused by pulse self-compression and subsequent blue-shift which has been discussed in the literature [18, 91] and in chapter 2.2.2. The ionization-induced self-phase-modulation (SPM) of the pump pulses differs from SPM at lower pulse intensities where material ionization can be neglected. At lower light intensities, SPM is a third order nonlinear-effect. However, at high light intensities, material ionization becomes significant and the free electrons in the plasma exhibit a high polarizability. Since the ionization rate is a highly nonlinear function of the light intensity, ionization cause the refractive index of the gas to change rapidly. As the average recombination time for the liberated electrons is much longer than the drive pulse duration, ionization can be regarded as an irreversible process. This results in an asymmetric broadening of the pulses with more wavelength components being generated at the blue end of the drive pulse spectrum. The magnitude of the resulting blue-shift is proportional to the ionization rate of the gas, and therefore larger at higher peak intensities [18]. It should be noted that experiments in an evacuated NC-PCF did not yield any spectral broadening or reshaping of the input beam after propagation in the fibre even at pulse energies ten times higher than used for HHG. This indicates that the silica glass of the NC-PCF walls does not contribute to the nonlinear response observed with an argon fill. As illustrated in Fig. 4.4b, the blue-shift of the driver translates onto the harmonic spectrum, yielding an XUV quasi-continuum at the highest input pulse energies. This behavior is known from theoretical studies and experiments reported in [19, 92]. It should be noted that no blue-shift of the driver

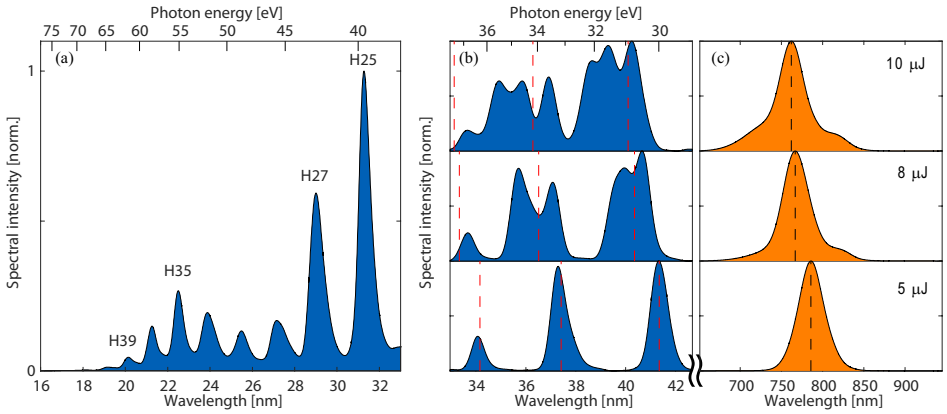


Figure 4.4: Measured XUV and IR spectra. (a) Harmonic spectrum generated in Ne at an inlet pressure of 0.8 bar with single 15 µJ pulses. Harmonics up to H39 (20 nm, 61.6 eV) are detected. (b) Harmonic spectrum (H19-23) in Ar at a pressure of 0.1 bar and (c) spectrum of the driving laser measured at the exit of the NC-PCF for the same three pulse energies used in Fig. 4.4b. The spectral broadening and blue shift of the driver due to nonlinear propagation in the NC-PCF is transferred to the harmonic spectrum. The red dashed lines indicate the central wavelength of the transmitted driving laser (Fig. 4.4c, black lines) divided by harmonics orders $q = 19, 21, 23$.

laser was observed when the NC-PCF was filled with neon gas.

The average spectral flux was found to be approximately 1.14×10^6 photons $\mathrm{s}^{-1}\,\mathrm{nm}^{-1}$ in H25 (1×10^3 photons per drive pulse) generated in Ne with 15 µJ pulses, and an average flux of less than 5.9×10^5 photons $\mathrm{s}^{-1}\,\mathrm{nm}^{-1}$ in H23 generated in Ar with 10 µJ pulses. The low conversion efficiency of 1×10^{-10} is mainly the result of poor phase-matching.

4.3 Quasi-phase-matched HHG in a PCF

Intermodal delay-controlled QPM (cf. section 3.2.2) was achieved by coupling into the PCF both driver and control pulses with a specific relative delay. It should be noted that the alignment of the drive beam focus at the entrance of the NC-PCF was slightly readjusted for $\chi \neq 0.64$ in order to sufficiently excite higher order waveguide modes. In Fig. 4.5c the integrated spectral intensity in a window spanning from H21 to H25 is shown as a function of delay τ between drive and control

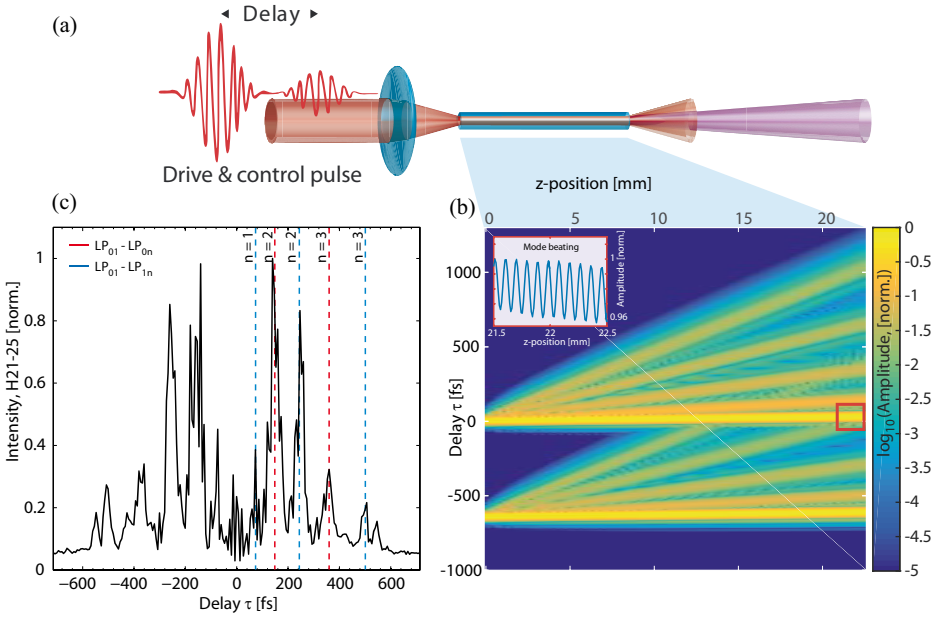


Figure 4.5: Intermodal-delay-controlled QPM. (a) Concept and (b) simulation results of IDC-QPM for a set of five low-order waveguide modes (LP01-LP05). A control and a drive pulse are launched into a gas-filled section of a NC-PCF with a relative delay. Modal dispersion of the waveguide results in a temporal separation of higher order spatial modes as the pulses propagate along the NC-PCF. Overlap of one higher order mode of the control pulse with the fundamental mode of the drive pulse causes mode beating at the exit of the NC-PCF and rapid longitudinal modulation of the combined electric fields (inset). The amplitude modulation depth, 5% in the present case, is set by the relative intensity of the beating modes at the exit of the NC-PCF. (c) Experimental results: Intensity of H21-25 as a function of delay τ between drive and control pulse. The dashed lines indicate, for a propagation distance of $z = 22.5\,\mathrm{mm}$, the difference in group delay between various higher-order modes and the fundamental mode.

pulses, both attenuated to 5 µJ. The delay was scanned by changing the length of one interferometer arm. The scan-step size was set to 2 µm. At small relative delays $|\tau| < 50\,\mathrm{fs}$, the LP_{01} modes of the drive and control pulse overlap and the modulation in the brightness of H21-H25 resembles a high-order interferometric autocorrelation of drive and control pulse. The peaks located around the temporal overlap at $|\tau| > 50\,\mathrm{fs}$ can be attributed to the temporal overlap of the LP_{01} mode of the driver pulse with the LP_{0n} and $LP_{1n} (n = 1, 2, 3)$ modes of the control pulse close to the exit of the NC-PCF. Since in this work the drive and control pulses are identical, and both pulses are coupled into almost identical waveguide modes, the

delay-dependent variation of the harmonics intensity is symmetric around $\tau = 0$. For $\tau < 0$ the control pulse is coupled into the NC-PCF first while harmonics are generated when the drive pulse arrives, whereas the situation is reversed for $\tau > 0$. Figure 4.5c shows, for a propagation distance of $z = 22.5\,\mathrm{mm}$, the group delays between various modes and the fundamental mode determined by the intermodal delays τ_{mn}. These are symmetric around $\tau = 0\,\mathrm{fs}$ and are marked with dashed lines for positive delays only. It can be seen that the harmonic intensity shows clear maxima for $\tau = \tau_{mn}$, confirming the model of IDC-QPM. It should be noted, that the hight of the peaks in Fig. 4.5c does not reflect the quantitative HHG enhancement. In order to determine the HHG enhancement, the delay had to be fine-tuned around the individual peaks while recording the entire HHG spectrum for each peak position. The comparison of the measured harmonic spectra for different IDC-QPM delays, show excellent agreement to the model predictions. Figure 4.6 shows a comparison of the measured harmonic spectrum H19-H29 in argon at an input pressure of 0.8 bar with IDC-QPM for the beating of the LP_{01} mode of the drive pulse with the LP_{02} mode of the control pulse and for the beating of the LP_{01} and LP_{21} mode with the relative harmonic brightness predicted by the build-up model. It can be seen that experiment and theory are in good agreement.

Figure 4.7 shows the harmonic spectrum (H21-H25) generated with pairs of 5 µJ pulses when the delay is precisely tuned to the enhancement peak at $\tau = 160\,\mathrm{fs}$ in Fig. 4.5c. Compared to the case when HHG is driven with single 10 µJ pulses (red curves), a brightness enhancement of H21-25 by a factor of approximately 60 was observed. In the present experiment, a comparatively long section of NC-PCF was chosen in order to allow for a good temporal mode separation. In order to localize sufficient gas pressure for HHG at the exit of the NC-PCF, the front was held at 800 mbar causing strong XUV reabsorption throughout almost the entire length of the NC-PCF. Hence, the benefits of using the PCF to purely extend the

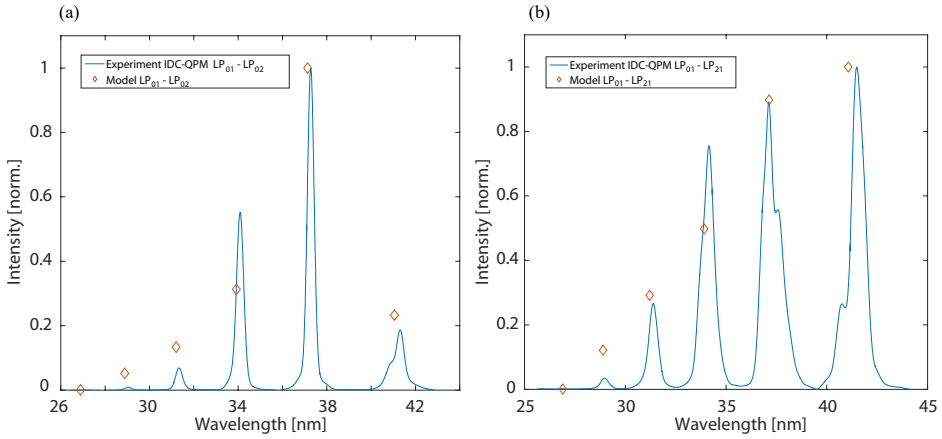


Figure 4.6: **Experimental HHG spectra and model prediction**. (a) Harmonic spectrum with IDC-QPM of LP_{01} and LP_{02} mode (blue line) and relative harmonic brightness predicted by the QPM model set out in chapter 3.2.2 (orange diamonds). (b) Experimental Harmonic spectrum with IDC-QPM of LP_{01} and LP_{21} mode (blue line) and model predictions (orange diamonds).

interaction length were limited. To understand the effect of the density gradient in the NC-PCF, the relative HHG efficiency was calculated for uniform and non-uniform gas fills, with and without MM-QPM according to the model presented in chapter 3.2.2. Figure 4.8 shows the modelled on-axis HHG yield as a function of input pressure. The model indicates that a uniformly filled NC-PCF would enable IDC-QPM at significantly lower input pressures while at the same time resulting in an additional enhancement of the HHG yield by up to an order of magnitude.

4.4 HHG efficiency

The response of the XUV spectrometer was calibrated for photon number, by measuring the XUV photon flux with a XUV photo diode (Opto Diode Corp. AXUV100Al) and a ultra-low-noise, femtoampere transimpedance amplifier (FEMTO LCA-2-10T). The XUV photodiode has a quantum efficiency of nearly 100% for photons below a photon energy of 4 keV. This diode is sensitive in the wavelength range 17 nm to 80 nm and is coated with a 150 nm thick aluminium layer to block

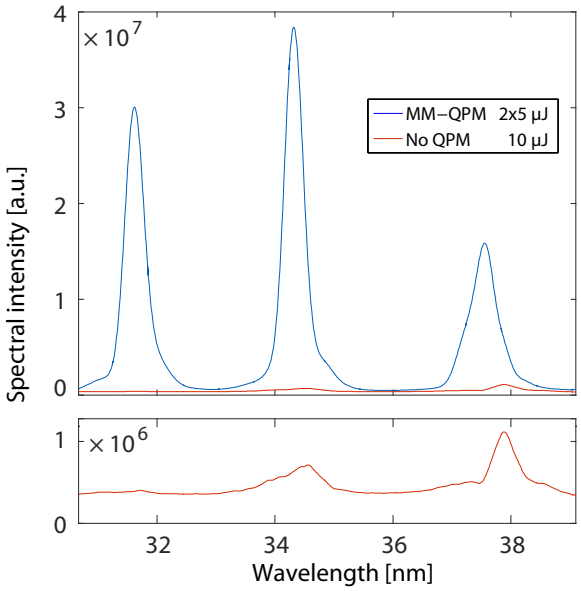


Figure 4.7: Enhancement of the HHG flux due to MM-QPM. Experimental harmonic spectrum H21–H25 driven with pairs of 5 µJ pulses (delay $\tau = 190$ fs) with IDC-QPM (blue curve) and driven with single 10 µJ pulses without any QPM (red curves); the bottom panel shows the same single-pulse data but rescaled. The brightness enhancement of H21-25 by a factor of 60 is the result of IDC-QPM.

NIR photons. Additionally, a free standing 400 nm thick aluminium filter was mounted in front of the diode to provide additional filtering of the NIR radiation. The Al-filter has a thickness tolerance of ±10%, as specified by the manufacturer (LEBOW). The XUV transmission of the free standing Al-filter was measured by comparing the photon count on the XUV spectrometer with and without the filter mounted in front of the spectrometer entrance aperture. The total XUV transmission was found to be approximately 10%. This figure is in good agreement with the estimated transmission for the case that all aluminium surfaces were covered with a 10 nm thick aluminium oxide layer which acts as a strong XUV absorber. The total XUV transmission through the free-standing aluminium filter and the aluminium coating of the photodiode is estimated to be $(3.5 \pm 0.3)\%$.

With IDC-QPM a flux of 10^8 photons per second per harmonic was measured, averaged over H17-H23. The measurment error resulting from the Al-filter transmission tolerance, the accuracy of the photocurrent amplifier and the oscilloscope

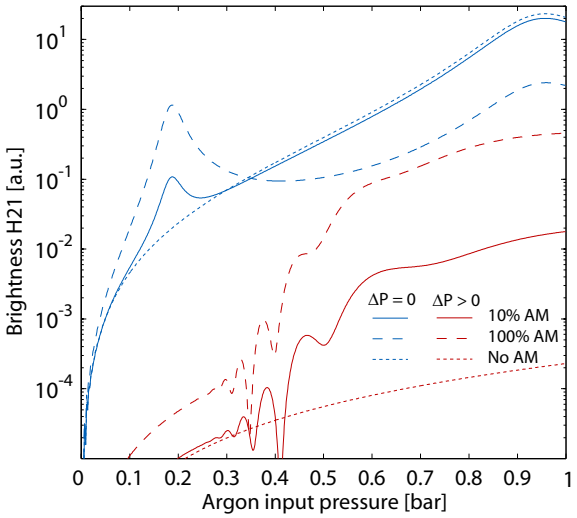


Figure 4.8: Modelled on-axis yield of H21 in the NC-PCF used in the present experiment for beating of the LP_{01} with LP_{13} mode in case of a uniform argon pressure in the NC-PCF, $\Delta P = (P_0 - P_L) = 0$, (all blue lines) and in case of a longitudinal pressure profile, $\Delta P > 0$ (all red lines). In both cases, the largest brightness enhancement is expected for beating of the LP_{01} with LP_{13} mode assuming 100% amplitude modulation (AM) in case of equally intense modes (dashed lines) and 10% AM in case of a weak LP_{13} mode (solid lines). Compared to the case where a pressure gradient is present in the NC-PCF, as in the present experiment, the model suggests further enhancement due to IDC-QPM at a uniform filling pressure of approximately 200 mbar (solid & dashed blue lines). The dotted lines correspond to the case when drive and control pulse propagate in the same mode without mode beating. The blue dotted line indicates full phase matching at a uniform pressure close to 1 bar. Even though, the HHG conversion efficiency is highest at this pressure, the resulting high gas load is experimentally challenging.

used to measure the output of the amplifier is estimated at approximately 16%. This total flux corresponds to an XUV yield of approximately 10^5 photons per harmonic per laser shot and a conversion efficiency of launched NIR driving power into a single harmonic order of approximately 10^{-7}. This is about two orders of magnitude higher than the HHG conversion efficiency in HC-PCF reached in previous experiments [5]. Compared to unphasematched HHG driven directly with few-microjoule pulses from 50 - 100 kHz Ti:sapphire lasers [85, 93], the efficiency reached in the present experiment is approximately one order of magnitude higher and is comparable to the efficiency of HHG directly driven with Yb-based fibre-laser system at a 100 kHz pulse repetition rates [86]. On the other hand, the conversion efficiency in the present experiment is one order of magnitude lower than quasi-phase-matched HHG in capillaries with mJ-level driving pulses [69] or phase-matched HHG in a tightly focused NIR beam [65]. In [65], it was shown that in a free focused beam geometry the phase matching pressure is inversely proportional to the square of the spot size, hence a very high pumping speed is required in order to maintain a good vacuum in the experimental chamber. This can be a substantial experimental limitation. Phase-matching HHG in a focused NIR beam with a size similar to the mode field diameter of the NC-PCF type I used in the experiment presented in this chapter would require pumping speeds well exceeding $1 \times 10^3\,\mathrm{l\,s^{-1}}$ in order to maintain a vacuum below 1×10^{-2} mbar in the target chamber [65].

In the present demonstration of IDC-QPM, no attempt was made to optimize the coupling of drive and control pulse into specific fiber modes e.g. by using a spatial light modulator [94]. Such modifications to the experiment have the potential to improve the overall HHG efficiency since all the available driving laser power could be preferentially coupled into fiber modes involved in MM-QPM. Furthermore, using drive and control pulse with orthogonal polarization could further improve the MM-QPM performance as proposed in [89]. This will

be explored in chapter 5.

4.5 Phase-matched HHG in a PCF

To demonstrate phase-matched generation of XUV radiation in a PCF, HHG was driven with $30-50\,\mu J$, 30 fs pulses in a argon filled NC-PCF type II. The large core diameter of this fibre enables phase-matching HHG at a wavelengths of around 30 nm at a low gas pressure of around 150 mbar. The low gas pressure allowed for application of the gas injection method described in section 3.2.2 and depicted in Figure 3.6b. Pressure controlled phase-matching was demonstrated through a pressure scan of the input pressure in steps of 10 mbar using a automated pressure regulator (Tescom, ER5000) while measuring the XUV photon yield in H21-25. The results are shown in figure 4.9 together with the predictions by the phase-matching model described in section 3.2.2. It can be seen that the experimental data shows two clear maxima. The first maximum located around 150 mbar can be explained by phase matching of the harmonics generated in the fundamental LP_{01} mode of this NC-PCF (blue curve). The second maximum located at around 120 mbar shows excellent agreement with the build-up model if beating of LP_{01} and LP_{02} mode is assumed (red line). For these experiments, only a single drive pulse was used, and hence the delay between the two modes was 0 fs. Due to the lower waveguide dispersion, the temporal walk-off of the modes in NC-PCF type II is significantly lower compared to NC-PCF type I, resulting in a longitudinally-extended modal overlap region. Additionally, the contribution of the higher order modes ($LP_{0n}, n > 2$) to MM-QPM in this wavelength region is negligible in NC-PCF type II, since no good matching of beating length and coherence length exist at an estimated ionization fraction of approximately 0.5-1.5%. The good agreement between experimental data and the predictions further supports the simple MM-QPM model set out in section 3.2.2.

The measured XUV yield in H21-H25 under phase-matching conditions, was in the order of 10^8 photons per second per harmonic equivalent to an effective conversion efficiency of approximately 10^{-8}. This low efficiency, compared to the IDC-QPM case in fibre type I, can be explained by substantial reabsorption of the emitted XUV photons in the dense argon gas in the gap between NC-PCF and pinhole and in the second vacuum chamber. The pressure difference between first and second vacuum chamber creates a supersonic gas jet by adiabatic expansion of argon through the 50 µm pinhole. It is difficult to determine the longitudinal extent of this jet. However, it can be estimated that the supersonic expansion creates a region of constant pressure (*zone of silence*) of approximately 4 mm length [95]. It is estimated that the total XUV transmission through this 4 mm thick region of argon gas at around 150 mbar is less than 0.2% in the wavelength range between $32-40$ nm, indicating that a measured flux of 10^8 photons per second per harmonic corresponds to a generated flux of $> 5 \times 10^{10}$ photons per second per harmonic at the harmonic source and conversion efficiency in the order of 1×10^{-6}. It should be noted that the much larger flux generated in NC-PCF type II compared to the case of IDC-QPM in fibre type I has to be put in perspective. The approximately five times larger mode area of NC-PCF type II compared to type I leads to a larger HHG source size and hence to a larger XUV yield.

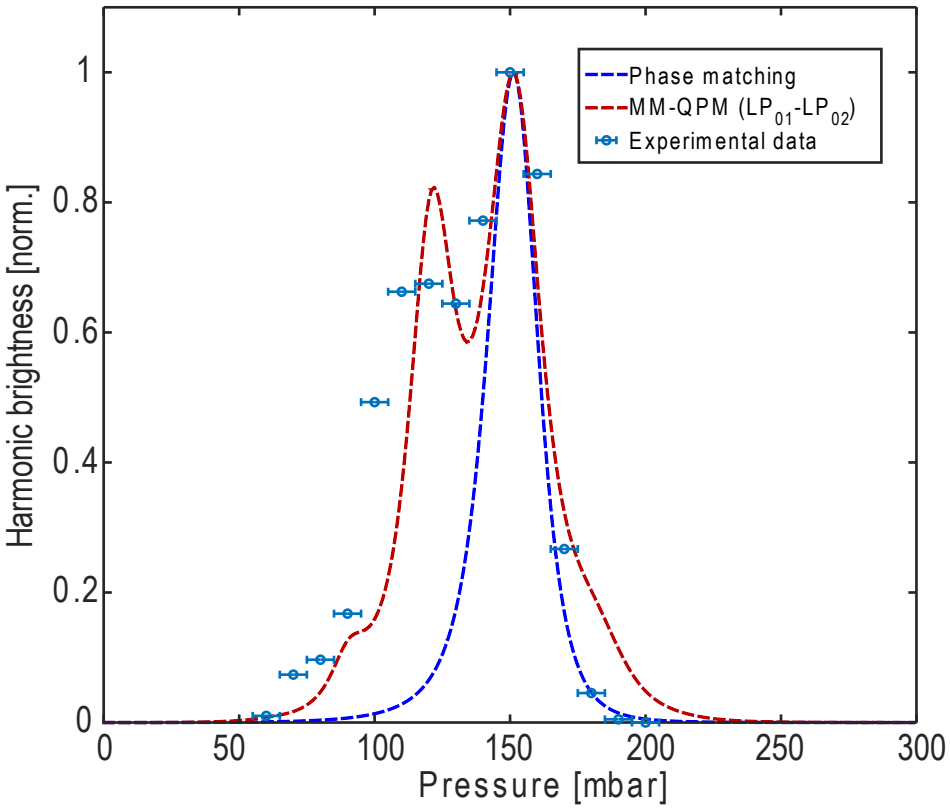


Figure 4.9: **Measured brightness of H21-25 for different gas pressures**. The NC-PCF was filled with Argon at different pressures $P_0 = P_L$. Phasematching is expected to occur at a pressure of $P_0 = 150\,\text{mbar}$ (blue curve). IDC-QPM of the modes LP_{01} and LP_{02} is expected at approximately $P_0 = 120\,\text{mbar}$ (red line).

Chapter 5

IDC-QPM with orthogonal polarization

5.1 Concept

5.1.1 Background

In the experiment described in the previous chapter, it was demonstrated that IDC-QPM is capable of significantly increasing the HHG conversion efficiency in NC-PCF. As a multi-mode QPM technique, IDC-QPM relies on coupling control pulses into multiple waveguide modes and overlapping one higher order mode with the strong fundamental mode of the diver pulse. The resulting mode beating causes longitudinal intensity modulation of the driver beam and suppression of HHG in regions with an intensity minimum. This results in quasi-phase-matching when beat length and coherence length match. The longitudinal modulation depth of the driver depends on the relative amplitude between control pulse and drive pulse modes. In order to maximize the efficiency, the modulation depth of the driver beam has to be maximized. This is challenging in many cases, since the amplitude of the control pulse propagating in a higher order mode is significantly

smaller than the amplitude of the drive beam propagating in the fundamental mode. One possible solution is to maximize the coupling of laser power into higher order modes by using a spatial light modulator [94] or by changing the coupling parameters (cf. section 2.3.1). However, in many cases the intensity modulation is limited to a few percent.

Liu et al. [89] proposed a different method. They suggested that, instead of longitudinal modulation of the HHG source term by modulating the driver intensity, this could be achieved by modulating the ellipticity of the driver. The HHG efficiency drops dramatically with increasing ellipticity of the driver pulse. In practice, this can be realized by coupling into multiple waveguide modes, drive and control pulses with different polarization. Modal dispersion then causes polarization beating, i.e. the driver pulse polarization varies from linear polarization to circular polarization, strongly suppressing HHG at positions where the drive pulse exhibits ellipticity. The proposed technique is called polarization-beating multi-mode QPM (PBMMQPM).

High-harmonic generation is highly susceptible to the driver pulse ellipticity. This can be explained by the lowered recombination probability of the tunnel-ionized electrons during the three step process (cf. section 3.1.1). The strong dependence of HHG to driver pulse ellipticity has been studied in the past and has been successfully applied to the generation of isolated attosecond pulses by using *polarization gating* [96]. In this technique, two circularly polarized pulses with clockwise and anti-clockwise rotation are partially overlapped in time. The superposition of the electric fields results in a composite pulse which exhibits linear polarization in the temporal overlap region of the two pulses and circular polarization everywhere else. When employed to drive HHG, harmonics are only generated in the temporal overlap region where the driver is linearly polarized. This overlap can be minimized allowing for only a single burst of harmonic radiation to be emitted. The reverse principle can be applied to PBMMQPM where harmonic

generation is suppressed in regions where mode beating of two linearly polarized modes leads to the generation of circularly polarized light. Compared to pure intensity modulation, where the harmonics source term $S_q(z)$ scales approximately with $I^5(z)$ (cf. section 3.2.2), the modulation of the source term by polarization beating is more efficient. Studies have shown that, for harmonics orders $q < 31$, the photon yield of HHG scales as [89, 97]:

$$h(\varepsilon) \approx \left(\frac{1+\varepsilon^2}{1-\varepsilon^2}\right)^{q-1} \tag{5.1}$$

where ε is the ellipticity of the driver beam and q is the harmonic order. Equation (5.1) shows that for slight ellipticity of the driver beam, HHG is strongly suppressed. The strong dependence of the HHG efficiency on the ellipticity of the driver results in stronger modulation of the HHG source term $S_q(z)$ than for intensity modulation of the driver beam (cf. section 3.2.2).

5.1.2 HHG build-up

In a waveguide where multiple, radial symmetric modes are excited, the electric field may be written in cylindrical coordinates and in the most general form as:

$$\vec{E}(r,z) = \sum_n E_0 c_n \vec{E}_n(r) \exp\{i[(\beta_n + i\alpha_n)z - \omega t]\} \tag{5.2}$$

where the z-axis is defined as the longitudinal axis of the waveguide, E_0 is the electric field amplitude, c_n, $\vec{E}_n(r)$, β_n, and α_n are the coupling constant, normalized transverse electric field, the propagation constant, and the attenuation constant of the the n^{th} waveguide mode. With IDC-QPM, it is possible to use isolate pairs of waveguide modes for MM-QPM. In the following, the case of two excited, radial symmetric modes is considered. The electric field of the superposition may then

be written as [89]:

$$\vec{E}(r,z) = E_0\{c_1\vec{E}_1(r)\exp\{i[(\beta_1+i\alpha_1)z-\omega t]+c_2\vec{E}_2(r)\exp\{i[(\beta_2+i\alpha_2)z-\omega t]\} \quad (5.3)$$

Further, it is considered that the polarization of the mode is parallel to the x-axis in case of $n = 1$, and forms and angle Ω with the x-axis in case of mode $n = 2$:

$$\vec{E}_1(r) = \begin{pmatrix} E_x \\ E_y \end{pmatrix} = \begin{pmatrix} c_1E_1(r) \\ 0 \end{pmatrix}, \vec{E}_2(r) = \begin{pmatrix} c_2E_2(r)\cos(\Omega) \\ c_2E_2(r)\sin(\Omega) \end{pmatrix} \quad (5.4)$$

Since the two modes propagate with different propagation constants, the electric field components at time $t' = t + \Delta t$, where $\Delta t = -\beta_1/\omega z$ is:

$$\vec{E}(r,z) = \begin{pmatrix} c_1E_1(r)\cos(\omega t') \\ 0 \end{pmatrix} + \begin{pmatrix} c_2E_2(r)\cos(\Omega)\cos(\omega t' + \Delta\beta z) \\ c_2E_2(r)\sin(\Omega)\cos(\omega t' + \Delta\beta z) \end{pmatrix} \quad (5.5)$$

where the mode attenuation has been neglected. In waveguides which are not birefringent, the propagation constants $\beta_{1,2}$ are as defined in 2.3.1.

For HHG, the on-axis electric field $\vec{E}(0,z)$ is most relevant as discussed in section 3.2.2 and the instantaneous on-axis ellipticity of the driver field is defined as [98]:

$$\varepsilon(t) = \tan\left(\frac{1}{2}\arcsin\left(\frac{2E_x(t)E_y(t)\sin(\phi_x(t)-\phi_y(t))}{|E_x(t)|^2+|E_y(t)|^2}\right)\right) \quad (5.6)$$

where $\phi_{x,y}(t)$ is the temporal phase of the electric field components. The longitudinal, on-axis ellipticity $\varepsilon(z)$ for the superposition of driver field and control field is then given by [99]:

$$\varepsilon(z) = \sqrt{\frac{\sin^2(\Omega)\cos^2(\phi_{min}-\Delta\beta z)+\cos^2(\Omega)\cos^2(\phi_m in)}{\sin^2(\Omega)\cos^2(\phi_{max}-\Delta\beta z)+\cos^2(\Omega)\cos^2(\phi_m ax)}} \quad (5.7)$$

where $\phi_{min,max} = \omega t_{min,max}$ is the phase of the minimum and maximum electric

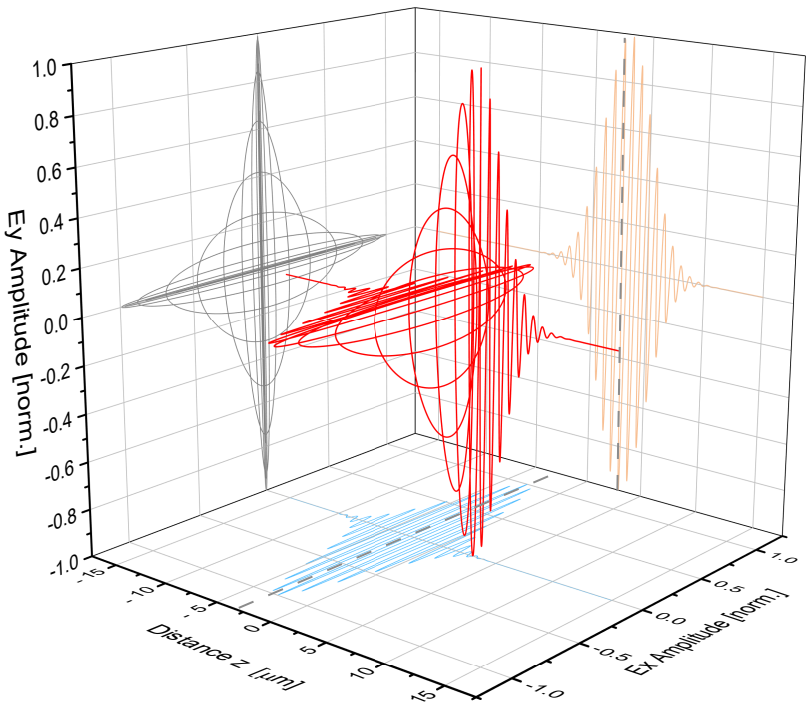


Figure 5.1: **Superposition of two orthogonally polarized laser pulses**. One light pulse is polarized parallel to the x-axis (blue projection onto the xz-plane) while the second, delayed pulse is polarized at $\Omega = 90°$ (orange projection) and exhibits a $\pi/2$ phase shift relative to the first pulse. The delay is indicated by the dashed lines. In the overlap region the electric field exhibits ellipticity which can be seen in the projection onto the yz-plane.

field. The polarization beat length is defined as:

$$L_B = 2L_P = \frac{2\pi}{\Delta\beta} \tag{5.8}$$

It should be noted, that the polarization beat length and the intensity beat length L_B (cf. equation (3.36)) are identical. However, the ellipticity of the driver changes periodically over a distance of $L_P = L_B/2$. This is illustrated in Fig. 5.2. As the two field components E_x and E_y propagate with different propagation constants, the resulting field reaches maximum ellipticity at positions where the two field components are out of phase by odd multiples of $\pi/2$. The handedness of the ellipticity changes with L_P. It should be noted that the harmonic light is not

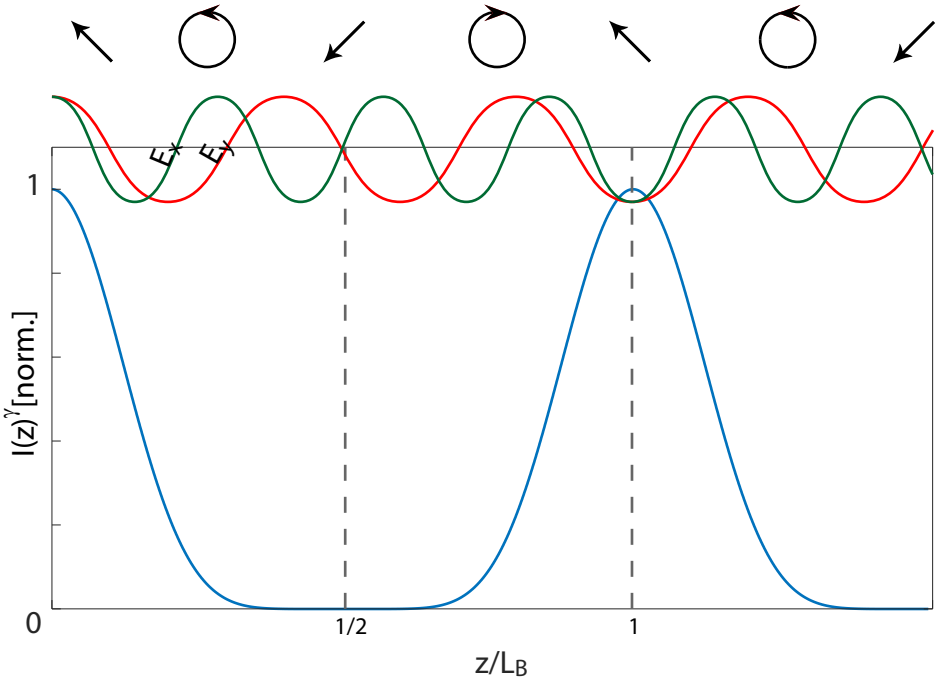


Figure 5.2: **Polarization beating.** Intensity modulation due to mode beating in case the light propagating in two beating waveguide modes has the same polarization (blue graph). For orthogonally polarized pulses, no intensity beating is expected. Instead, the polarization of the electric field varies between elliptic and linear with the beating period $L_B/2$.

guided and thus x and y-components of the harmonic field propagate with the same velocity. However, since the driver propagates in different modes with different propagation constants, the coherence lengths of x and y-components of the harmonic radiation differ. As a result, only one polarization component of the harmonic field can be quasi-phase-matched at a time.

The on-axis modulation of the driver pulse intensity by the control pulse depends on the relative polarization and can be written as [89]:

$$I(z) = c_1^2 E_1^2 + c_2^2 E_2^2 + 2c_1 E_1 c_2 E_2 \cos(\Omega) \cos(\Delta\beta z) \tag{5.9}$$

It can be seen, that IDC-QPM with orthogonally polarized pulses (XIDC-QPM, $\Omega = 90°$) results in polarization beating only. The modulation of the HHG source

term $S_q(z) \propto I(z)H[\varepsilon(z)]$ is then governed by the ellipticity of the driver [89, 99]. For qualitative modelling, it can be assumed that $S[\varepsilon(z)] \propto H[\varepsilon(z)] = \sqrt{h[\varepsilon(z)]}$ ranges over $[0, 1]$. Furthermore, it can be assumed under the same argument as set out in section 3.2.2, that with XIDC-QPM, HHG is generated only in the strongly excited fundamental mode of the driver pulse and that the parts of the control pulse propagating in a higher order mode only act as a small perturbation modulating the driver field ellipticity. The harmonic source term can then be written as:

$$S_q(z) \propto \sqrt{\left(\frac{1+\varepsilon^2}{1-\varepsilon^2}\right)^{q-1}} \tag{5.10}$$

and build-up equation (3.41) can be solved numerically.

5.1.3 Method

For the demonstration of XIDC-QPM, the setup used to demonstrate IDC-QPM (cf. section 4.1.2) was modified by inserting a half-wave plate into the beam path of the delay line while a ND filter was mounted into the second beam path to balance the delay and the optical power in both beam paths. The experimental setup can be seen in Fig. 5.3. The half-wave plate in the delay line rotates the polarization of the laser pulses. The relative polarization angle between drive and control pulse can be changed by rotating the waveplate. For the demonstration of XIDC-QPM the polarization angle was set to $\Omega = 90°$. A 21 mm long section of NC-PCF of type I ($d = 22.5\,\mu\text{m}$) was mounted in between the first and the second vacuum chamber (cf. Fig. 4.2), the first of which was filled with argon at a pressure of $P_0 = 800\,\text{mbar}$ while vacuum was maintained in the second chamber ($P_L = 1 \times 10^{-3}\,\text{mbar}$).

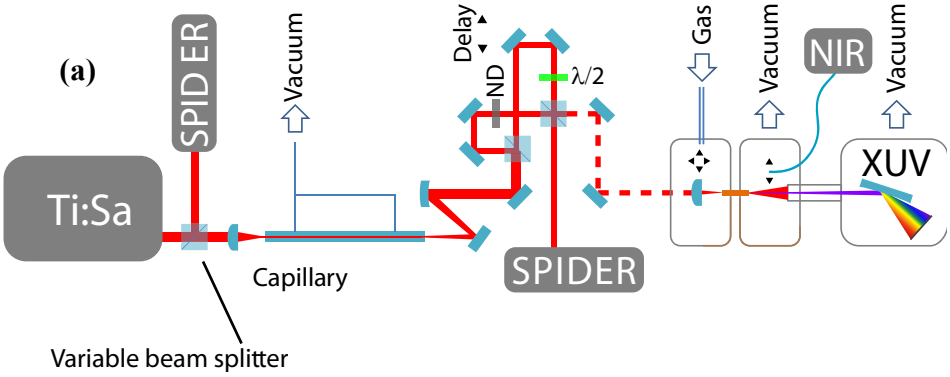


Figure 5.3: **Experimental setup for demonstration of XIDC-QPM**. The experimental setup described in section 4.1.2 was modified. A half-wave plate was inserted into the delay line.

5.2 Results

Cross-polarization IDC-QPM was achieved by coupling into the NC-PCF drive and control pulse with an adjustable delay τ. The pulse energy of drive and control pulse was set to 6 µJ. While scanning τ, the photon yield in harmonics H23-H29 was measured. The results of the delay scan are presented in Fig. 5.4 for the case of XIDC-QPM (control pulse polarization rotated to $\Omega = 90°$) and IDC-QPM ($\Omega = 0°$). Figure 5.4a shows the intensity of H23-H29 for normal IDC-QPM. It can be seen, that enhancement of the HHG efficiency is found for the delay τ corresponding to the overlap of the fundamental LP_{01} mode with some higher order LP_{1n}, LP_{3n} modes (dashed lines). At a delay $\tau = 0$ fs, the fundamental modes of drive and control pulse overlap at $z = L$ causing a coherent superposition. The intensity of H23-H29 resembles a high-order interferometric autocorrelation of drive and control pulse.

Figure 5.4b shows the intensity of H23-H29 for XIDC-QPM. For sake of clarity, the group delays between various modes and the fundamental mode are marked with dashed lines for negative delays only. By comparing a) and b) it can be clearly seen that the enhancement of HHG is observed for different combinations of waveguide modes. This can be explained by the different modulation period

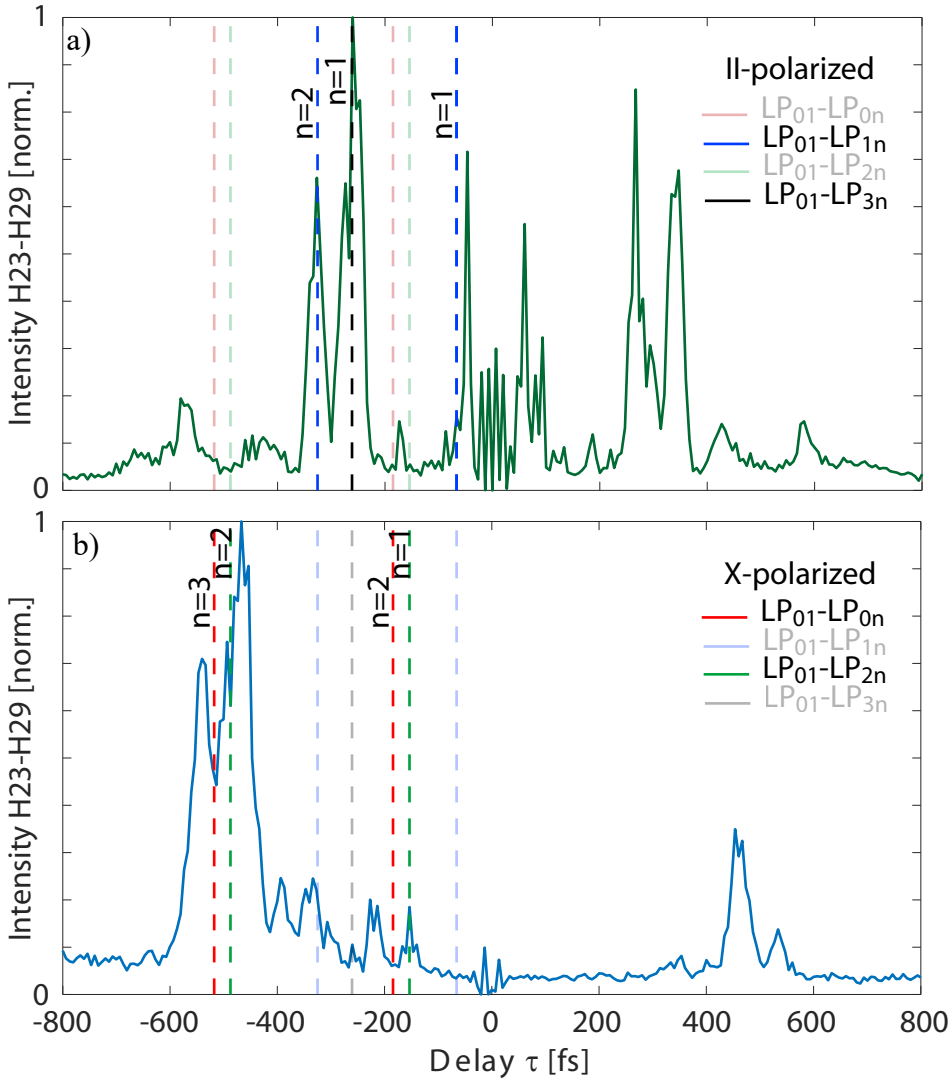


Figure 5.4: **Cross-polarization Intermodal-delay-controlled QPM**. a) Delay scan similar to Fig. 4.5c. The delay τ between control and drive pulse ($\Omega = 0°$) was scanned while the intensity of H23-H29 was measured. b) Results of the same scan performed with $\Omega = 90°$. The normalization factor for a) and b) are approximately the same.

of the HHG source term for the case of $\Omega = 0°$ and $\Omega = 90°$ which differs by a factor of two. In case the intensity beat length L_B for one combination of modes matches a given L_{QPM}, polarization beating of the same mode pair will result in ellipticity modulation with the period $L_P = 1/2L_B$. Since QPM requires the HHG source term to be modulated with $L_{QPM} = jL_B$ (cf. equation (3.35)), where j is an odd integer, $L_B = 2L_P$ implies that one combination of modes cannot lead to

QPM enhancement for both cases, $\Omega = 0°$ and $\Omega = 90°$. The effect of polarization beating is most evident in Fig. 5.4b at a delay of $\tau = 0\,\text{fs}$ where the HHG yield is significantly reduced. This is expected, since the coherent superposition of the two orthogonally polarized fundamental modes of control and drive pulse at $\tau = 0\,\text{fs}$ does not increase the driver pulse intensity, in contrast to the case of parallel polarized modes. Additionally, HHG is suppressed when the delay corresponds to an odd multiple of $\tau = \pi/2\omega$ due to the strong ellipticity of the drive beam. It should be noted that, while the relative intensity of drive and control pulse in a) was almost identical, the intensity changed slightly in b) resulting in the asymmetry of the peaks left and right of $\tau = 0\,\text{fs}$. An alternative explanation for the asymmetry could be a slight drop in output power of the driving laser over the duration of the delay-scan (15 min), also explaining the slightly lower harmonic "background" on the right side compared to the left.

The experimental results are in good qualitative agreement with theoretical predictions of the harmonic brightness enhancement due to XIDC-QPM. Figure 5.5 shows the simulated harmonic build-up in a window around H27 at the output of the NC-PCF section. The simulation predicts enhancement of the HHG efficiency for polarization beating of fundamental LP_{01} mode of the drive pulse with the LP_{03} and the LP_{22} modes of the control pulse (red and green curves). In contrast, no enhancement of the HHG brightness is expected for polarization beating of the fundamental mode of the driver with LP_{1n} modes of the control pulse (blue curves).

It could be argued that the enhancement found in case of IDC-QPM ($\Omega = 0°$) is purely the result of an increased driver intensity when the modes of control and drive pulse overlap in time. However, the enhancement found with XIDC-QPM clearly shows that the increased HHG flux found previously with regular IDC-QPM (cf. chapter 4) cannot simply be the result of an increased intensity, since the driver intensity is not changed by the orthogonally polarized control pulse

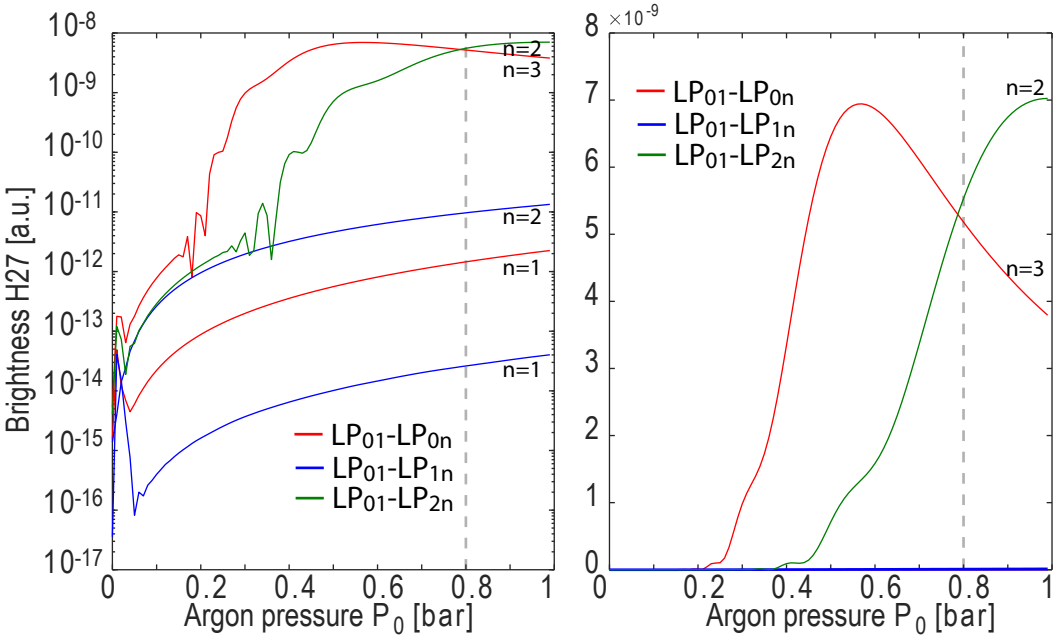


Figure 5.5: **Simulation results for XIDC-QPM**. Enhancement of H27 is predicted for polarization beating of fundamental LP_{01} mode of the drive pulse with the LP_{03} and the LP_{22} modes of the control pulse. The argon pressure used in experiment is marked with a vertical, dashed line. The right panel shows the same data as on the left on a linear scale.

mode. This further supports the hypothesis that the observed enhancement is in fact the result of MM-QPM.

5.2.1 Enhancement

The enhancement due to XIDC-QPM was measured for the delay corresponding to the overlap of the LP_{01} mode of the driver with the LP_{13} mode or the control pulse at $\tau = -500\,\mathrm{fs}$. This corresponds to the enhancement peak in Fig. 5.4b. Figure 5.6 shows the observed harmonic spectrum when HHG was driven with an orthogonally polarized pair of 6 µJ pulses (blue curve). The spectrum observed with single 12 µJ pulses without XIDC-QPM is shown in orange. The peaks of the harmonic spectrum without XIDC-QPM are slightly blue-shifted compared to the harmonic spectrum with XIDC-QPM. This is due to a larger plasma blue-shift of the driver as a result of the higher pump pulse energy used in the single-pulse

case. The two spectra show a strong enhancement of the HHG flux in H25-H29 due to XIDC-QPM. Enhancement by a factor of 70 was observed for H25 and by a factor of 130 for H29. The strongest enhancement by a factor of 160 was found for H27.

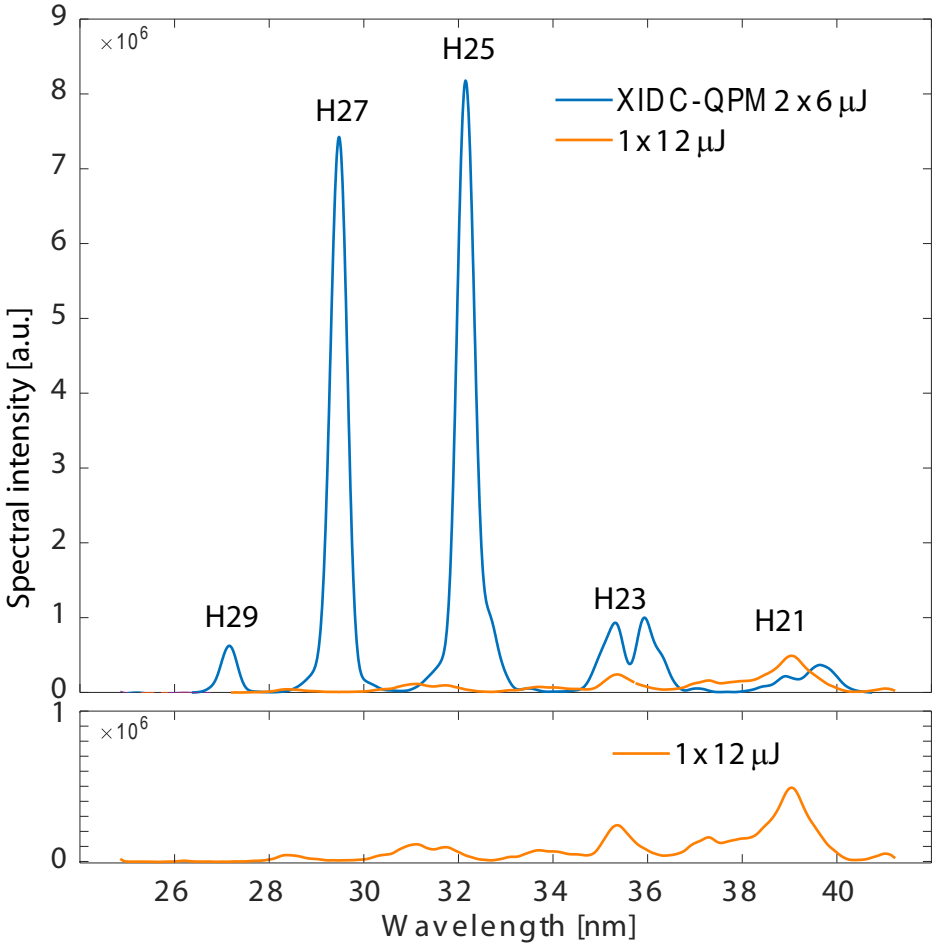


Figure 5.6: **Enhancement of the HHG flux due to XIDC-QPM**. Experimental harmonic spectrum H21–H29 driven with pairs of 6 µJ pulses (delay $\tau = -500$ fs) with XIDC-QPM (blue curve) and driven with single 12 µJ pulses without any QPM (orange curve); the bottom panel shows the same single-pulse data but rescaled. The brightness enhancement of H25-H29 by a factor of up to 160 is the result of XIDC-QPM. The plasma blue-shift of the driver is larger for the higher pulse energy used in the single-pulse case (orange) resulting in a blue-shift of the harmonic peaks compared to the spectrum with XIDC-QPM (blue).

5.3 Conclusion

In chapters 4 and 5, HHG driven with $5-50\,\mu J$, 30 fs laser pulses in the NIR was explored in different types of PCFs, filled with neon or argon gas.

Using Ne and drive pulse energies of $15\,\mu J$, non-phase-matched HHG up to photon energies approaching the aluminium L-edge (72.8 eV) was demonstrated. While using an argon-fill, a novel MM-QPM concept was applied: The group delay between different modes of a PCF ($d = 22.5\,\mu m$) was used to make MM-QPM controllable using pairs of parallel or orthogonally polarized drive and control pulses. Using (X)IDC-QPM, it was possible to increase the efficiency of HHG driven with $5-6\,\mu J$ driving pulses by two orders of magnitude. Furthermore, fully phase-matched HHG in an argon-filled PCF ($d = 53\,\mu m$) was demonstrated using a drive pulse energy of $30-50\,\mu J$. Compared to the QPM case, a higher conversion efficiency could be reached. However, strong reabsorption of the generated XUV photons in the argon gas surrounding the exit of the PCF lead to an overall lower effective conversion efficiency compared to the QPM case.

Chapter 6

Metrology of ultrashort pulses

In the previous chapters, experiments were described which employed ultrashort pulses of light to drive a nonlinear optical interaction. In this and other types of optical experiments, it is vital to characterize the input and output pulses of light in order to study the interaction and determine the experimental conditions. Various parameters are essential for characterizing light pulses such as pulse energy, pulse peak power, spatial and temporal shape or the relative CEP (cf. section 2.1.1). The wide range of pulsed light sources, capable of generating pulses with different duration from CW to the femtosecond or even attosecond regime, requires different characterization techniques. Whereas CW laser beams can often be characterized using slow photoelectric detectors, such as photodiodes or thermoelectric detectors, the long photoelectric response time does not allow this method to be used with femtosecond or even picosecond laser pulses. New types of fast metal-semiconductor-metal photodetectors with ultra low capacitance and active area of only a few microns exhibit impulse responses below ten picoseconds and can be operated with very high reverse bias voltages. Of course, visualizing the output of such photodetectors requires recording devices with sufficient bandwidth and sampling rates. Another technique to measure the temporal shape of light pulses with durations above a few picoseconds are streak cameras. These are based on

the principle of projecting elapsed time onto a spatial axis of a detector by using a high-speed sweep. These devices can reach temporal resolutions of a few hundereds of femtoseconds.

All the characterization techniques mentioned above are limited to light pulses in the range of picoseconds and above. In order to characterize ultrafast laser pulses of only a few tens of femtoseconds which are regularly generated in Ti:Sapphire laser systems, different characterization techniques are required. Starting from optical correlation, a variety of different all-optical pulse characterization techniques for ultrashort pulses such as frequency-resolved optical gating (FROG), spectral-phase interferometry for direct electric field-reconstruction (SPIDER) or Mutual interferometric characterization of two electric fields (MICE) have been developed in the past decades. In this chapter these methods are briefly reviewed.

6.1 Optical Correlation

6.1.1 Intensity autocorrelation

The first attempts to measure the duration of ultrashort pulses were correlation techniques. The general idea of optical correlations is based on the mathematical concept of correlation functions. Given two time-dependent functions $A(t)$ and $B(t)$ one of which is known, then measurement of the first-order correlation function $G(\tau)$ yields the other function:

$$G(\tau) = \int_{-\infty}^{+\infty} dt B(t) A(t-\tau) \tag{6.1}$$

Unfortunately, on an ultrafast timescale, a known test function $A(t)$ (i.e. a reference pulse) cannot be synthesized. However, the pulse itself can serve as a test function. This approach is known as *autocorrelation*. In practice, this is achieved by splitting a pulse under test into two identical replicas using a beam splitter;

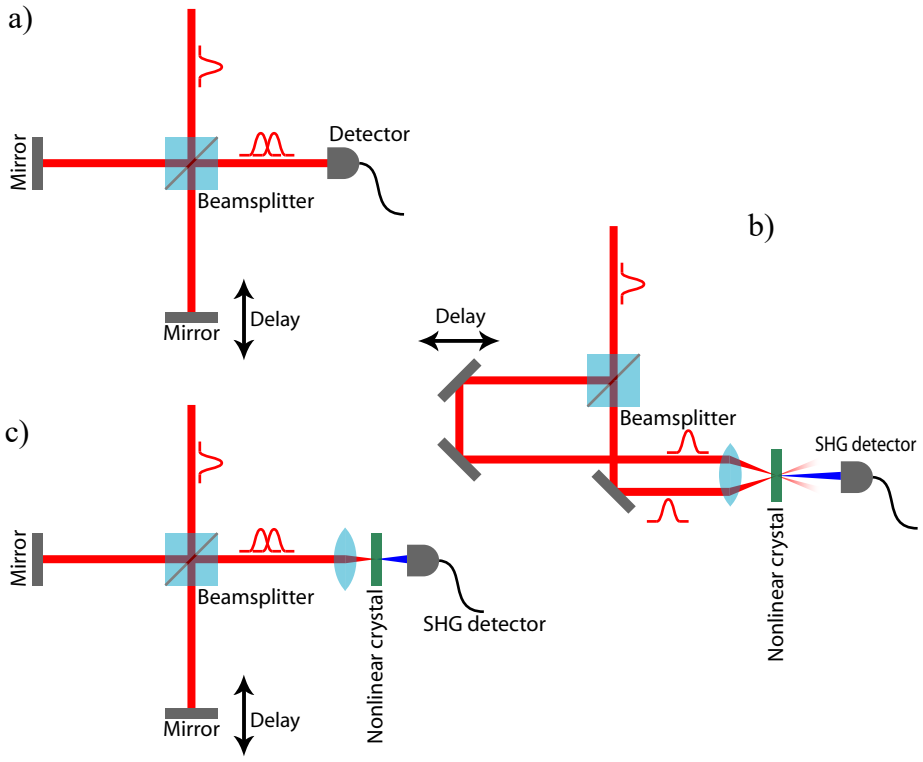


Figure 6.1: **Experimental setups for optical autocorrelation**. a) First-order field autocorrelator. b) Intensity autocorrelator. c) Interferometric autocorrelation (FRAC) setup.

the two pulses are recombined in an interferometric setup where the relative delay τ between the pulses can be varied by changing the length of one interferometer arm. This is shown in Fig. 6.1a. Upon recombining the beam paths, the laser field intensity is measured while scanning τ. The delay dependent intensity $I_1(\tau)$ can be expressed as:

$$I_1(\tau) = \int_{-\infty}^{+\infty} dt \, |E(t) + E(t-\tau)|^2 \tag{6.2}$$

where $E(t)$ is the time dependent electric field. Similar to the first-order autocorrelation function, higher-order correlation functions $I_n(\tau)$ can be obtained. For instance, the second order autocorrelation function can be measured by using a two-photon process such as SHG:

$$I_2(\tau) = \int_{-\infty}^{+\infty} dt \, \left|[E(t) + E(t-\tau)]^2\right|^2 \tag{6.3}$$

Exact knowledge of $E(t)$ requires that all possible autocorrelation functions $I_n(\tau)$ are measured. However, in many experiments it is sufficient to use only intensity autocorrelation while guessing a realistic pulse envelope. The experimental setup for this case can be seen in Fig. 6.1b. In this case, the intensity of the measured second-harmonic signal takes the form:

$$I_2(\tau) = \int_{-\infty}^{+\infty} dt I(t) I(t-\tau) \tag{6.4}$$

The shape of the measured intensity $I_2(\tau)$ is symmetric with respect to $\tau = 0$. The intensity autocorrelation measurement allows only for an estimate of the pulse duration while the actual pulse shape cannot be determined from the shape of the autocorrelation trace [16].

6.1.2 Interferometric autocorrelation

A combination of the techniques described above is the fringe-resolved autocorrelation (FRAC) shown in Fig. 6.1c. In this approach, the interferogram of two frequency doubled pulses I_{FRAC} is measured as a function of delay in a collinear geometry and takes the form of the second-order autocorrelation.

$$I_{FRAC}(\tau) = \int_{-\infty}^{+\infty} dt \left| [E(t) + E(t-\tau)]^2 \right|^2 \tag{6.5}$$

I_{FRAC} is sensitive to the temporal phase of the pulse and may be used to determine the pulse field using an algorithmic approach. Studies by Naganuma and co-workers have shown that, in theory, the pulse field can be fully characterized, except from an ambiguity regarding the dicection of time if, in addition to an FRAC trace, the pulse spectrum is known [100]. However, in practice the algorithm proposed by Naganuma was found to not always converge [16].

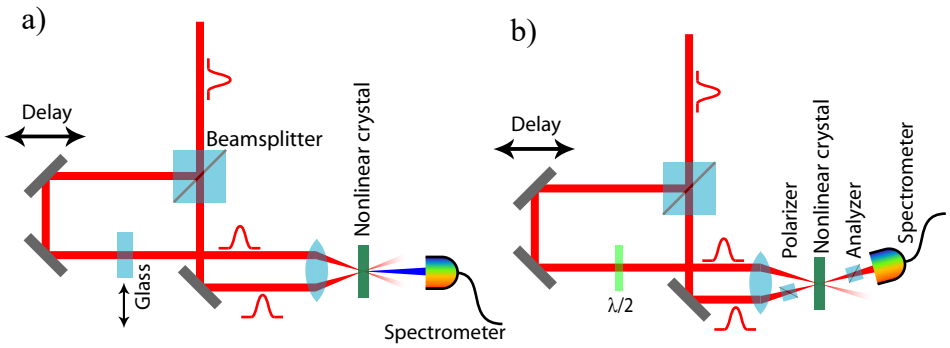


Figure 6.2: **Experimental implementations of FROG**. a) Second-harmonic FROG (SHG FROG). b) Polarization-gated FROG (PG FROG).

6.2 FROG

In the pulse characterization techniques mentioned so far, the temporal shape of the pulse is hidden within the autocorrelation function. The complete temporal characterization of the electric field and phase of an ultrashort pulses of light requires more advanced techniques. One such technique is frequency-resolved optical gating (FROG) which involves spectrally resolving the n^{th} order autocorrelation function. The most common approach is so-called SHG FROG and involves measuring the delay-dependent spectrum of the second harmonic signal. The FROG trace is a spectrogram in the (ω, τ) domain:

$$I_{FROG}^{SHG}(\omega,\tau) = \left| \int_{-\infty}^{+\infty} dt E(t) E(t-\tau) \exp(i\omega t) \right|^2 \tag{6.6}$$

The amplitude and phase of the pulse under test can then be retrieved from the FROG trace using an iterative algorithm. Due to the low-order nonlinearity of the gate, SHG FROG can be applied to the measurement of weak pulses. However, the FROG trace is symmetric with respect to $\tau = 0$ and therefore suffers from the time-direction ambiguity which cannot be resolved without any a priori knowledge of the pulse. A solution to this problem is measuring a second FROG trace for which some positive chirp is introduced in one of the pulses by a piece of glass

inserted into one of the beampaths. This is illustrated in Fig. 6.2a. It is then possible to find a reconstruction of the pulse shape which is unique and consistent with both measurements. Unfortunately, this renders FROG unsuitable for single-shot operation.

Another implementation is polarization-gated FROG (PG FROG), shown in Fig. 6.2b. In PG FROG, a third-order nonlinearity acts as a gate for the test pulse. The test pulse is first split into two pulses, the probe and the gate pulse. The probe pulse is sent through a pair of crossed polarisers while the polarization of the gate pulse is rotated by 45° by using a half-wave plate. Both pulses are then overlapped inside a nonlinear crystal. The gate pulse intensity induces birefringence through the Kerr-effect which shows the same temporal evolution as the gate pulse intensity and rotates the probe pulse polarization by an angle proportional to the instantaneous intensity. Since polariser and analyser are crossed, only polarization-rotated components of the probe pulse are transmitted through the analyser and reach the spectrometer. Hence, it is possible to record the frequency resolved autocorrelation trace of the pulse:

$$I_{FROG}^{PG}(\omega,\tau) = \left| \int_{-\infty}^{+\infty} dt |E(t-\tau)|^2 E(t) \exp(i\omega t) \right|^2 \tag{6.7}$$

Instead of the Kerr-effect, alternative third-order nonlinear effects such as third-harmonic generation can be used to record the FROG trace (6.7) while using a setup similar as shown in Fig. 6.2a [16]. In contrast to SHG FROG, polarization-gated FROG does not suffer from time-direction ambiguity. However, for PG FROG it is necessary to use polarisers with a high extinction ratio which can be costly, and the higher nonlinearity of the gate requires higher test pulse intensities.

In FROG, the spectral phase (cf. section 2.1.1) is reconstructed from a measured FROG trace through an iterative algorithm which aims at solving the 2D phase problem. In physics, the phase problem refers to the loss of phase informa-

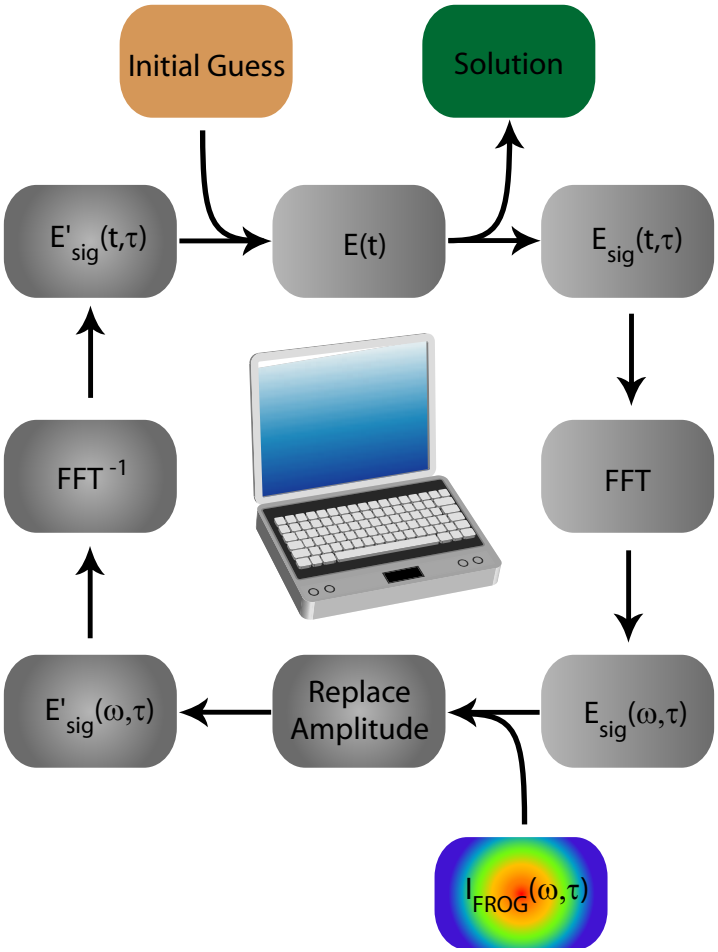


Figure 6.3: **Flowchart of a generic FROG algorithm**.

tion, in case signal intensities are measured instead of signal amplitudes. Common 2D phase retrieval problems can be found in imaging science and signal processing. Over the years, many powerful phase retrieval algorithms have been developed, such as the Gerchberg-Saxton algorithm which is widely used in coherent diffraction imaging. The robustness of these phase retrieval algorithms against measurement noise and stagnation have steadily been improved by employing Fourier filtering and generalised projections, ultimately leading to the development of the principal component generalised projections algorithm (PCGPA) used for FROG. Figure 6.3 shows a flowchart of a generic FROG algorithm. Starting with a random initial guess for the gate and probe pulse amplitude and phase, the algorithm aims at finding two fields which reproduces the measured FROG trace. The first

step involves calculating a $E_{\text{sig}}(t,\tau)$ from the guessed fields. Depending on the type of FROG this signal is given for PG FROG, SHG FROG or THG FROG as:

$$E_{\text{sig}}(t,\tau) \propto \begin{cases} E(t)|E(t-\tau)|^2 \\ E(t)E(t-\tau) \\ E(t)^2E(t-\tau) \end{cases}$$

After a Fourier transform with respect to t, the signal field $E_{\text{sig}}(\omega,\tau)$ is projected onto a set of fields in *Fourier space*, that is consistent with the measured FROG trace. This is most commonly done by simply replacing the amplitudes of the signal field by the square root of the measured intensities $I_{FROG}(\omega,\tau)$. The resulting, updated signal field $E'_{\text{sig}}(\omega,\tau)$ is then Fourier transformed back into the temporal domain and the updated guess $E(t)$ is calculated. The process is then repeated while every cycle yields an improved guess which may converge onto the correct complex electric field of the test pulse, in the ideal case. To date many versions of the FROG algorithm have been developed. Detailed descriptions of various implementations of FROG and different phase retrieval algorithms can be found, for instance in [16].

6.3 SPIDER

A very powerful method for temporal characterization of ultrashort pulses is spectral phase interferometry for direct electric field reconstruction (SPIDER) [101]. This approach makes use of spectral shearing interferometry where the spectral interferogram $I_{SPIDER}(\omega,\tau)$ of two delayed and frequency sheared replicas of the

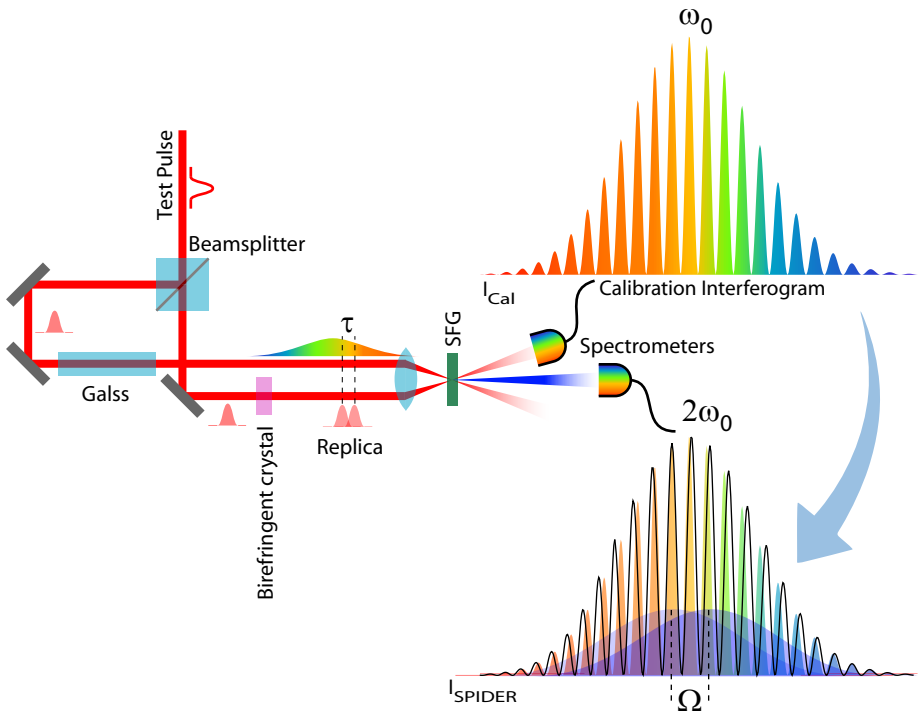


Figure 6.4: **Experimental implementation of SPIDER**. Two replica pulses and one massively chirped ancillary pulse are derived from the test pulse. The pulses are then focussed into a nonlinear crystal where the sum-frequency signal is generated. The SPIDER interferogram and a calibration interferogram are then spectrally resolved and exhibit spectral fringes due to a spectral shear Ω and the delay τ.

test pulse is measured:

$$\begin{aligned} I_{SPIDER}(\omega,\Omega,\tau) &= |E(\omega) + E(\omega-\Omega)\exp(i\omega\tau)|^2 \\ &= I(\omega) + I(\omega-\Omega) + 2\sqrt{I(\omega)I(\omega-\Omega)} \\ &\times \cos\left(\phi(\omega) - \phi(\omega-\Omega) + \omega\tau\right) \end{aligned} \tag{6.8}$$

where Ω is a fixed frequency shear. The τ-dependent term in equation (6.8) is also referred to as the *AC-term* whereas the other part is called the *DC-term*. The spectral phase $\phi(\omega)$ is encoded in the AC-term or the interferrogram and can be extracted directly from the measured data without an iterative phase retrieval algorithm. The concept and an experimental implementation of SPIDER is il-

lustrated in Fig. 6.4. A pair of pulses is generated from a linearly polarized test pulse in a beamsplitter. One pulse, the *ancillary* pulse, is then sent through a pulse stretcher e.g. a thick block of glass which introduces a large frequency chirp through the GDD. The second pulse is sent though an interferometer or a birefringent crystal in order to generate two replica pulses delayed by τ. The replica pulses are then temporally overlapped with the ancillary pulse in a nonlinear crystal where the two replica pulses undergo sum-frequency generation with different frequency components of the ancillary pulse, separated by $\Omega = \tau/GDD$. The replica pulse pair and the sum-frequency signal are then spectrally resolved. Due to the temporal delay, the spectrum of the pair of replica pulses exhibits spectral fringes which are separated by $\delta\omega = 2\pi/\tau$. The spectrum of the sum-frequency signal also exhibits cosine modulation of the spectral intensity as can be seen in equation (6.8) where the modulation is set by:

$$\theta(\omega) = \phi(\omega) - \phi(\omega - \Omega) + \omega\tau \tag{6.9}$$

Comparison of the SPIDER interferogram to the calibration interferogram of the replica pulse pair allows for separating the contributions from the spectral phase and from the delay. This can be done using an algorithm developed by Takeda and co-workers [102]. Figure 6.5 shows a flowchart of the phase extraction algorithm used for SPIDER. The first step in this algorithm involves a Fourier transformation of the measured SPIDER interferogram into the temporal domain. The resulting Fourier transformed SPIDER interferogram consists of a peak at $t = 0$, referred to as the *DC-peak* corresponding to the DC-term in equation (6.8), and two *AC-sidebands* corresponding to the modulation of the spectral intensity. In order to isolate the AC-term which contains the information on $\theta(\omega)$, one AC-sideband is isolated by applying a gate window. In order to remove the contribution of $\omega\tau$ in equation (6.9), the calibration phase is extracted from the calibration in-

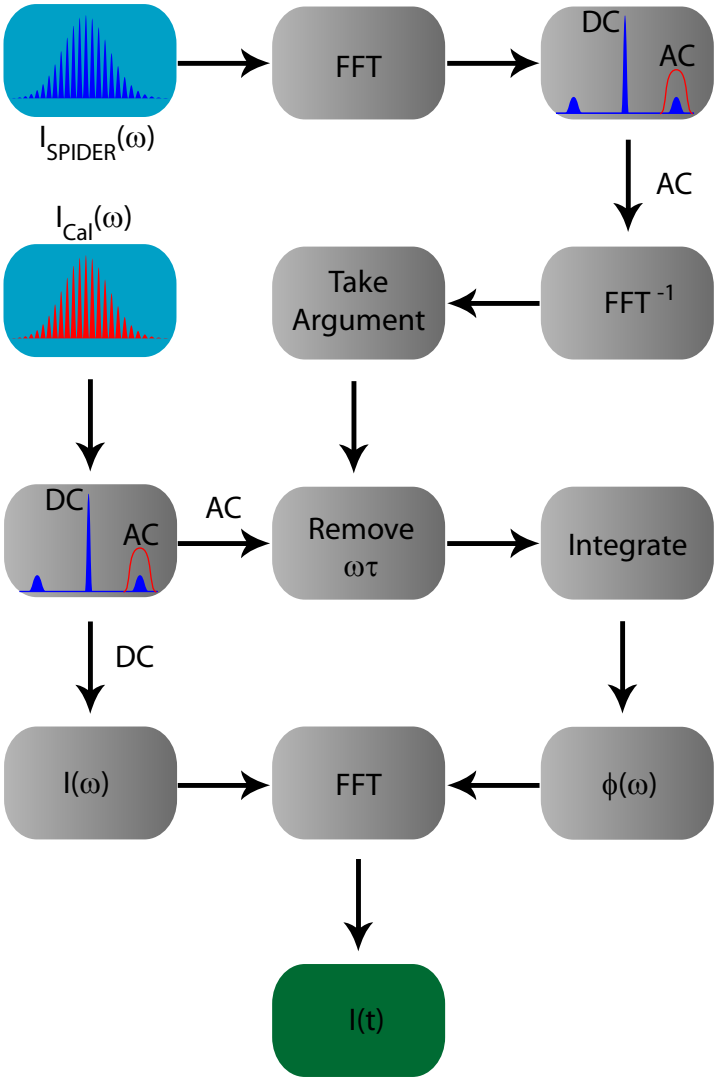


Figure 6.5: **Phase extraction algorithm for SPIDER**.

terferogram using the same filtering method and the AC-sidebands of calibration interferogram and SPIDER interferogram are substracted. The result is then Fourier transformed back into the spectral domain, yielding the phase difference $\phi(\omega) - \phi(\omega - \Omega)$ between sectral components of the test pulse separated by the frequency shear which corresponds to the gradient of the spectral phase for small shears. Finally, concatenation or integration yields the spectral phase of the test pulse.

Figure 6.6 shows the recorded SPIDER and calibration interferogram of an ultrafast, high average power OPCPA laser system operating at a central wave-

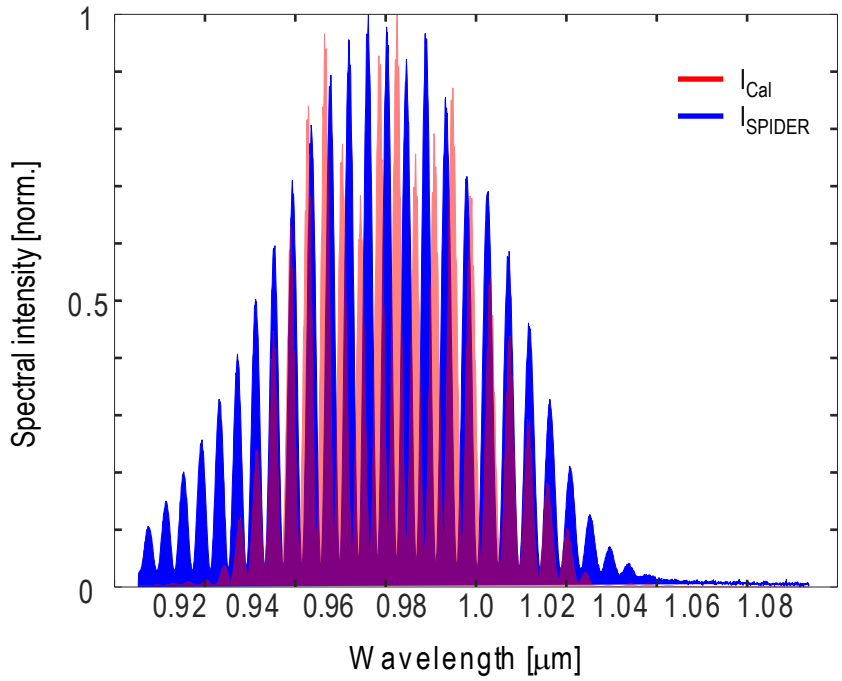


Figure 6.6: **SPIDER and calibration interferogram.**. The spectral phase information is contained in the fringe spacing of the SPIDER interferogram which becomes apparent when comparing the calibration interferogram (red) and the SPIDER interferogram (blue).

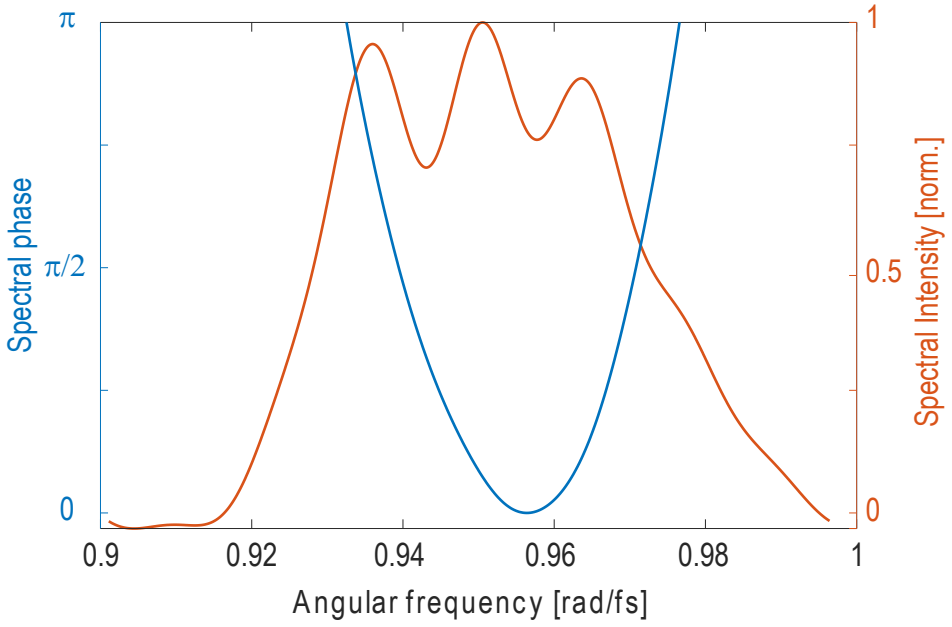


Figure 6.7: **Reconstructed spectral phase** of the output pulses of an OPCPA system operating at a central wavelength of 1.9 µm.

length of 2 µm. Single-shot temporal characterizing of laser pulses at this central wavelength is challenging due to a lack of suitable spectrometer technology for this wavelength range. The experimental setup used to acquire the interferograms was similar to the one shown in Fig. 6.4. A 30 mm thick block of silicon was used instead of glass as a pulse strecher in a double pass geometry to generate the chirped ancillary pulse and a 1.5 mm thick birefringent Tellurium dioxide crystal was used to generate the replica pulses. The SPIDER and calibration signals where recorded at a central wavelength of $\sim$ 1 µm by using the SFG and SHG signal of the pulses generated in a 3 mm thick BBO crystal. The extracted spectral phase is shown in Fig. 6.7 together with the measured spectral intensity. The spectral phase shows that the uncompressed output pulses of the OPCPA were positively chirped.

6.4 Discussion

Interferometric techniques such as SPIDER benefit from the fact that the spectral phase can be determined analytically. This enables single-shot characterization, high resilience to noise, due to Fourier-filtering, and robustness against phase-matching non-uniformity of the nonlinear process. Furthermore, the algorithmic phase extraction process is less computationally involved than an iterative phase retrieval, since instead of 2D spectrograms, only 1D interferograms have to be processed. However, SPIDER is also not free from ambiguities. The absolute phase of the electric field, as well as the absolute arrival time, cannot be determined. Another challenge results from the fact that the spectral phase cannot be recovered, if the spectrum of the test pulse exhibits extended intensity nulls. In particular, if these spectral gaps are wider than the frequency shear, the spectral phase across the gap cannot be characterized. Even though, the spectral phase in regions where the the spectral intensity is non-zero may well be characterized, the relative spectral phase between these regions cannot be determined. In the temporal domain, the relative phase information between different regions in the pulse spectrum has a substantial impact on the temporal pulse shape as will be outlined in the next section. In the past, multiple shears have been used to characterize the phase across a spectral gap. However, the requirement for the pulse to contain a spectral region substantially wider than the gap still remains [103, 104].

6.4.1 Multi-Colour Pulses

Light pulses composed of multiple colours play an important role in generating short light pulses with arbitrary waveforms that have many applications in science and technology. In this context, light-wave synthesis has gained significant interest as it enables control over the optical waveform with sub-cycle precision. These have applications e.g. for the generation of isolated attosecond pulses without the

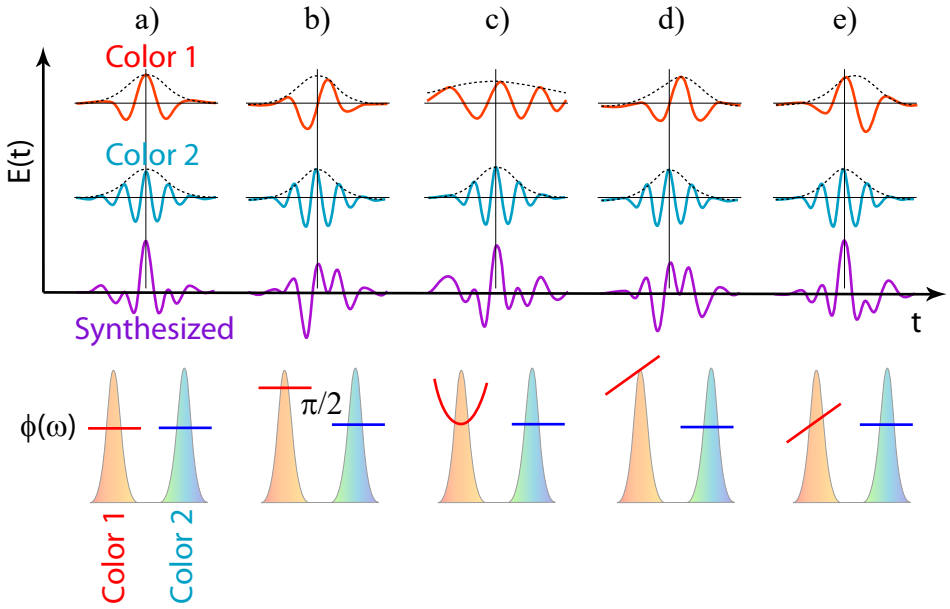


Figure 6.8: **Multi Colour pulses with different relative phases**, adapted from [105].

use of polarization gating or pulse compression.

Based on the concept of wavepackets introduced in section 2.1, lightwave synthesis involves coherently combining separated spectral components with "different colours" (the *parent pulses*) to a hybrid pulse with a defined waveform and temporal duration. A particularly attractive concept is the coherent superposition of separate laser sources operating at different central wavelengths. Synthesizing the shortest possible pulse sets specific requirements on the bandwidth of hybrid spectrum and the spectral phase of the parent pulses. This is illustrated in Fig. 6.8. While the individual parent pulses can have a narrow bandwidth, the spectrum of the synthesized pulse may cover a broad spectral range and therefore supports light pulses shorter than the parent pulses. The hybrid spectrum may exhibit an extended spectral region with vanishing spectral intensity. In the past, characterization techniques such as spatially encoded arrangement of chirped arangement for SPIDER (SEA-CAR-SPIDER) have been developed capable of characterizing pulses with narrow spectral gaps [104]. However, if this spectral gap has an extent

similar or larger than the spectral support of the individual parent pulses, common pulse characterization techniques fail at reconstructing the relative spectral phase across the spectral gap. A spectral gap is considered large, if the gap size is similar or wider than the spectral support of the parent pulses. In literature, this issue has been discussed extensively, for instance by Keusters and co-workers [103]. An overview and a detailed discussion can also be found in [6].

The impact of a variation in the relative spectral phase is illustrated in Fig. 6.8. As can be clearly seen, altering the relative spectral phase of the parent pulses (blue and red) fundamentally changes the waveform of the synthesized pulse (purple). Comparing Fig. 6.8 a) and b) shows that, even though the phase of the parent pulses may be perfectly flat, the relative phase offset between the colours leads to a dramatic change in the synthesized waveform. A technique capable of fully characterizing the spectral phase of such multi-colour pulses is therefore paramount. In the recent years attempts were made to overcome this problem by combining multi-shear interferometry with iterative 2D phase retrieval algorithms, in order to extract the spectral phase from a series of interferograms. This resulted in development of spectral-gap immune characterization of electric fields, the SPICE-approach.

Chapter 7

Characterization of multi-colour pulses

The aim of the experimental work described in this chapter is the demonstration of a pulse characterization technique capable of reconstructing the spectral phase of multi-colour laser pulses which exhibit a spectrum containing a large spectral gap. In the past, attempts were made to characterize such pulses by using SPICE [6]. However, the experimental implementation resulted in an ambiguity which could not be resolved. In this chapter, an experiment is described which aims at demonstrating SPICE without this ambiguity by using an alternative experimental implementation.

7.1 Background

The concept of SPICE is based on the MICE technique [106, 8]. This technique enables simultaneous temporal or spatial characterization of a set of independent, mutually coherent electric fields without the requirement of a well characterized reference field or a priori knowledge. This is done by measuring the fringe-resolved field cross-correlation (FCC) of the test fields and an iterative 2D phase retrieval

algorithm based on Fourier processing of the interferograms and generalized projections.

7.1.1 MICE

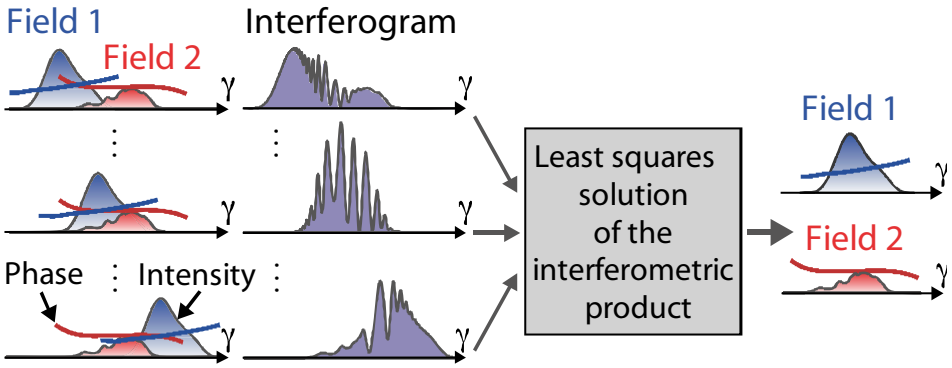


Figure 7.1: **Concept of MICE** taken from [106].

In the MICE approach, one test field $E_1(\gamma)$ is interfered with another, uncharacterised field $E_2(\gamma - \Gamma)$ that has been sheared in a set degree of freedom by the amount Γ. In contrast to SPIDER, the two fields do not have to be replicas. However, it is a requirement that the fields are mutually coherent to a degree that enables resolving the interference of the two superimposed fields. The concept of MICE is illustrated in Fig. 7.1. For reconstruction of the spatial phase, i.e. the wavefront, multiple shears are applied in the spatial domain where the degrees of freedom are x, y, z and t while a spatially resolved interference pattern is recorded for each shear. In turn, in the Fourier domain, the shear is applied in the Fourier-equivalent degrees of freedom, k_x, k_y, k_z and ω. In the absence of space-time coupling, the degrees of freedom can be considered independently and reconstruction of the spectral phase involves applying K frequency shears while recording a series of K interferograms each sampled over J data points. The recorded intensities $I_{j,k}$ are then given by:

$$I_{j,k} = |E_1(\gamma_j)|^2 + |E_2(\gamma_j - \Gamma_k)|^2 + 2\Re[E_1(\gamma_j)E_2^*(\gamma_j - \Gamma_k)] \tag{7.1}$$

The phase information is encoded in the fringe modulations governed by the interferometric product $2\Re[E_1(\gamma_j)E_2^*(\gamma_j - \Gamma_k)]$. Similar as done for SPIDER, MICE involves isolating this AC-term by Fourier filtering. The processed interferograms $AC_{j,j-k}^{meas}$ then form a dataset of size $J \times K$. The MICE algorithm then involves finding two fields which best reproduces $AC_{j,j-k}^{meas}$. This is done iteratively by minimizing the error:

$$\epsilon = \sum_{j,k}^{J,K} \left| AC_{j,j-k}^{meas} - E_1(\gamma_j)E_2^*(\gamma_j - \Gamma_k) \right|^2 \tag{7.2}$$

In the reconstruction, ϵ is used as an error metric which shows convergence of the algorithm. By setting to zero the derivative of equation (7.2) with respect to E, experssions for the fields $E_{1,2}$ can be found:

$$E_1(\gamma_j) = \frac{\sum_k AC_{j,j-k}^{meas} E_2(\gamma_j - \Gamma_k)}{\sum_k |E_2(\gamma_j - \Gamma_k)|^2} \tag{7.3}$$

$$E_2(\gamma_j) = \frac{\sum_k AC_{j,j+k}^{meas} E_1^*(\gamma_j + \Gamma_k)}{\sum_k |E_1(\gamma_k + \Gamma_k|^2} \tag{7.4}$$

This system of equations can be solved iteratively. First, a random guess for E_2 is taken and inserted into equation (7.3) and the field E_1 is calculated using the measured AC-term $AC_{j,j-k}^{meas}$. The field E_2 is then updated by inserting the result into equation (7.4). The process is then repeated until the result is convergent, and the two reconstructed fields minimize the field error ϵ. Usually, the convergence of MICE is very fast, requiring fewer than ten iterations [106]. Similar as in coherent imaging techniques such as ptychography, it is essential that $AC_{j,j-k}^{meas}$ contains redundant information, i.e. that two consecutive interferograms partly overlap. This can be guaranteed by choosing sufficiently small shear steps. Since the phase can only be recovered in the region covered by the applied shears, the implementation must also provide sufficient shear coverage.

As in all the characterization techniques presented in the previous sections, the absolute phase of each field remains ambiguous. Additionally, $AC^{meas}_{j,j-k}$ does not allow for reconstruction of the field intensities. This is due to the fact that $AC^{meas}_{j,j-k}$ contains information on $E_1(\gamma_j)E_2^*(\gamma_j - \Gamma_k) = \alpha E_1(\gamma_j)\frac{1}{\alpha}E_2^*(\gamma_j - \Gamma_k)$, where α is a complex constant or a slowly varying γ-dependent function. However, the reconstructed intensities may closely resemble the real field intensities in most cases. Alternatively, the real spectral intensities can be extracted from the DC-terms of the measured interferograms or can simply be measured for each field separately. One big advantage of MICE is the robustness against noise and low signal levels due to the heterodyne effect and the generalized projections approach. The combined advantages enables the phase to be recovered at extraordinarily low signal to noise ratios (SNRs) where the signal is deeply embedded into a noise floor. This makes MICE also applicable to holographic imaging of weakly scattering samples when a well characterized reference beam is not available e.g. in XUV holography. The noise performance of the MICE algorithm has been studied in the past and MICE has been found to be robust even against extreme noise levels [106, 8]. This can be explained by the fact that MICE routine takes advantage of both, efficient noise suppression by Fourier filtering as well as of least-squares minimization.

7.2 Applications of MICE

The multi-shear approach of MICE is applicable to a broad range of phase characterization problems where other characterization techniques fail. In particular, it enables characterization of the spectral phase of multi-colour light pulses with a spectral gap larger than the spectral support of the parent pulses. For that, the MICE approach can be adapted to spectral shears where ω_j, Ω_k take the roles of γ_j, Γ_k. In order to apply the MICE technique to the spectral domain,

many frequency shears must be applied to the test pulse (TP). A common approach is known from SPIDER and involves using an ancillary pulse (AP) which is heavily chirped. By sum-frequency generation of the test pulse with specific quasi-monochromatic slices of the ancillary pulse, the frequency up-converted test pulse can be spectrally sheared. The chirp may be encoded in time by using a temporal chirp or in space by spatially chirping the ancillary pulse such as done in SEA-CAR-SPIDER. Using a temporally chirped ancillary pulse, the amount of shear can be set by delaying the test pulse relative to the ancillary pulse by an adjustable delay τ.

7.2.1 Application to SEA-CAR-SPIDER

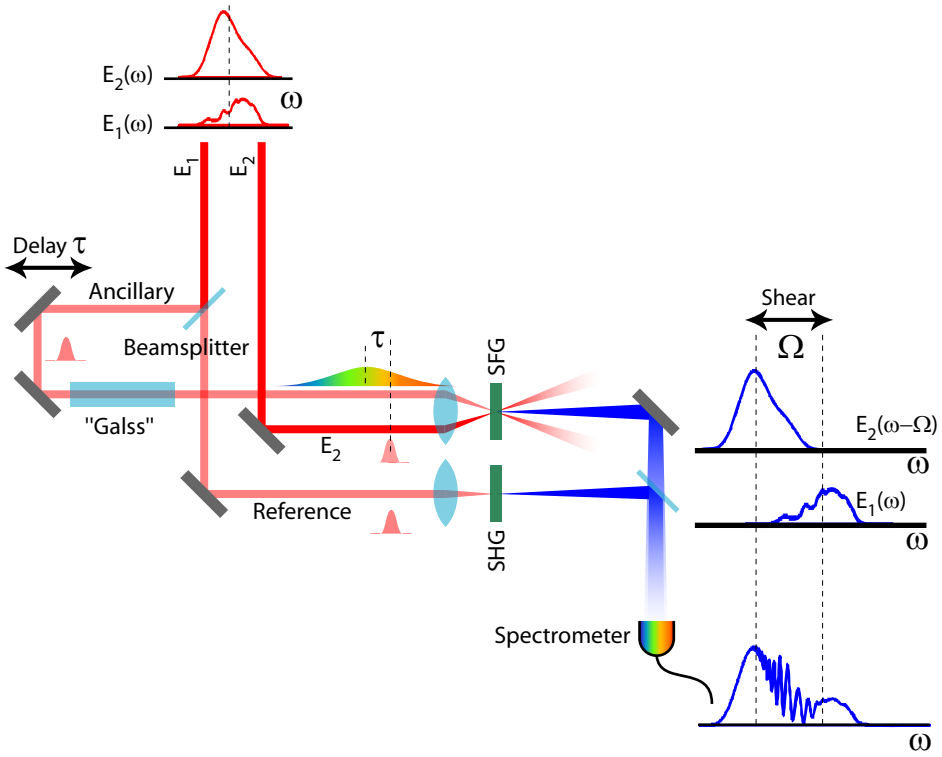


Figure 7.2: **Concept of spectral shearing MICE**. The field E_1 is split into a reference beam and an ancillary beam. A sum-frequency signal is generated from the ancillary field and the field E_2, and subsequently interfered with the frequency-doubled reference field. A series of interferograms is recorded using a spectrometer.

One possible implementation of frequency shearing MICE is illustrated in Fig. 7.2. Two mutually coherent light pulses E_1 and E_2 are sent into the apparatus. One of the field is split into a reference field and an ancillary field by a beamsplitter. The ancillary field is temporally chirped by using a pulse stretcher or a thick block of glass before it is focussed into a nonlinear crystal where it undergoes SFG with the field E_2. By varying the delay τ, the frequency shear can be adjusted. The reference pulse (RP) is frequency doubled in a nonlinear crystal and then interfered with the SFG signal in a collinear geometry. An interferogram is recorded for each shear using a spectrometer. For each shear, the phase difference between the sheared test pulse and up-converted reference pulse is encoded in the spectral fringes.

Instead of using a temporal chirp, the ancillary pulse may also be spatially chirped enabling the use of a spatially resolving imaging spectrometer to record interferograms for multiple shears in a single shot. This approach is used in SEA-CAR-SPIDER where two spatially chirped ancillary pulses are used to shear the test pulse in two directions. The two up-converted, oppositely sheared replicas of the test pulse are interfered on a spatially resolving spectrometer. A typical interferogram of two test pulses $E_{1,2}$ with a fundamental wavelength around 800 nm taken from [106] is shown in Fig. 7.3a. The spatial chirp is applied to the ancillary pulse which results in a position dependent frequency shear of the sum-frequency signal (blue, dashed line). The MICE routine was then applied to the experimental data. As can be seen in Fig. 7.3b, the convergence of the algorithm is fast. The retrieved spectral intensities and spectral phases of the two test fields $E_{1,2}$ are shown in Fig. 7.3c. In order to apply the MICE routine to SEA-CAR-SPIDER data or to any implementation of MICE where a chirped ancillary pulse is used to generate a frequency shear, the MICE routine has to be modified, since in the SFG process, the amplitude and phase of the quasi-monochromatic spatial or temporal slice of the ancillary field contributes to the phase and amplitude of the SFG

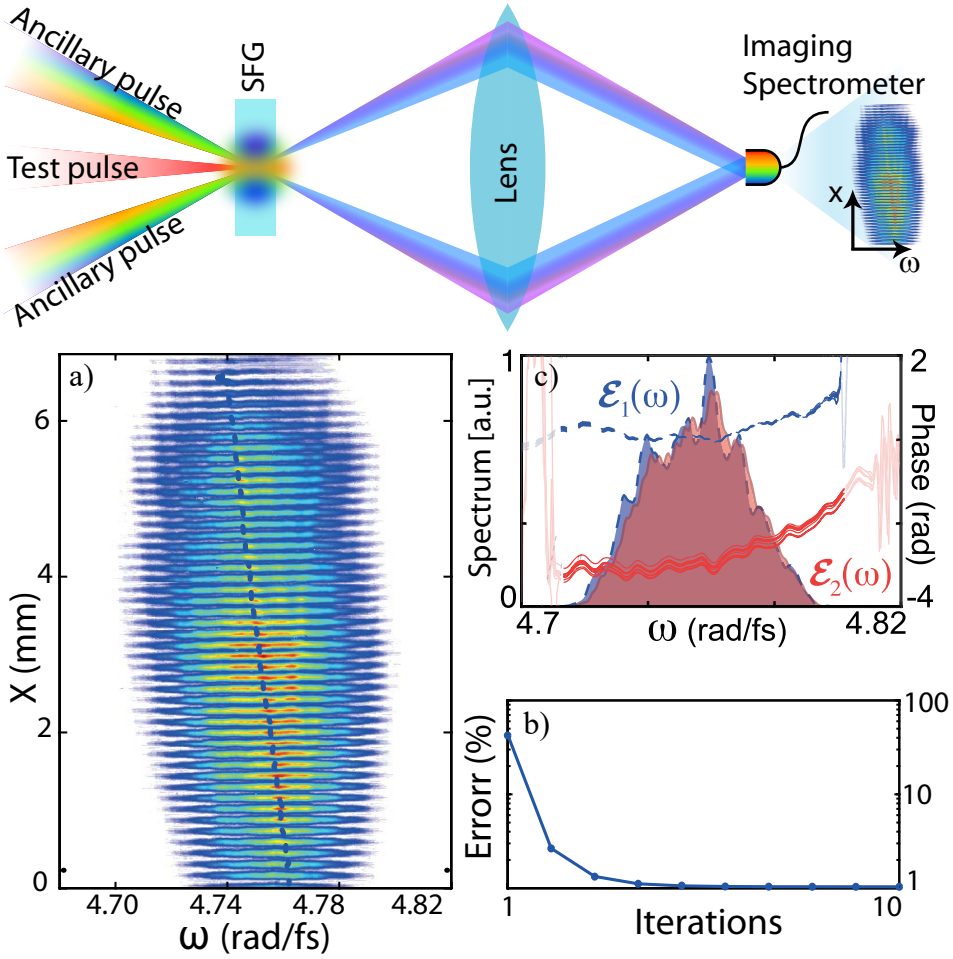


Figure 7.3: **Spectral shearing MICE** adapted from [106]. Top: Experimental concept of SEA-CAR-SPIDER. a) SEA-CAR-SPIDER interferogram of two pulses at a fundamental wavelength of 800 nm; the dashed blue line marks the spectral shear. (b) Reconstruction error. (c) Retrieved spectral phases and intensities of $E_{1,2}$ after ten iterations of the MICE routine (red,blue).

signal. Therefore, the ancillary field takes the role of a third unknown field. Technically, this can be taken into account by multiplying the up-converted field by a complex, Ω-dependent factor $E_{1,2}(\omega-\Omega_{1,2})\alpha_{1,2}(\Omega_{1,2})$. Inserting the modified fields in equation 7.1 changes the interferometric product to $E_1(\omega_j)E_2^*(\omega_j-\Omega_k)A(\Omega_k)$, where $A(\Omega_k)=\alpha_1\alpha_2^*(\Omega_1-\Omega_2)$ [8]. Minimizing the error 7.2 with respect to the updated fields, yields a set of equations for the three unknown fields:

$$E_1(\omega_j)=\frac{\sum_k AC^{meas}_{j,j-k}E_2(\omega_j-\Omega_k)\cdot A^*(\Omega_k)}{\sum_k|E_2(\omega_j-\Omega_k)\cdot A(\Omega_k)|^2} \tag{7.5}$$

$$E_2^*(\omega_j)=\frac{\sum_k AC^{meas}_{j+k,j}E_1^*(\omega_j+\Omega_k)\cdot A^*(\Omega_k)}{\sum_k|E_1(\omega_j)E_2(\omega_j-\Omega_k)|^2} \tag{7.6}$$

$$A(\Omega_k)=\frac{\sum_j AC^{meas}_{j,j-k}\cdot E_1^*(\omega_j)E_2(\omega_j-\Omega_k)}{\sum_j|E_1(\omega_j)E_2(\omega_j-\Omega_k)|^2} \tag{7.7}$$

This set of equations can be solved iteratively using the same MICE routine as outlined above while using initial random guesses for E_2 and A. Further details on the MICE technique can be found in [106, 8, 6].

7.2.2 SPICE

Spectral shearing MICE can be employed to reconstruct the spectral phase across a large spectral gap. Previous experiments used a spatially encoded variant of the experimental implementation shown in Fig. 7.2 (SEA-SPICE). This is depicted in Fig. 7.4. Two unknown fields E_1 and E_2 are sent into the SEA-SPICE setup. A sum-frequency signal is generated from field E_2 and a spatially chirped ancillary field in a nonlinear crystal. The field E_1 is frequency-doubled and interfered with the sum-frequency signal on a spatially resolving spectrometer.

The SEA-SPICE approach is subject to a phase ambiguity resulting from space-time coupling (STC) of the chirped ancillary pulse. In the experimental implementation used in [6], the ancillary field was spatially chirped by using a grating

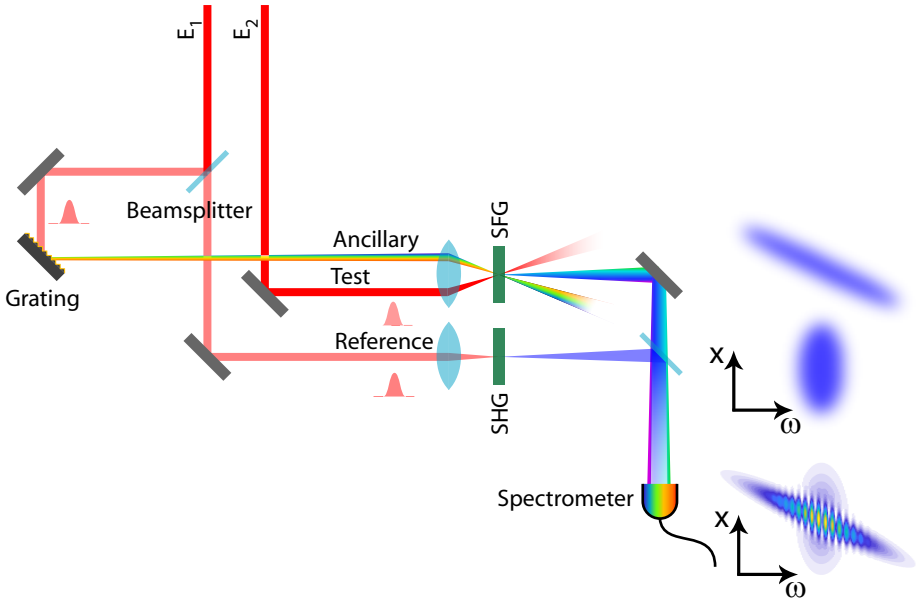


Figure 7.4: **Concept of SEA-SPICE**. The unknown field E_2 undergoes sum-frequency generation with a spatially chirped ancillary field. The field E_1 is frequency-doubled and interfered with the sum-frequency signal on a spatially resolving spectrometer.

which introduced a pulse front tilt (PFT). This is illustrated in Fig. 7.5. The

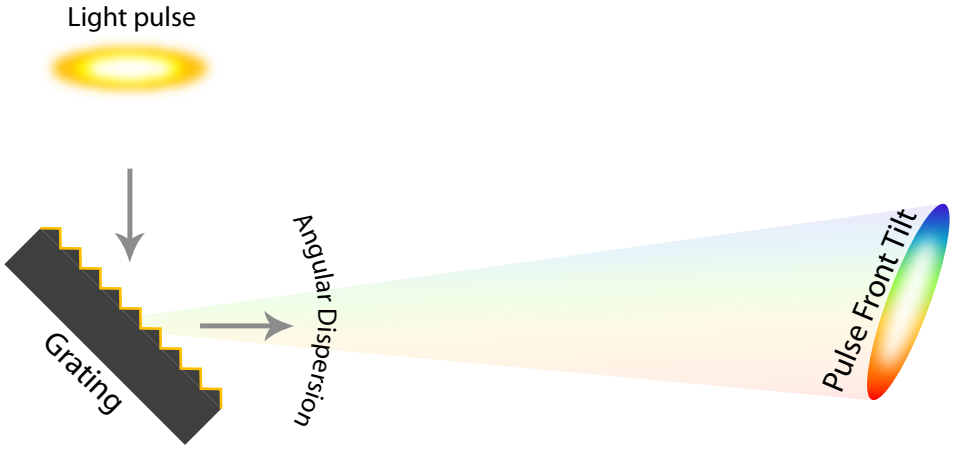


Figure 7.5: **Pulse Front Tilt**. The PFT is one example for space-time coupling (STC) of a light pulse.

PFT manifests as an additional temporal phase of the ancillary field. It can be

characterized as the derivative of the pulse front arrival time t_0 with respect to the position x:

$$\begin{aligned} p &= \frac{dt_0}{dx} \\ &= k_0 \frac{d\theta}{d\omega} + \phi^{(2)} \frac{d\omega}{dx} \end{aligned}$$

where k_0 is the wavenumber, $\phi^{(2)}$ is the second order phase. In SEA-SPICE, the PFT of the ancillary pulse contributes to the phase of the AC-term of the SPICE interferogram:

$$\phi_{AC} = \phi_{E_1}(\omega) - \phi_{E_2}(\omega - \Omega) - \phi_A(\Omega) + \phi_{STC}(\omega, \Omega) \tag{7.8}$$

where the contribution of $\phi_{STC} = \gamma(\omega - \omega_0)(\Omega - \Omega_0) = \gamma\omega\Omega - \gamma\omega_0\Omega$ with the coupling term $\gamma\omega\Omega$ which has the same effect to the fringe spacing as an additional quadratic phase added to the real phase of the interfering fields. In the MICE reconstruction, ϕ_{STC} cannot be separated from the actual GDD of the fields. Calibrating the SPICE apparatus for this ambiguity is difficult and requires elaborate optimization of the shear resolution in order to isolate the contribution of ϕ_{STC} from the real phase of the fields [6].

This issue can be resolved, to the expense of the single-shot capability, by choosing the implementation of SPICE which does not rely on a spatially chirped ancillary pulse.

7.3 Experimental Method

In the experiment described in this chapter, a the SPICE concept illustrated in Fig. 7.2 was used. A beam of 100 µJ, 30 fs pulses from Ti:Saphire laser was sent into the experimental setup depicted in Fig. 7.6. The size of the input beam (red

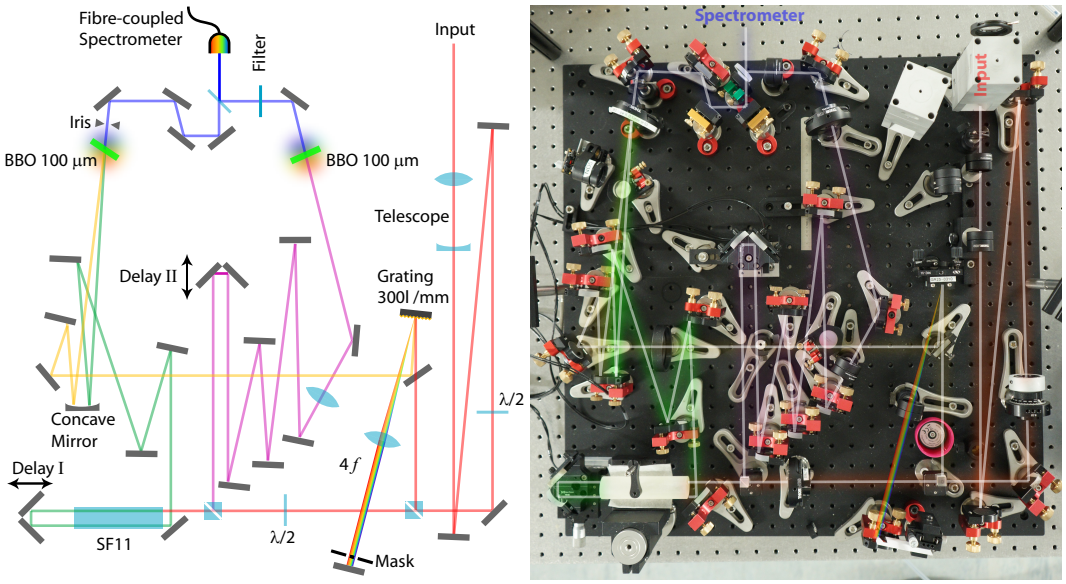


Figure 7.6: **Experimental setup for SPICE**. (red) Input beam ($P = 100\,\mathrm{mW}$), (yellow) test field,(green) ancillary field, (magenta) reference field, and (blue) frequency up-converted test field and reference field.

line) was adjusted using a telescope comprised of a plano-convex and a plano-concave lens. A test pulse with a spectral gap (yellow line) was then prepared using a folded 4-f pulse shaper. The chirped ancillary field was generated using a 10 cm long glass rod (SF11) in a double pass geometry and a retro-reflector which was mounted onto a piezo-driven translation stage (Newport) to adjust the delay τ. Both fields were then focussed into a 100 µm thick BBO crystal $\theta = 53$ degree in order to generate a sum-frequency signal. The reference field was derived directly from the input beam using a 50:50 beamsplitter and frequency-doubled in a 100 µm BBO crystal. The relative delay between the SFG and the SHG signal could be controlled by adjusting the position of a second retro-reflector mounted onto a piezo-driven translation stage. Both signals were then interfered in a collinear geometry and sent into a fibre-coupled spectrometer.

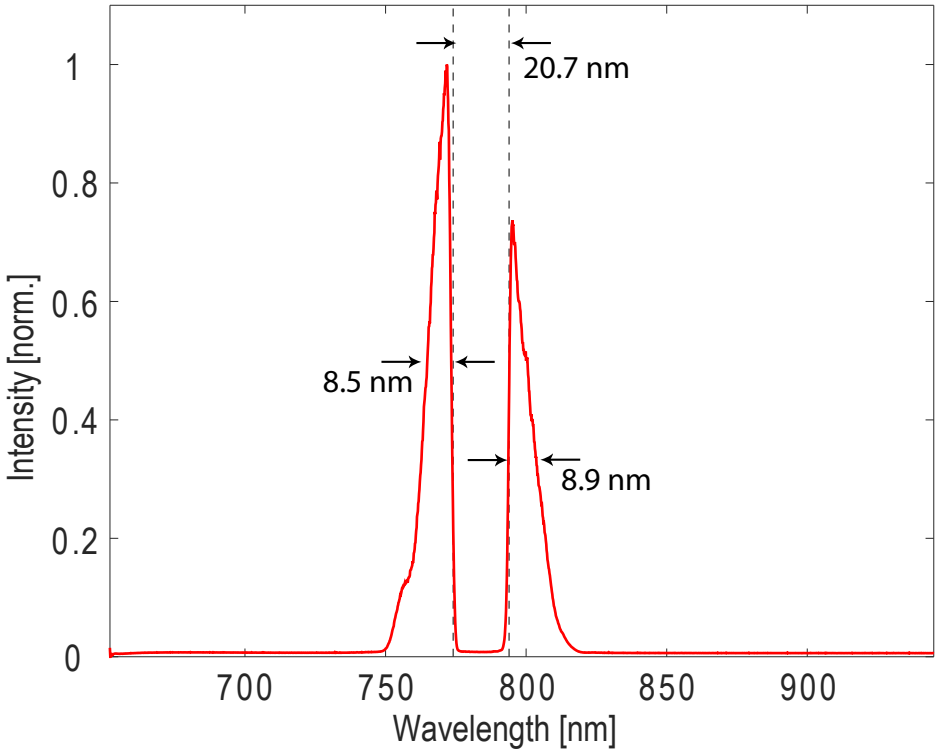


Figure 7.7: **Shaped spectrum of the test pulse** measured after the 4-f pulse shaper. The position and the width of the spectral gap could be adjusted by repositioning a V-shaped amplitude mask mounted onto a XY stage in the Fourier plane of the pulse shaper.

7.3.1 Test pulse preparation

The two-color test pulses were prepared using a 4-f amplitude-only pulse shaper. The input beam of 30 fs pulses was directed onto a grating (300 lines mm^{-1}) which introduced angular dispersion in the horizontal plane. The diffracted beam was then collimated using a bi-convex lens (f = 100 mm) and directed onto a mirror located in the Fourier plane of the pulse shaper, oriented perpendicular to the beam. A spectral gap was introduced into the spectrum of the pulses by blocking the dispersed beam with an amplitude mask (V-shaped cardboard) mounted on top of the mirror. The reflected beam was then re-focussed onto the grating where the spectral components were recombined. The shaped pulses and the chirped ancillary pulse were then focussed into a BBO crystal using a concave mirror.

Figure 7.7 shows a spectrum of the shaped pulses after the 4-f line. The spectra

of the parent pulses are approximately 9 nm wide (FWHM) with an approximately 21 nm wide gap in between. The gap-size and position could be varied by changing the vertical and horizontal position of the amplitude mask.

7.3.2 Shear Calibration

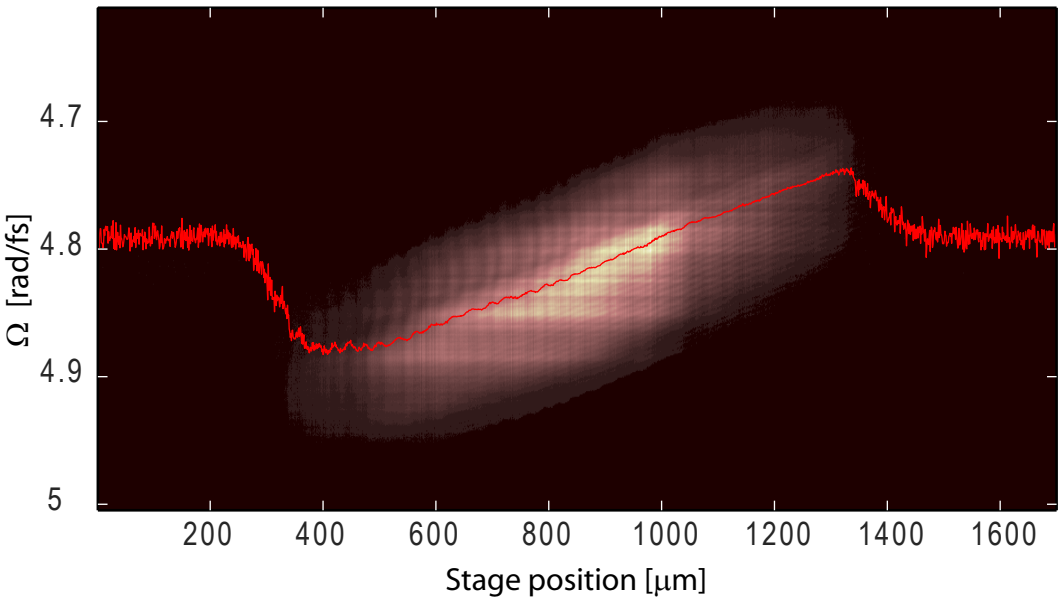


Figure 7.8: **Shear calibration**. The Spectrogram shows the sum-frequency signal of unfiltered test pulse and chirped ancillary pulse for a range of shears. The x-axis shows the position of delay stage I (cf. Fig. 7.6). The red line shows the center of gravity of the measured signal.

The first step in the MICE reconstruction is the calibration of the frequency shear. Figure 7.8 shows the sum-frequency signal of the test pulse (without a spectral gap) and the ancillary pulse for a range of delay stage positions. The red line shows the center of gravity of the signal which was used to determine the frequency shift per shear step. Figure 7.9a/b show the same spectrogram as in Fig. 7.8 on a wavelength scale before and after removing the spectral shear. Figure 7.9c shows the integrated signal of the spectrogram b) for all shears (blue) and the measured fundamental spectrum of the TP plotted at the doubled frequency (blue). Figure 7.9c shows, that the phase-matching bandwidth of the BBO crystal

used was large enough to cover the entire spectrum of the test pulse and, in case of a gap cut into the test pulse spectrum, enabled "bridging" the spectral gap. The doubling bandwidth (FWHM) $d\lambda \approx 73\,\text{nm}$ of the BBO crystal used can be estimated using equation (2.23) and was approximately two times larger than the spectral bandwidth of the test pulses ($\sim 36\,\text{nm}$).

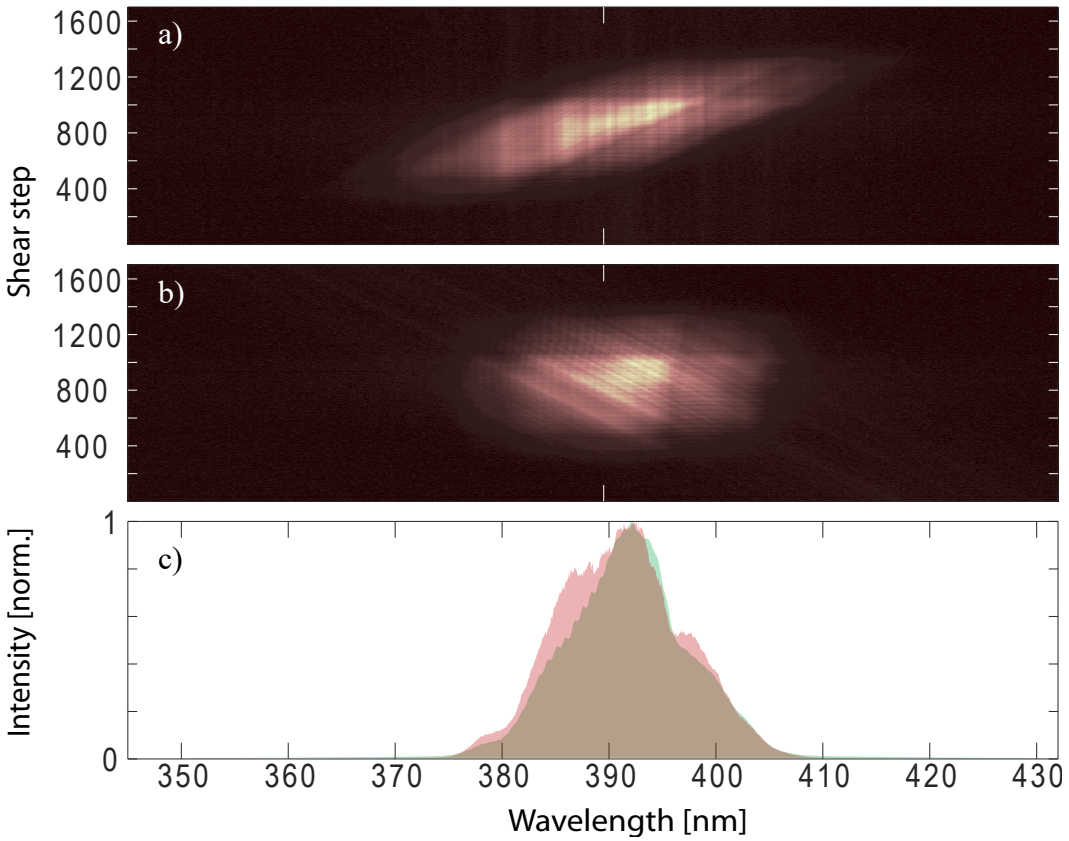


Figure 7.9: **Shear calibration**. a) Measured spectrum of the sheared, unshaped TP. b) The same spectrum as in a) after removing the shear. c) Spectral intensity of the TP integrated over all shears (green) and spectrum of the TP measured at the fundamental wavelength (red).

7.3.3 SPICE interferogram

Figure 7.10a/b shows the spectrogram of the unfiltered and filtered TP. Figure 7.10c/d show the recorded SPICE interferograms for the unfiltered and filtered TP. The vertical structure that can be seen is the frequency-doubled spectrum of the RP. The horizontal, stripy structure of the spectrogram and interferogram are

caused by variation in laser output power over the period of the scan. For the used input pulse energy 100 µJ, the time for one scan was approximately 5 min.

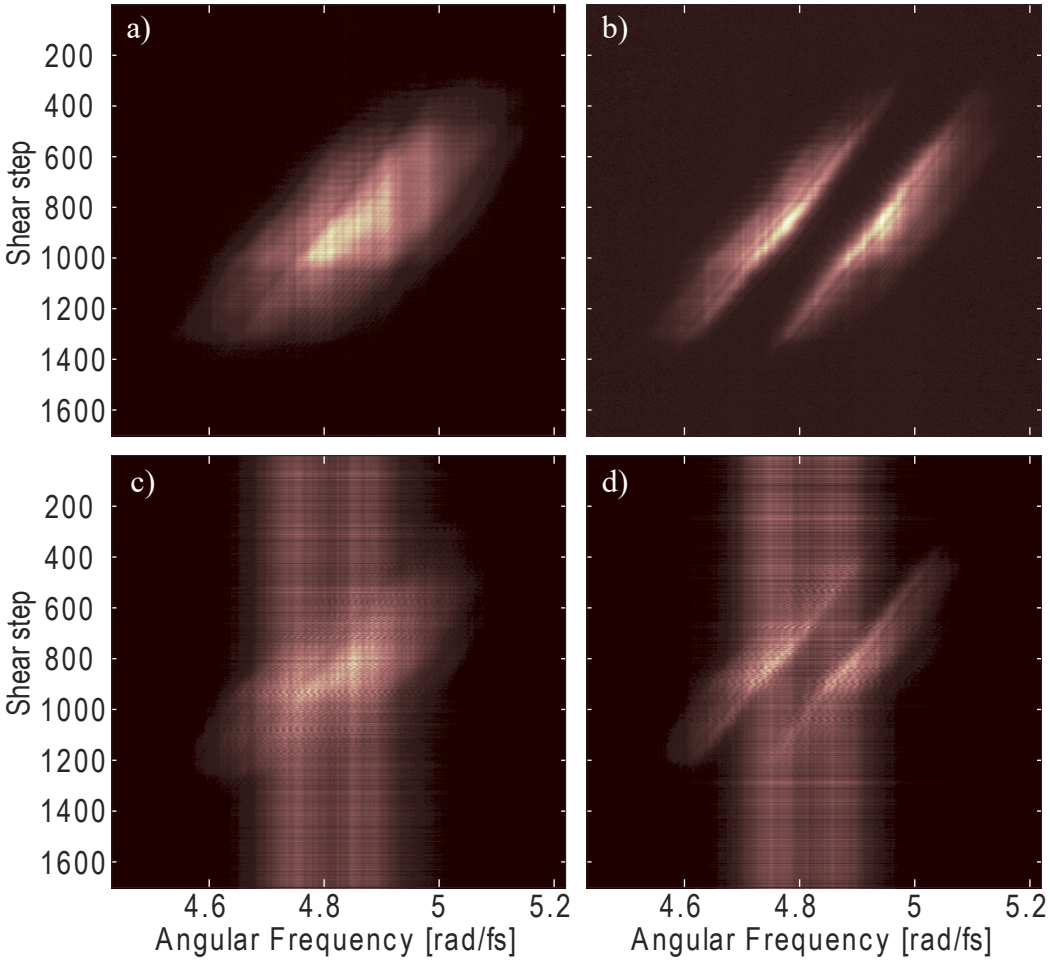


Figure 7.10: **SPICE interferograms**. a) Spectrum of the TP for a range of shears. b) Spectrum of the sheared, shaped TP with spectral gap. c) Interferogram of TP and RP. d) Interferogram of shaped TP and RP.

7.4 Results

The MICE routine aims to find three complex electric fields which reproduce the measured set of SPICE interferograms. The MICE routine is seeded with an initial guess of the amplitude and phase which in the present case was random noise. After iteratively solving equations (7.5)-(7.7), the interferometric product generated

by the reconstructed fields resembled the measured interferometric product for the true fields. Comparing the measured interferometric product to the reconstructed, yields the SPICE error and shows convergence of the algorithm onto the correct solution.

Figure 7.11 shows the measured and reconstructed AC-sidebands for an interferogram of RP and unfiltered TP after 10 iterations of the MICE algorithm. As can be seen, the reconstructed AC-sideband is in good agreement with the measured interferometric product.

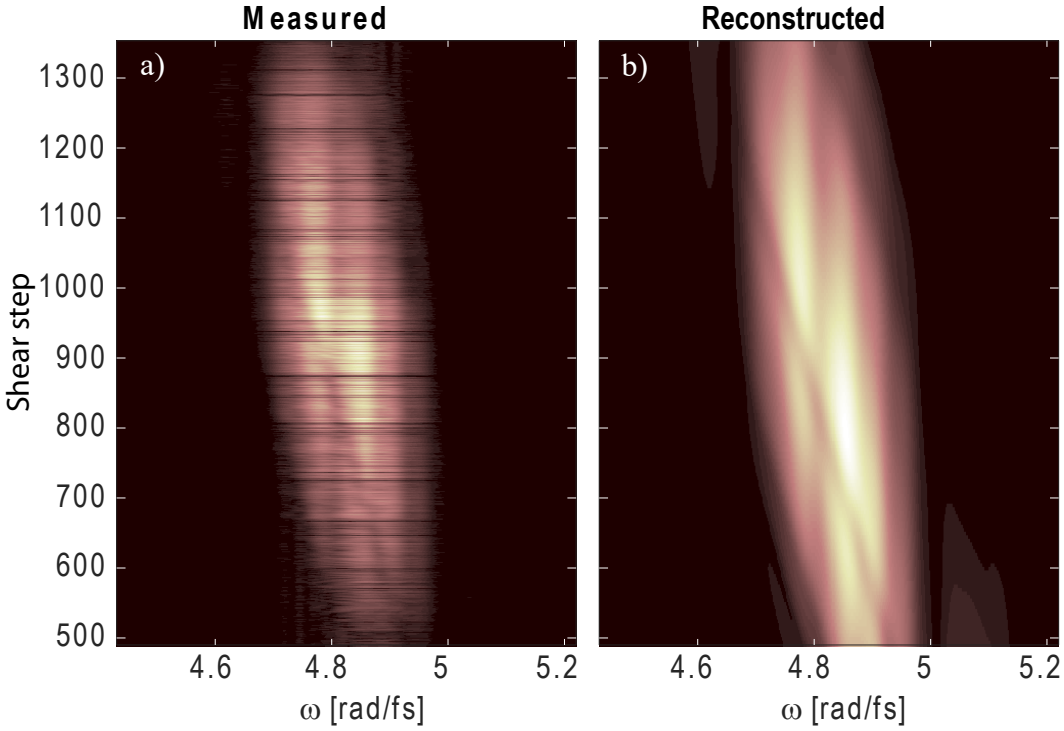


Figure 7.11: **Retrieved interferometric product**. a) Measured interferometric product (after shear calibration and Fourier-filtering). b) Retrieved interferometric product after 10 iterations of the MICE algorithm.

Figure 7.12 shows the measured and reconstructed AC-sidebands for an interferogram of RP and filtered TP after 10 iterations of the MICE algorithm. As can be seen, reconstructed and measured AC-sidebands are in good agreement.

Figure 7.13 shows the result of SPICE for RP and TP for a couple of SPICE scans. For Fig. 7.13a/b, scans were performed for test pulses with an unshaped

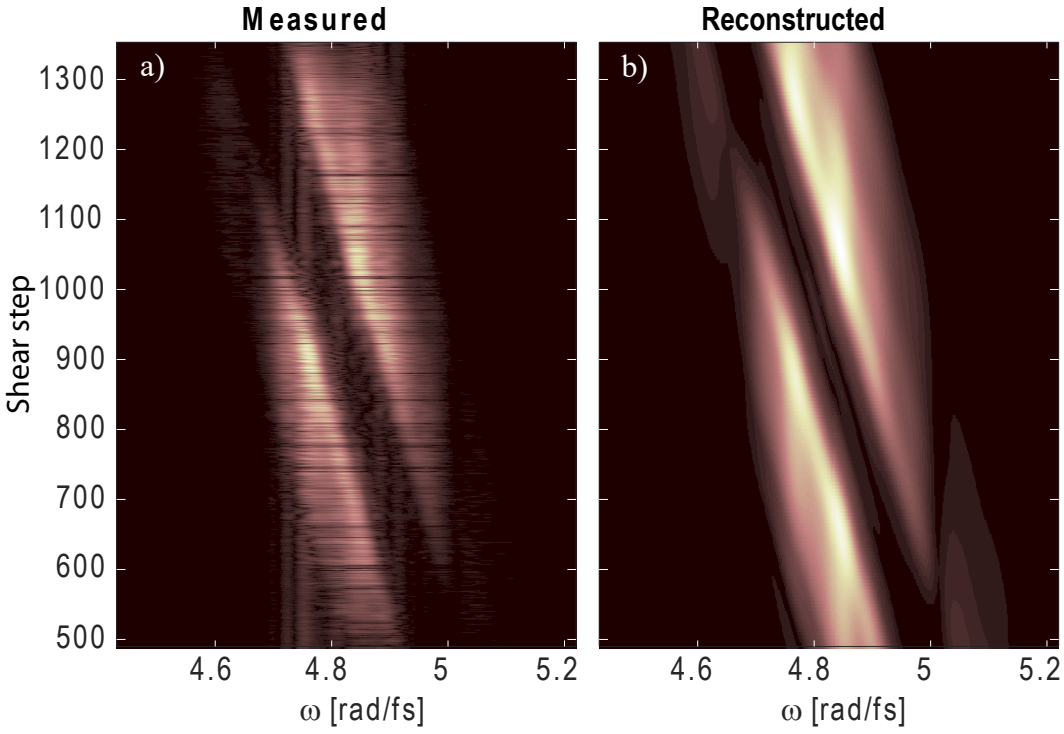


Figure 7.12: **Retrieved interferometric product**. a) Measured interferometric product (after shear calibration and Fourier-filtering). b) Retrieved interferometric product after 10 iterations of the MICE algorithm.

spectrum and for the case of a spectral gap. It can be seen in Fig. 7.13b, that the relative spectral phase of the parent pulses agree with the spectral phase at the same spectral position in case of an unshaped pulse. This shows that the SPICE technique is capable of correctly reconstructing the relative spectral phase across the spectral gap. It should be noted that the spectral phase within the gap is undefined wherever the recorded intensity is nil. However, due to measurement noise and seed-noise in the reconstruction, the MICE algorithm converges to a finite value for the spectral phase. In the present case, the amplitude modulation of the RP spectrum also contributes the residual signal in the spectral gap of the filtered AC-sideband which is approximately 18 dB above the experimental noise floor. This can be seen in the gap of the AC-sideband shown in Fig. 7.12a. The residual signal could be significantly reduced by reducing the spectral modulations in the RP spectrum which are most likely caused by the experimental setup, or

by optimizing the delay between RP and TP (Delay II, cf. Fig. 7.6), in order to better separate the contributions of the interferometric product of RP and TP and the contributions from the spectral intensity modulation of the RP to the AC-component of the interferogram.

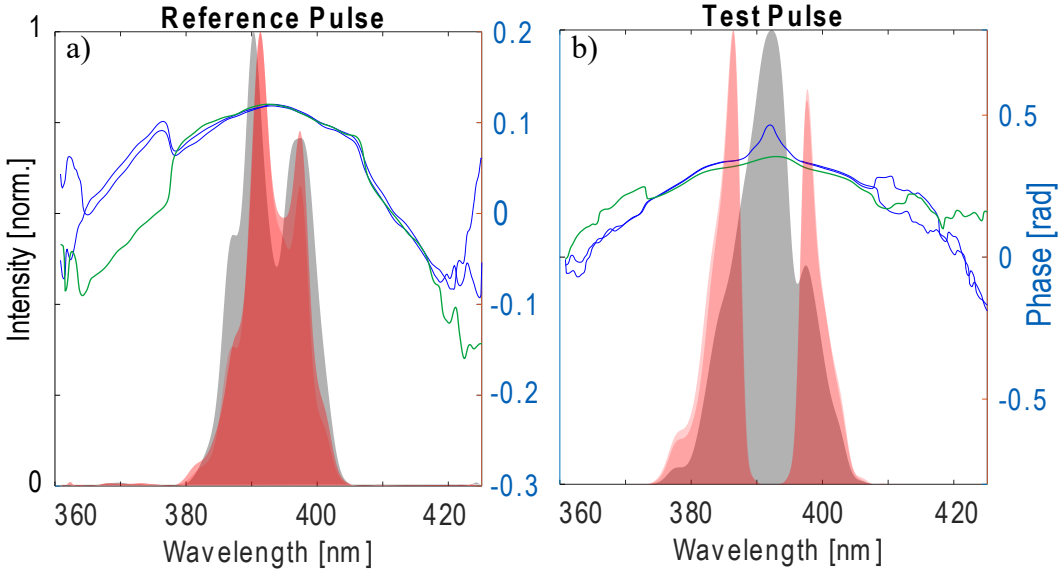


Figure 7.13: **SPICE Reconstruction**. a) Retrieved spectral intensities and spectral phases of the reference field for multiple SPICE measurements. RP spectral intensity and phase for the case of an unfiltered TP (grey and green); intensity and phase for the case of a shaped TP (red and blue). b) Retrieved spectral intensity and phase of the test field for the case of an unfiltered TP (grey and green) and spectral intensity for the case of a TP with a spectral gap (red and blue).

Figure 7.14 shows SPICE for different TP with a range of different gap sizes. As can be seen, the relative spectral phase of the parent pulses is conserved, and the reconstruction is not significantly affected by a larger gap size. It should be noted that results from multiple SPICE measurements are combined in one plot. The greater variation in the reconstructed spectral phases is mainly the result of a change in the pulse compression of the laser due to temperature variation in the laboratory over a period of approximately 90 min.

As outlined in section 7.1.1, the spectral intensities of RP and TP cannot be retrieved unambiguously by taking into account the AC-sidebands of the measured interferograms only. However, the spectrum of RP and TP can be recovered using

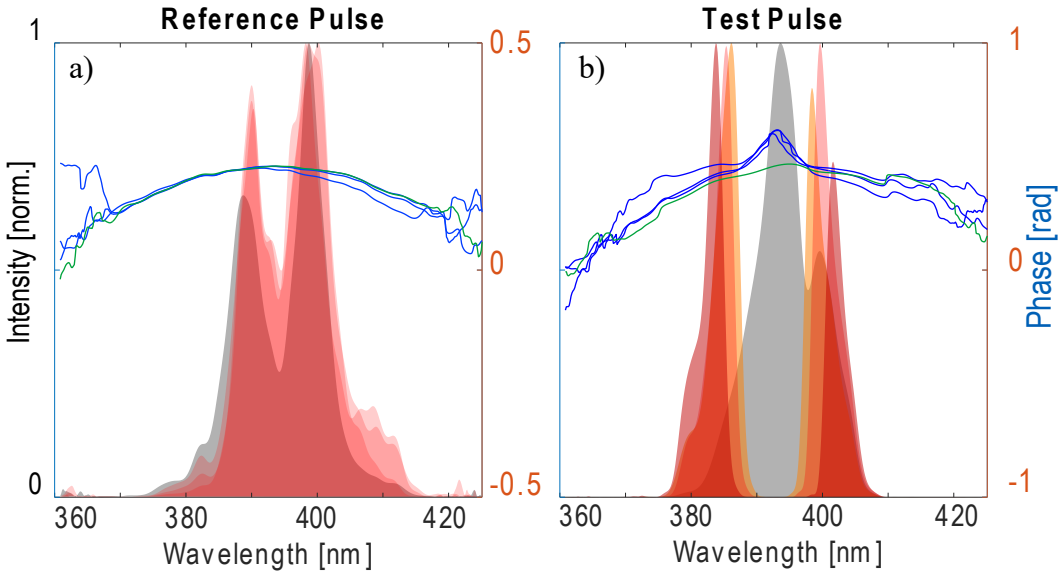


Figure 7.14: **SPICE Reconstruction for different gap sizes**. a) Reconstructed spectral intensity and phase for the RP in case of unshaped TP (grey and green) and shaped TP (red and blue). b) Retrieved spectral intensity and phase of TP for unshaped case (grey and green) and for TPs with various gap-size (red and blue).

the DC-component of the measured interferogram or measured directly either by using the SFG and SHG signal or by measuring the spectra of the RP and TP at their fundamental wavelengths. It should be noted that, on the one hand, the absolute amplitude of the frequency-doubled TP and RP should not impact the phase-retrieval, since the phase information is encoded in the fringe spacing, on the other hand, full temporal characterization of TP and RP includes knowing the exact spectral amplitudes of both fields. Figure 7.15a shows the measured SHG signal of the RP (green) and the spectral intensities retrieved from the AC-component of the interferogram (grey). As can be seen, the two spectra show similarities but do not agree to a full extent. Figure 7.15b shows the filtered TP after shear calibration and integrated over all shears (green) and the spectrum of the same TP measured at the fundamental wavelength (red). As can be seen, both spectra agree to a large extent (orange area). However, there are slight discrepancies between the fundamental spectrum and the spectrum of the SFG

signal which are most likely the result of improper phase-matching. Therefore, direct measurement of the TP and RP spectra yields the more accurate results.

The robustness of MICE and SPICE has been studied in the past [6, 8, 106, 107] where both techniques were found to be fast-converging and extraordinarily resilient to noise. For the individual reconstructions shown in Fig. 7.13 and in Fig. 7.14, the MICE algorithm was convergent after less than 10 iterations with a normalized reconstruction error $\epsilon / \sum_{j,k} |AC^{meas}|^2$ below 2% after 3 iterations and below 1% after 10 iterations. This is in good agreement with the convergence behavior found in previous studies [6, 8, 106, 107].

Comparing the difference between the measured AC-terms $\delta AC_{i,j}^{meas}$ and retrieved AC-terms $\delta AC_{i,j}^{ret}$ for the i^{th} and j^{th} measurement allows for estimating the robustness of SPICE against small input variations, i.e. by which amount a SPICE reconstruction changes for a given change of the input signal. For the results presented in Fig. 7.13 and in Fig. 7.14 a linear dependence was found with $\delta AC_{i,j}^{ret} / \delta AC_{i,j}^{meas} = (0.954 \pm 0.025)$. This shows that the amount of change in the input signal is reflected in a comparable amount of change in the reconstruction result. For three to four repeated measurements shown in Fig. 7.13 and in Fig. 7.14, the relative standard deviation resulting from stability of the laser source and random measurement error is below 12% for the reconstructed phase in the spectral region between 375 nm and 410 nm where the measured intensity signal is above the noise floor.

7.5 Conclusion

In this chapter, simultaneous characterization of two mutually coherent, complex fields was demonstrated using the SPICE technique. The use of a temporally chirped ancillary field enabled SPICE without a phase ambiguity resulting from STC of the ancillary field as observed in previous experiments [6]. This eliminates

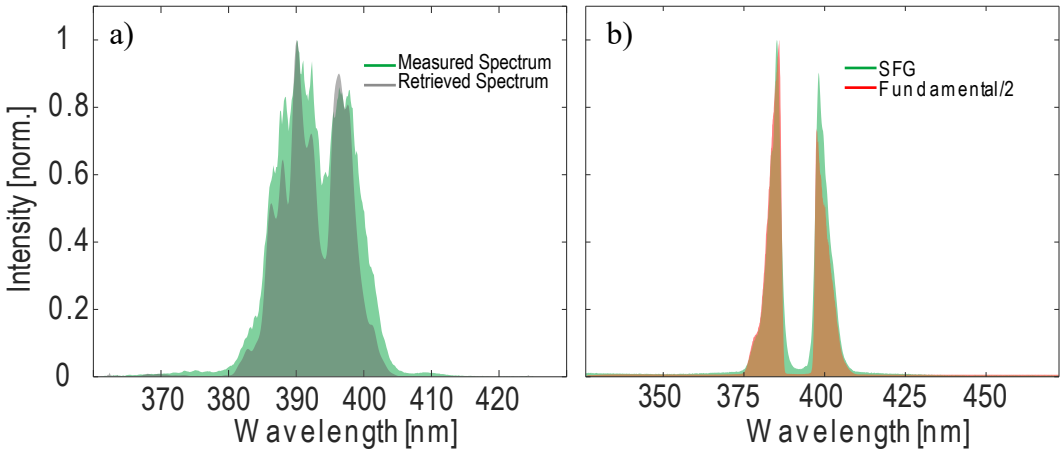


Figure 7.15: **Measured and retrieved spectral intensity**. a) Measured spectrum of the RP (green) and retrieved spectrum (grey). b) Measured spectrum of the frequency-doubled TP, integrated over all shears (green) and spectrum of the same TP measured directly at the fundamental wavelength and extrapolated to the frequency-doubled wavelength scale(red).

the need of laborious calibration of the SPICE setup for STC. The experimental results show that SPICE is capable of reconstructing the spectral phase across an extended spectral gap and that the spectral-gap size does not significantly influence the accuracy of the phase retrieval.

Chapter 8

Conclusion

8.1 Summary

The desire to study the dynamics of the microscopic world has made attoscience to one of the most fascinating fields of modern physics and technology. Observing and controlling the dynamics in the microscopic world requires tools of extraordinary spatial and temporal resolution. Today, high-harmonic generation represents a versatile table-top light source, capable of generating short-wavelength radiation with excellent temporal and spatial coherence. Not only can HHG sources be operated at a fraction of the costs required to operate other types of light sources such as synchrotron light sources or free-electron lasers, but often also with far better spatial and temporal coherence. On the one hand, the excellent temporal coherence properties of HHG enables generating pulses of light as short as a few hundred attoseconds which can be used as a probing tool in spectroscopy and for recording molecular movies. On the other hand, coherent microscopy techniques such as ptychography are an important tool for non-destructive imaging of, for instance, (living) biological samples [38, 108, 109]. At the same time, semiconductor industry has pushed the boundaries of spatial resolution in lithography to the few-nanometre scale. Therefore, the demand for a bright, tabletop source of

coherent short-wavelength light for applications in science and technology is high.

High-harmonic generation driven with high average power fibre lasers or optical parametric chirped-pulse amplifiers provides a promising route towards such light sources. However, the low drive pulse energies delivered from such lasers necessitates new generation schemes in order to increase the conversion efficiency. In the past, gas-filled capillary waveguides have very been used to increase the efficiency of HHG. However, scaling this concept to low pulse energy drivers is challenging, since it would require using waveguides with very small core diameter in order to reach sufficient intensity to drive HHG. On the one hand, this requires technologically challenging, multi-atmosphere gas pressures to phase-match HHG [65]. On the other hand, the small core diameter and the resulting high modal attenuation in such waveguides hinders the application of quasi-phase-matching techniques such as periodically modulating the diameter of the hollow waveguide [68] or multi-mode quasi-phase-matching [66, 69] which have shown to significantly increase the HHG yield at lower gas-pressures. This limitation can be mitigated by generating harmonics in gas-filled hollow-core photonic crystal fibres which exhibit significantly lower guiding loss. A proof-of-concept study conducted by Heckl and co-workers [5] has shown that, in absence of phase-matching or quasi-phase-matching, HHG can be driven with few-microjoule drive pulses in PCF with low efficiency. The low conversion efficiency hinders the application of PCF to HHG using few-microjoule drive pulses delivered from modern high average-power lasers. In the present thesis, intermodal delay-controlled quasi-phase-matching (IDC-QPM, XIDC-QPM), a novel quasi-phase-matching technique, was developed and demonstrated which enables quasi-phase-matched HHG in gas-filled PCF. IDC-QPM was applied to HHG in an argon-filled PCF and enabled increasing the HHG yield by two orders of magnitude.

For applications such as the generation of isolated attosecond pulses, control over the driver waveform is paramount. High-harmonic generation using sythe-

sized driver waveforms, such as multi-colour pulses, could open the door to an entirely new generation of experiments in atomic, molecular and optical science. Temporal characterization of these driving fields is not possible using established pulse characterization techniques such as SPIDER or FROG, if the spectra of these pulses contain extended spectral gaps. In the present thesis, a spectral-gap-immune pulse characterization technique (SPICE) was successfully demonstrated. Two mutually coherent pulses, a test and a reference pulse, where derived from a Ti:Sapphire laser source. An extended spectral gap was introduced into the spectrum of the test pulse using an amplitude-only pulse shaper. This test field was frequency sheared by using sum-frequency generation with an temporally chirped ancillary field, derived from the same laser source, and subsequently interferred with the frequency doubled reference pulse. By using the MICE approach, the spectral intensities and phases of the test and the reference field could be retrieved from a series of interferrograms. The use of a temporal chirp instead of a spatial chirp enabled a frequency shear of the test pulse without a phase ambiguity resulting from STC of the ancillary field, as observed in previous experiments [6]. This eliminates the need of laborious calibration of the SPICE setup for STC. The experimental results show that SPICE is capable of reconstructing the spectral phase across an extended spectral gap and that the spectral-gap size does not significantly influence the accuracy of the phase retrieval.

8.2 Outlook

8.2.1 HHG driven with high-average power

The harmonic fluxes generated using the driving pulse energy and peak power in the experiments presented in chapter 4 and chapter 5 open the prospect of scaling efficient HHG to few-MHz repetition rates and high average driving powers using

Yb-based thin-disk lasers, fibre-CPAs or high repetition rate, optical parametric chirped-pulse amplifiers (OPCPA) [83, 84, 110, 111]. OPCPAs can deliver high peak power pulses in the mid-infrared (MIR). However, HHG with MIR pulses is more of a challenge since the phase-matching pressure scales with λ^2 [112]. Therefore, quasi-phase-matching techniques of the type described in this thesis could be of even greater importance for long wavelength driving laser pulses. Driving HHG in the NIR with lanthanide-based fiber-CPAs and thin-disk lasers requires pulse compression. Pulse post-compression has recently been demonstrated in gas-filled NC-PCFs [113, 114] and Kagome-PCFs [19] and has enabled wavelength-tunable HHG in a gas jet placed directly behind the output of the fibre. In the work described in the preceding chapters, by generating directly in a NC-PCF and employing IDC-QPM and XIDC-QPM, at least ten times higher conversion efficiency has been reached for similar driving pulse energies. It should be noted that no significant damage to the NC-PCF was observed over an operation period of several hours, even at average driving power beyond 50 mW. Guidance of continuous laser power of up to 36 W within a NC-PCF of similar design type has already been demonstrated in experiment by Jaworski and co-workers [115]. Hence, scaling the present approach to multi-watt NIR or MIR average driving powers provides a promising route to high average power, short wavelength light sources extending into the soft x-ray region.

8.2.2 XUV-MICE

Mutual interferometric characterization of a pair of independent electric fields has been successfully applied to the XUV domain for wavefront characterization of an HHG beam [106, 8, 107]. A key challenge in attoscience is the temporal characterization of a HHG source. Current techniques are mostly based on nonlinear light–matter interactions which are often experimentally involved. Therefore, an

all-optical attosecond-pulse characterization technique is of great interest. Early studies by Mairesse and co-workers [116] implemented a XUV-variant of SPIDER and Pedatzur and co-workers [117] recently demonstrated all-optical approaches for temporal characterization of a HHG source based on double-blind holography. The approach taken by Mairesse et al. used frequency shearing interferometry in the XUV domain. This was made possible by spectrally shaping a HHG drive pulse using a programmable acousto optic dispersive filter (Fastlite, DAZZLER). Two delayed and spectrally sheared quasi-replica pulses from a Ti:Sapphire laser oscillator were generated, amplified and subsequently used to drive HHG in an argon gas-jet. The two pulses with slightly different fundamental wavelengths caused generation of two quasi-independent XUV pulse trains which were frequency-sheared according to the frequency-shear of the drive pulses. A XUV interferogram was recorded for the 11^{th} harmonic using a XUV spectrometer and the spectral phase of H11 was extracted using SPIDER approach (cf. section 6.3). However, the method presented by Mairesse and co-workers is not applicable to the attosecond domain, since this would require reconstructing the spectral phase across an entire harmonic spectrum, i.e. across many extended spectral gaps. At the same time, the technique is limited due to the fact that the two drive pulses have to be sheared replicas.

The approach taken by Pedatzur and co-workers used a double-blind holographic phase retrieval. As set out in section 6.3, the relative spatial or spectral phase of two interfering signals is encoded in the intensity modulations of the hologram (interferogram). In case one of these signals is well-characterized, the missing spectral phase of the other signal can be retrieved from these fringes. In case both phases are unknown, blind holographic phase retrieval can be applied to reconstruct the spectral phases of the two signals, if constraints can be applied that enable finding a unique solution to the phase retrieval problem (cf. section 6.2). One such constraint can be a ‘compact temporal support’ of the signals,

i.e. a finite temporal duration, as applied in [117]. The authors generated two independent attosecond signals and recorded the individual spectra as well as the interferogram. Using the constraint of a compact temporal support, they were able to reconstruct the spectral phase from the recorded interferogram using an iterative approach. XUV-MICE could yet provide another important approach to an all-optical, fully spatio-temporal characterization of attosecond pulses. In order to perform spectral shearing MICE in the XUV domain, multiple spectral shears need to be applied to one of two interfering harmonics beams. This may be achieved using a pulse shaper similar as done in [116]. However, the use of gas-filled PCF enables generating harmonics using significant lower drive pulse energies which would enable using a DAZZLER to shape the drive pulse directly after the laser amplifier, making the frequency shear much more controllable and reliable. Another interesting approach to a tunable HHG source could be using a tunable OPA as a driver source, such as done for instance in [118], or by frequency shearing the drive pulse as done for the SPICE experiment presented in chapter 7. Recent studies [119] have demonstrated that HHG can be driven using shorter wavelength drivers with acceptable efficiency, in this case a frequency-tripled Ti:Sapphire laser at $\lambda_0 = 270\,\mathrm{nm}$. Thus, two mutually coherent harmonic sources could be realized in argon-filled PCFs using two laser beams $\lambda = 400\,\mathrm{nm}$ derived from a Ti:Sapphire laser system. A frequency shear in the XUV could be achieved by shearing the drive pulse using SFG of the signal with a chirped ancillary pulse. The harmonic signal from this source could then be interfered with a second HHG signal driven with a frequency-doubled Ti:Sapphire laser. Using the MICE routine, the spectral phase across the harmonic spectrum could be retrieved, enabling an all-optical temporal characterization of the HHG source.

8.2.3 Blind digital holographic microscopy

The MICE approach has proven to be a very robust method for wavefront characterization of high-harmonic beams [107, 8]. Therefore, another important application of MICE could be holograpic imaging.

There are two common approaches to coherent imaging. The first approach consists of holographic techniques, and in particular digital holographic microscopy. In this scheme, a probe beam is scattered from a sample and subsequently interfered with a fully characterized reference beam. The amplitude and phase of the scattered probe beam can be extracted from the recorded hologram, since the reference amplitude and phase are known. The second family of techniques rely on (iterative) phase retieval from scattering patterns alone. This approach requires additional constraints to the phase retrieval problem as outlined in the previous sections. This can be done by applying some a-priori knowledge or by sufficient oversampling. In practice, this requires recording a series of diffraction patterns for different sample illuminations while ensuring a certain degree of redundancy in the recorded data. One particularly successful scheme of this type is ptychography [120]. In this approach, leastsquares minimization leads to strong noise suppression. Such improvements have led to wide acceptance of this technique in X-ray scattering experiments where imperfect illumination is commonplace.

Blind digital holographic microscopy (BDHM) using the MICE approach can yield images with resolution limited only by the numerical aperture of the arrangement, and with the additional feature that the reference beam need not be characterized. At the same time, the combined advantages of the interferometric approach and least-squres minimization lead to extraordinary resilience to noise and low signal-to-noise ratios (SNRs), as has been demonstrated previously [106].

Figure 8.1 shows the proposed geometry for XUV-BDHM. First, spatially separated probe and reference beams are derived. Next, the probe is scattered by the

sample before propagating to the detector where it interferes with the reference. A sequence of holograms is recorded as the reference is raster scanned across the detector. Using a 2D-version of the MICE algorithm, amplitude and phase of the sample beam and reference beam can be retrieved from the series of holograms.

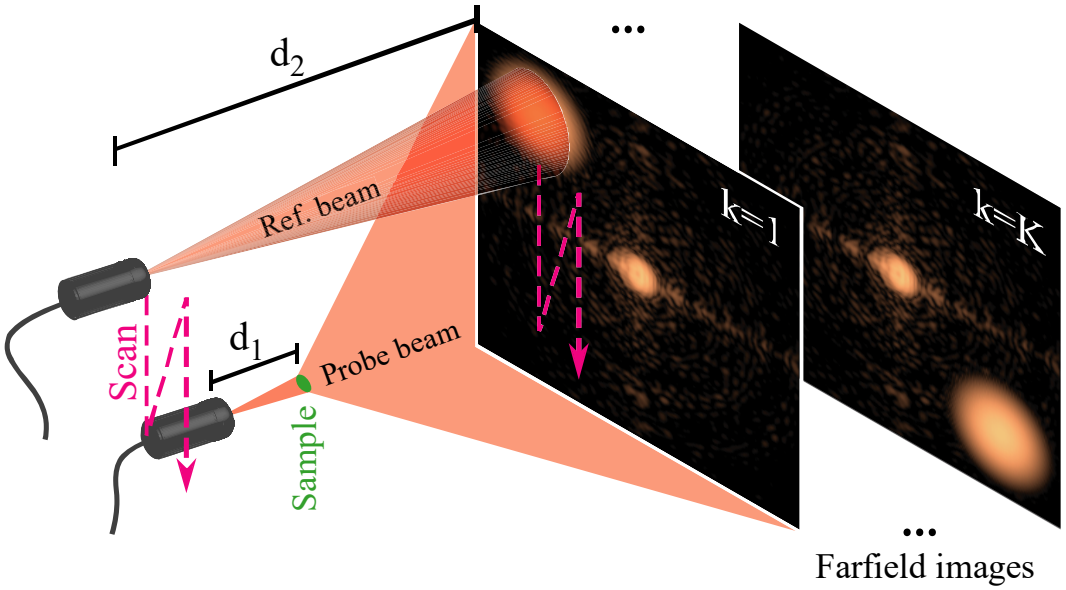


Figure 8.1: **Blind digital holographic microscopy**. Illustration of the proposed geometry. First, spatially separated probe and reference beams are derived. Next, the probe is scattered by sample before propagating to the detector where it interferes with the reference. A sequence of holograms is recorded as the reference is raster scanned across the detector.

The results of a proof-of-concept demonstration recently performed[1] at the University of Oxford and lead by scientist Dr. Patrick Anderson can be seen in Fig. 8.2. The probe and a reference beams were derived from a helium-neon laser ($\lambda = 633\,\text{nm}$). The main figure shows the reconstructed probe field amplitudes retrieved from a sequence of 224 holograms. The figure inlay shows the field amplitude of the heavily distorted reference beam. The results demonstrate that BDHM not only eliminates the need for a well-characterized reference beam but also relaxes the requirements for beam quality of the reference beam. The extraordinary resilience

[1]The author complemented the study with theoretical work regarding the noise performance of BDHM.

against low SNRs, coherent noise and beam distortions makes this approach very attractive for imaging applications in the XUV domain.

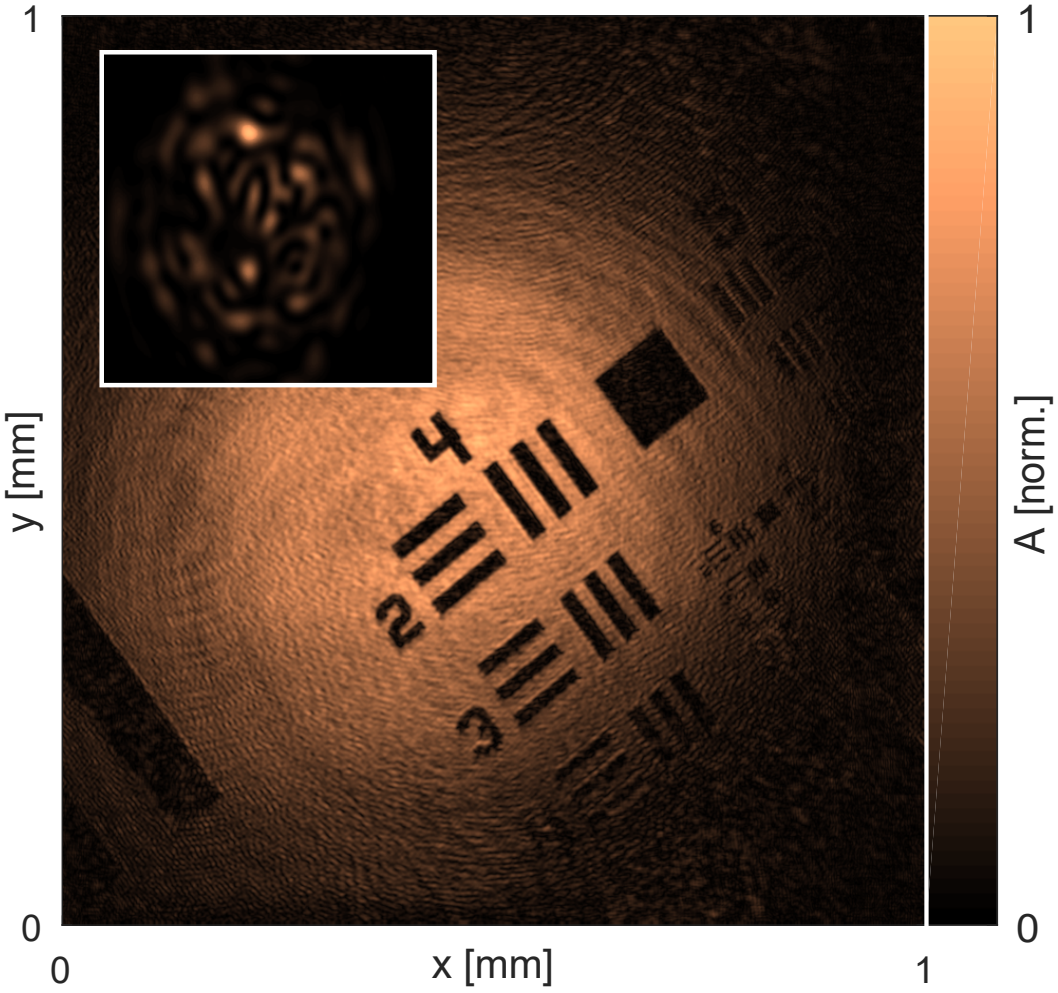


Figure 8.2: **Experimental imaging of resolution test target**. The probe field amplitude retrieved from a sequence of 224 holograms backpropagated to the sample. The inset shows the amplitude (at the detector) of the severely distorted reference field, plotted on the same scale as the main figure.

Acknowledgements

First and foremost, I want to thank Patrick Anderson who spent many hours in the laboratory with me while assembling the high-harmonic beamline in the Oxford Attosciencelab.

I want to thank my supervisors Professor Simon Hooker and Professor Ian Walmsley who have provided me with immeasurable support as well as advice in many difficult situations in the laboratory and elsewhere.

Finally, I want to thank the European Comission for the generous support of my doctorate through the Marie Skłodowska-Curie actions and all my colleagues in the "Horizon 2020" network "HICONO" with whom I spent many joyful moments in the laboratory and on conferences in different parts of Europe and the world.

Bibliography

[1] T. Maiman, "Stimulated optical radiation in ruby." *Nature*, vol. 187, pp. 493–494, 1960.

[2] P. F. Moulton, "Spectroscopic and laser characteristics of ti:al2o3," *J. Opt. Soc. Am. B*, vol. 3, no. 1, pp. 125–133, Jan 1986.

[3] D. Strickland. (2018) Nobel lecture: Generating high-intensity ultrashort optical pulses. [Online]. Available: https://www.nobelprize.org/prizes/physics/2018/strickland/lecture/

[4] A. Rundquist, C. G. Durfee, Z. Chang, C. Herne, S. Backus, M. M. Murnane, and H. C. Kapteyn, "Phase-matched generation of coherent soft x-rays," *Science*, vol. 280, no. 5368, pp. 1412–1415, 1998.

[5] O. H. Heckl, C. R. E. Baer, C. Kränkel, S. V. Marchese, F. Schapper, M. Holler, T. Südmeyer, J. S. Robinson, J. W. G. Tisch, F. Couny, P. Light, F. Benabid, and U. Keller, "High harmonic generation in a gas-filled hollow-core photonic crystal fiber," *Applied Physics B*, vol. 97, no. 2, p. 369, Oct 2009. [Online]. Available: https://doi.org/10.1007/s00340-009-3771-x

[6] I. Gianani, "Characterisation of ultrashort light pulses." Ph.D. dissertation, University of Oxford, 2017.

[7] I. Walmsley, L. Waxer, and C. Dorrer, "The role of dispersion in ultrafast optics," *Review of Scientific Instruments*, vol. 72, no. 1, pp. 1–29, 2001.

[8] M. Mang, "Interferometric spatio-temporal characterisation of ultrashort light pulses." Ph.D. dissertation, University of Oxford, 2014.

[9] R. W. Boyd, *Nonlinear Optics*. Elsevier Science, 2008.

[10] J. A. Armstrong, N. Bloembergen, J. Ducuing, and P. S. Pershan, "Interactions between light waves in a nonlinear dielectric," *Phys. Rev.*, vol. 127, pp. 1918–1939, Sep 1962.

[11] P. L. Kelley, "Self-focusing of optical beams," *Phys. Rev. Lett.*, vol. 15, pp. 1005–1008, Dec 1965.

[12] R. L. Carman, R. Y. Chiao, and P. L. Kelley, "Observation of degenerate stimulated four-photon interaction and four-wave parametric amplification," *Phys. Rev. Lett.*, vol. 17, pp. 1281–1283, Dec 1966.

[13] I. D. Abella, "Optical double-photon absorption in cesium vapor," *Phys. Rev. Lett.*, vol. 9, pp. 453–455, Dec 1962.

[14] P. A. Franken, A. E. Hill, C. W. Peters, and G. Weinreich, "Generation of optical harmonics," *Phys. Rev. Lett.*, vol. 7, pp. 118–119, Aug 1961.

[15] C. Hirlimann, *Femtosecond Laser Pulses*, C. Rullière, Ed. Springer, 2005.

[16] R. Trebino and E. Zeek, *Frequency-Resolved Optical Gating: The Measurement of Ultrashort Laser Pulses*. Kluwer Academic Publishers, 2000.

[17] F. Parmigiani, C. Finot, K. Mukasa, M. Ibsen, M. A. F. Roelens, P. Petropoulos, and D. J. Richardson, "Ultra-flat spm-broadened spectra in a highly nonlinear fiber using parabolic pulses formed in a fiber bragg grating," *Opt. Express*, vol. 14, no. 17, pp. 7617–7622, 2006.

[18] S. C. Rae and K. Burnett, "Detailed simulations of plasma-induced spectral blueshifting," *Phys. Rev. A*, vol. 46, pp. 1084–1090, Jul 1992.

[19] F. Tani, M. H. Frosz, J. C. Travers, and P. S. Russell, "Continuously wavelength-tunable high harmonic generation via soliton dynamics," *Opt. Lett.*, vol. 42, no. 9, pp. 1768–1771, May 2017. [Online]. Available: http://ol.osa.org/abstract.cfm?URI=ol-42-9-1768

[20] A. L'Huillier, P. Balcou, S. Candel, K. J. Schafer, and K. C. Kulander, "Calculations of high-order harmonic-generation processes in xenon at 1064 nm," *Phys. Rev. A*, vol. 46, pp. 2778–2790, Sep 1992.

[21] J. R. Carson, S. P. Mead, and S. A. Schelkunoff, "Hyper-frequency wave guides — mathematical theory," *The Bell System Technical Journal*, vol. 15, no. 2, pp. 310–333, April 1936.

[22] E. A. J. Marcatili and R. A. Schmeltzer, "Hollow metallic and dielectric waveguides for long distance optical transmission and lasers," *Bell Syst. Tech. J., 43, 1783, (1964)*, vol. 43, p. 1783, 1964. [Online]. Available: https://doi.org/10.1002/j.1538-7305.1964.tb04108.x

[23] M. Miyagi and S. Karasawa, "Waveguide losses in sharply bent circular hollow waveguides," *Appl. Opt.*, vol. 29, no. 3, pp. 367–370, Jan 1990.

[24] J. M. Senior, *Optical Fiber Communications: Principles and Practice*, 2009.

[25] J. A. Buck, *Fundamentals of Optical Fibers*. Wiley, 2004.

[26] R. K. Nubling and J. A. Harrington, "Launch conditions and mode coupling in hollow-glass waveguides," *Optical Engineering*, vol. 37, no. 9, pp. 2454 – 2458, 1998.

[27] T. A. Robinson, "Quasi-phase-matching of high-harmonic generation," Ph.D. dissertation, Oxford University, UK, 2009.

[28] T. Pfeifer and M. C. Downer, "Direct experimental observation of periodic intensity modulation along a straight hollow-core optical waveguide," *J.*

Opt. Soc. Am. B, vol. 24, no. 5, pp. 1025–1029, May 2007. [Online]. Available: http://josab.osa.org/abstract.cfm?URI=josab-24-5-1025

[29] M. A. Duguay, Y. Kokubun, T. L. Koch, and L. Pfeiffer, "Antiresonant reflecting optical waveguides in sio2-si multilayer structures," *Applied Physics Letters*, vol. 49, no. 1, pp. 13–15, 1986. [Online]. Available: https://doi.org/10.1063/1.97085

[30] A. W. Snyder and J. D. Love, *Optical Waveguide Theory.*, 1983.

[31] J. C. Travers, W. Chang, J. Nold, N. Joly, and P. S. J. Russell, "Ultrafast nonlinear optics in gas-filled hollow-core photonic crystal fibres," *Journal of the Optical Society of America B*, vol. 23, no. 2, p. A11, 2011.

[32] D. Bird, "Attenuation of model hollow-core, anti-resonant fibres," *Opt. Express*, vol. 25, no. 19, pp. 23 215–23 237, Sep 2017.

[33] L. Vincetti and V. Setti, "Waveguiding mechanism in tube lattice fibers," *Opt. Express*, vol. 18, no. 22, pp. 23 133–23 146, Oct 2010.

[34] W. Belardi and J. C. Knight, "Effect of core boundary curvature on the confinement losses of hollow antiresonant fibers," *Opt. Express*, vol. 21, no. 19, pp. 21 912–21 917, Sep 2013.

[35] F. Yu and J. C. Knight, "Spectral attenuation limits of silica hollow core negative curvature fiber," *Opt. Express*, vol. 21, no. 18, pp. 21 466–21 471, Sep 2013.

[36] M. Schultze, M. Fieß, N. Karpowicz, J. Gagnon, M. Korbman, M. Hofstetter, S. Neppl, A. L. Cavalieri, Y. Komninos, T. Mercouris, C. A. Nicolaides, R. Pazourek, S. Nagele, J. Feist, J. Burgdörfer, A. M. Azzeer, R. Ernstorfer, R. Kienberger, U. Kleineberg, E. Goulielmakis, F. Krausz, and V. S.

Yakovlev, "Delay in photoemission," *Science*, vol. 328, no. 5986, pp. 1658–1662, 2010.

[37] J. M. Dahlström, A. L'Huillier, and A. Maquet, "Introduction to attosecond delays in photoionization," *Journal of Physics B: Atomic, Molecular and Optical Physics*, vol. 45, no. 18, p. 183001, aug 2012.

[38] E. R. Shanblatt, C. L. Porter, D. F. Gardner, G. F. Mancini, R. M. Karl, M. D. Tanksalvala, C. S. Bevis, V. H. Vartanian, H. C. Kapteyn, D. E. Adams, and M. M. Murnane, "Quantitative chemically specific coherent diffractive imaging of reactions at buried interfaces with few nanometer precision," *Nano Letters*, vol. 16, no. 9, pp. 5444–5450, 2016, pMID: 27447192.

[39] A. McPherson, G. Gibson, H. Jara, U. Johann, T. S. Luk, I. A. McIntyre, K. Boyer, and C. K. Rhodes, "Studies of multiphoton production of vacuum-ultraviolet radiation in the rare gases," *J. Opt. Soc. Am. B*, vol. 4, no. 4, pp. 595–601, Apr 1987.

[40] M. Ferray, A. L'Huillier, X. F. Li, L. A. Lompre, G. Mainfray, and C. Manus, "Multiple-harmonic conversion of 1064 nm radiation in rare gases," *Journal of Physics B: Atomic, Molecular and Optical Physics*, vol. 21, no. 3, pp. L31–L35, 1988.

[41] A. L'Huillier, K. J. Schafer, and K. C. Kulander, "Higher-order harmonic generation in xenon at 1064 nm: The role of phase matching," *Phys. Rev. Lett.*, vol. 66, pp. 2200–2203, Apr 1991. [Online]. Available: https://link.aps.org/doi/10.1103/PhysRevLett.66.2200

[42] G. Farkas and C. Tóth, "Proposal for attosecond light pulse generation using laser induced multiple-harmonic conversion processes in rare gases," *Physics Letters A*, vol. 168, no. 5, pp. 447 – 450, 1992.

[43] P. B. Corkum, "Plasma perspective on strong field multiphoton ionization," *Phys. Rev. Lett.*, vol. 71, pp. 1994–1997, Sep 1993. [Online]. Available: https://link.aps.org/doi/10.1103/PhysRevLett.71.1994

[44] M. Lewenstein, P. Balcou, M. Y. Ivanov, A. L'Huillier, and P. B. Corkum, "Theory of high-harmonic generation by low-frequency laser fields," *Phys. Rev. A*, vol. 49, pp. 2117–2132, Mar 1994.

[45] T. Luu, Z. Yin, A. Jain, and et al., "Extreme-ultraviolet high-harmonic generation in liquids." *Nat. Commun.*, vol. 9, p. 3723, 2018.

[46] L. V. Keldysh, "Ionization in the field of a strong electromagnetic wave," *Sov. Phys. JETP*, vol. 20, pp. 1307–1314, 1965.

[47] M. D. Perry, A. Szoke, O. L. Landen, and E. M. Campbell, "Nonresonant multiphoton ionization of noble gases: Theory and experiment," *Phys. Rev. Lett.*, vol. 60, pp. 1270–1273, Mar 1988.

[48] S. Augst, D. Strickland, D. D. Meyerhofer, S. L. Chin, and J. H. Eberly, "Tunneling ionization of noble gases in a high-intensity laser field," *Phys. Rev. Lett.*, vol. 63, pp. 2212–2215, Nov 1989.

[49] H. R. Reiss, "Dipole-approximation magnetic fields in strong laser beams," *Physical Review A*, vol. 63, p. 013409, 2000.

[50] ——, "Limits on tunneling theories of strong-field ionization," *Physical Review Letters*, vol. 1, p. 043002, 2008.

[51] A. L'Huillier, M. Lewenstein, P. Salières, P. Balcou, M. Y. Ivanov, J. Larsson, and C. G. Wahlström, "High-order harmonic-generation cutoff," *Phys. Rev. A*, vol. 48, pp. R3433–R3436, Nov 1993.

[52] M. V. Frolov, N. L. Manakov, and A. F. Starace, "Wavelength scaling of high-harmonic yield: Threshold phenomena and bound state symmetry dependence," *Phys. Rev. Lett.*, vol. 100, p. 173001, 2008.

[53] A. Zaïr, M. Holler, A. Guandalini, F. Schapper, J. Biegert, L. Gallmann, U. Keller, A. S. Wyatt, A. Monmayrant, I. A. Walmsley, E. Cormier, T. Auguste, J. P. Caumes, and P. Salières, "Quantum path interferences in high-order harmonic generation," *Phys. Rev. Lett.*, vol. 100, p. 143902, 2008.

[54] D. Yost, T. Schibli, J. Ye, and et al., "Vacuum-ultraviolet frequency combs from below-threshold harmonics." *Nature Phys*, vol. 5, pp. 815–820, 2009.

[55] K. C. Kulander and B. W. Shore, "Calculations of multiple-harmonic conversion of 1064-nm radiation in xe," *Phys. Rev. Lett.*, vol. 62, pp. 524–526, Jan 1989.

[56] V. C. Reed and K. Burnett, "Loss of harmonic generation in intense laser fields," *Phys. Rev. A*, vol. 46, pp. 424–429, Jul 1992.

[57] P. Eckle, A. N. Pfeiffer, C. Cirelli, A. Staudte, R. Dörner, H. G. Muller, M. Büttiker, and U. Keller, "Attosecond ionization and tunneling delay time measurements in helium," *Science*, vol. 322, pp. 1525–1529, 2008.

[58] U. S. Sainadh, H. Xu, X. Wang, A. A. tul Noor, W. C. Wallace, N. Douguet, A. Bray, I. Ivanov, K. Bartschat, A. Kheifets, R. T. Sang, and I. V. Litvinyuk, "Attosecond angular streaking and tunnelling time in atomic hydrogen," *Nature*, vol. 568, pp. 75–77, 2019.

[59] V. S. Popov, "Tunnel and multiphoton ionization of atoms and ions in a strong laser field (keldysh theory)," *PHYS-USP*, vol. 47, pp. 855–885, 2004.

[60] M. Ammosov, N. Delone, and V. Krainov, "Tunnel ionization of complex atoms and of atomic ions in an alternating electromagnetic field," *Sov. Phys. JETP*, vol. 64, p. 1191, 1986.

[61] X. M. Tong, Z. X. Zhao, and C. D. Lin, "Theory of molecular tunneling ionization," *Phys. Rev. A*, vol. 66, p. 033402, Sep 2002.

[62] C. G. Durfee, A. R. Rundquist, S. Backus, C. Herne, M. M. Murnane, and H. C. Kapteyn, "Phase matching of high-order harmonics in hollow waveguides," *Phys. Rev. Lett.*, vol. 83, pp. 2187–2190, Sep 1999. [Online]. Available: https://link.aps.org/doi/10.1103/PhysRevLett.83.2187

[63] H. J. Lehmeier, W. Leupacher, and A. Penzkofer, "Nonresonant third order hyperpolarizability of rare gases and n_2 determined by third harmonic generation," *Optics Communications*, vol. 56, no. 1, pp. 67–72, 1985.

[64] E. T. F. Rogers, "Modelling of capillary high harmonic generation." Ph.D. dissertation, University of Southampton, 2008.

[65] J. Rothhardt, M. Krebs, S. Hädrich, S. Demmler, J. Limpert, and A. Tünnermann, "Absorption-limited and phase-matched high harmonic generation in the tight focusing regime," *New Journal of Physics*, vol. 16, no. 3, p. 033022, mar 2014.

[66] B. Dromey, M. Zepf, M. Landreman, and S. M. Hooker, "Quasi-phasematching of harmonic generation via multimode beating in waveguides," *Opt. Express*, vol. 15, no. 13, pp. 7894–7900, Jun 2007. [Online]. Available: http://www.opticsexpress.org/abstract.cfm?URI=oe-15-13-7894

[67] H. Ren, A. Nazarkin, J. Nold, and P. S. Russell, "Quasi-phase-matched high harmonic generation in hollow core photonic crystal fibers," *Opt.*

Express, vol. 16, no. 21, pp. 17 052–17 059, Oct 2008. [Online]. Available: http://www.opticsexpress.org/abstract.cfm?URI=oe-16-21-17052

[68] E. A. Gibson, A. Paul, N. Wagner, R. Tobey, D. Gaudiosi, S. Backus, I. P. Christov, A. Aquila, E. M. Gullikson, D. T. Attwood, M. M. Murnane, and H. C. Kapteyn, "Coherent soft x-ray generation in the water window with quasi-phase matching," *Science*, vol. 302, no. 5642, pp. 95–98, 2003. [Online]. Available: https://science.sciencemag.org/content/302/5642/95

[69] M. Zepf, B. Dromey, M. Landreman, P. Foster, and S. M. Hooker, "Bright quasi-phase-matched soft-x-ray harmonic radiation from argon ions," *Phys. Rev. Lett.*, vol. 99, p. 143901, Oct 2007. [Online]. Available: https://link.aps.org/doi/10.1103/PhysRevLett.99.143901

[70] M. Kolesik, J. V. Moloney, and M. Mlejnek, "Unidirectional optical pulse propagation equation," *Phys. Rev. Lett.*, vol. 89, p. 283902, Dec 2002. [Online]. Available: https://link.aps.org/doi/10.1103/PhysRevLett.89.283902

[71] F. Yu and J. C. Knight, "Spectral attenuation limits of silica hollow core negative curvature fiber," *Opt. Express*, vol. 21, no. 18, pp. 21 466–21 471, Sep 2013.

[72] D. A., K. A. E., and B. D. Robert, "The refractive indices and verdet constants of the inert gases," *Proc. R. Soc. Lond. A*, vol. 259, pp. 424–431, 1960.

[73] B. Henke, E. Gullikson, and J. Davis, "X-ray interactions: Photoabsorption, scattering, transmission, and reflection at e = 50-30,000 ev, z = 1-92," *Atomic Data and Nuclear Data Tables*, vol. 54, no. 2, pp. 181–342, 1993.

[74] C. T. Chantler, "Theoretical form factor, attenuation, and scattering tabulation for z=1-92 from e=1-10 ev to e=0.4-1.0 mev," *Journal of Physical and Chemical Reference Data*, vol. 24, no. 1, pp. 71–643, 1995.

[75] ——, "Atomic form factors and photoelectric absorption cross-sections near absorption edges in the soft x-ray region," *AIP Conference Proceedings*, vol. 652, no. 1, pp. 370–377, 2003.

[76] cxro. [Online]. Available: www.cxro.lbl.gov

[77] S. Akira, H. Masatoshi, N. Keigo, and M. Katsumi, "Generation of sub-10-fs, 5-mj-optical pulses using a hollow fiber with a pressure gradient," *Applied Physics Letters*, vol. 86, no. 11, p. 111116, 2005.

[78] W. Wissdorf, D. Müller, Y. Brachthäuser, M. Langner, V. Derpmann, S. Klopotowski, C. Polaczek, H. Kersten, K. Brockmann, and T. Benter, "Gas flow dynamics in inlet capillaries: Evidence for non laminar conditions," *J. Am. Soc. Mass Spectrom.*, vol. 27, no. 9, pp. 1550–1563, 2016.

[79] A. Husakou and J. Herrmann, "Quasi-phase-matched high-harmonic generation in composites of metal nanoparticles and a noble gas," *Phys. Rev. A*, vol. 90, p. 023831, 2014.

[80] E. Constant, D. Garzella, P. Breger, E. Mével, C. Dorrer, C. Le Blanc, F. Salin, and P. Agostini, "Optimizing high harmonic generation in absorbing gases: Model and experiment," *Phys. Rev. Lett.*, vol. 82, pp. 1668–1671, Feb 1999. [Online]. Available: https://link.aps.org/doi/10.1103/PhysRevLett.82.1668

[81] P. Rudawski, C. M. Heyl, F. Brizuela, J. Schwenke, A. Persson, E. Mansten, R. Rakowski, L. Rading, F. Campi, B. Kim, P. Johnsson, and A. L'Huillier, "A high-flux high-order harmonic source," *Review of*

Scientific Instruments, vol. 84, no. 7, p. 073103, 2013. [Online]. Available: https://doi.org/10.1063/1.4812266

[82] J. Brons, V. Pervak, D. Bauer, D. Sutter, O. Pronin, and F. Krausz, "Powerful 100-fs-scale kerr-lens mode-locked thin-disk oscillator," *Opt. Lett.*, vol. 41, no. 15, pp. 3567–3570, Aug 2016. [Online]. Available: http://ol.osa.org/abstract.cfm?URI=ol-41-15-3567

[83] C. Gaida, M. Gebhardt, F. Stutzki, C. Jauregui, J. Limpert, and A. Tünnermann, "Thulium-doped fiber chirped-pulse amplification system with 2 gw of peak power," *Opt. Lett.*, vol. 41, no. 17, pp. 4130–4133, Sep 2016. [Online]. Available: http://ol.osa.org/abstract.cfm?URI=ol-41-17-4130

[84] N. Thiré, R. Maksimenka, B. Kiss, C. Ferchaud, P. Bizouard, E. Cormier, K. Osvay, and N. Forget, "4-w, 100-khz, few-cycle mid-infrared source with sub-100-mrad carrier-envelope phase noise," *Opt. Express*, vol. 25, no. 2, pp. 1505–1514, Jan 2017. [Online]. Available: http://www.opticsexpress.org/abstract.cfm?URI=oe-25-2-1505

[85] F. Lindner, W. Stremme, M. G. Schätzel, F. Grasbon, G. G. Paulus, H. Walther, R. Hartmann, and L. Strüder, "High-order harmonic generation at a repetition rate of 100 khz," *Phys. Rev. A*, vol. 68, p. 013814, Jul 2003. [Online]. Available: https://link.aps.org/doi/10.1103/PhysRevA.68.013814

[86] A. Cabasse, G. Machinet, A. Dubrouil, E. Cormier, and E. Constant, "Optimization and phase matching of fiber-laser-driven high-order harmonic generation at high repetition rate," *Opt. Lett.*, vol. 37, no. 22, pp. 4618–4620, Nov 2012. [Online]. Available: http://ol.osa.org/abstract.cfm?URI=ol-37-22-4618

[87] A. Vernaleken, J. Weitenberg, T. Sartorius, P. Russbueldt, W. Schneider, S. L. Stebbings, M. F. Kling, P. Hommelhoff, H.-D. Hoffmann, R. Poprawe, F. Krausz, T. W. Hänsch, and T. Udem, "Single-pass high-harmonic generation at 20.8 mhz repetition rate," *Opt. Lett.*, vol. 36, no. 17, pp. 3428–3430, Sep 2011. [Online]. Available: http://ol.osa.org/abstract.cfm?URI=ol-36-17-3428

[88] F. Yu and J. C. Knight, "Negative curvature hollow-core optical fiber," *IEEE J. Sel. Topics Quantum Electron.*, vol. 22, p. 4400610, 2016. [Online]. Available: https://doi.org/10.1109/JSTQE.2015.2473140

[89] L. Z. Liu, K. O'Keeffe, and S. M. Hooker, "Quasi-phase-matching of high-order-harmonic generation using multimode polarization beating," *Phys. Rev. A*, vol. 87, p. 023810, Feb 2013. [Online]. Available: https://link.aps.org/doi/10.1103/PhysRevA.87.023810

[90] F. Yu, "Hollow core negative curvature optical fibres," Ph.D. dissertation, University of Bath, 2013.

[91] M. F. Saleh, W. Chang, P. Hölzer, A. Nazarkin, J. C. Travers, N. Y. Joly, P. S. J. Russell, and F. Biancalana, "Theory of photoionization-induced blueshift of ultrashort solitons in gas-filled hollow-core photonic crystal fibers," *Phys. Rev. Lett.*, vol. 107, p. 203902, Nov 2011.

[92] S. C. Rae, K. Burnett, and J. Cooper, "Generation and propagation of high-order harmonics in a rapidly ionizing medium," *Phys. Rev. A*, vol. 50, pp. 3438–3446, Oct 1994.

[93] C. M. Heyl, J. Güdde, A. L'Huillier, and U. Höfer, "High-order harmonic generation with microjoule laser pulses at high repetition rates," *Journal of Physics B: Atomic, Molecular and Optical Physics*, vol. 45, no. 7, p. 074020, mar 2012.

[94] D. Walter, T. Pfeifer, C. Winterfeldt, R. Kemmer, R. Spitzenpfeil, G. Gerber, and C. Spielmann, "Adaptive spatial control of fiber modes and their excitation for high-harmonic generation," *Opt. Express*, vol. 14, no. 8, pp. 3433–3442, Apr 2006.

[95] G. Tejeda, B. Maté, J. M. Fernández-Sánchez, and S. Montero, "Temperature and density mapping of supersonic jet expansions using linear raman spectroscopy," *Phys. Rev. Lett.*, vol. 76, pp. 34–37, Jan 1996.

[96] O. Tcherbakoff, E. Mével, D. Descamps, J. Plumridge, and E. Constant, "Time-gated high-order harmonic generation," *Phys. Rev. A*, vol. 68, p. 043804, 2003.

[97] K. S. Budil, P. Salières, A. L'Huillier, T. Ditmire, and M. D. Perry, "Influence of ellipticity on harmonic generation," *Phys. Rev. A*, vol. 48, pp. R3437–R3440, 1993.

[98] R. Boge, S. Heuser, M. Sabbar, M. Lucchini, L. Gallmann, C. Cirelli, and U. Keller, "Revealing the time-dependent polarization of ultrashort pulses with sub-cycle resolution," *Opt. Express*, vol. 22, no. 22, pp. 26 967–26 975, Nov 2014.

[99] L. Z. Liu, "Polarisation controlled quasi-phase matching of high harmonic generation." Ph.D. dissertation, University of Oxford, 2014.

[100] K. Naganuma, K. Mogi, and H. Yamada, "Time direction determination of asymmetric ultrashort optical pulses from second-harmonic generation autocorrelation signals," *Applied Physics Letters*, vol. 54, no. 13, pp. 1201–1202, 1989.

[101] C. Iaconis and I. A. Walmsley, "Spectral phase interferometry for direct electric-field reconstruction of ultrashort optical pulses," *Opt. Lett.*, vol. 23, no. 10, pp. 792–794, May 1998.

[102] M. Takeda, H. Ina, and S. Kobayashi, "Fourier-transform method of fringe-pattern analysis for computer-based topography and interferometry," *J. Opt. Soc. Am.*, vol. 72, no. 1, pp. 156–160, Jan 1982.

[103] D. Keusters, H.-S. Tan, P. O'Shea, E. Zeek, R. Trebino, and W. S. Warren, "Relative-phase ambiguities in measurements of ultrashort pulses with well-separated multiple frequency components," *J. Opt. Soc. Am. B*, vol. 20, no. 10, pp. 2226–2237, Oct 2003.

[104] D. R. Austin, T. Witting, and I. A. Walmsley, "Resolution of the relative phase ambiguity in spectral shearing interferometry of ultrashort pulses," *Opt. Lett.*, vol. 35, no. 12, pp. 1971–1973, Jun 2010.

[105] C. Manzoni, O. D. Mücke, G. Cirmi, S. Fang, J. Moses, S.-W. Huang, K.-H. Hong, G. Cerullo, and F. X. Kärtner, "Coherent pulse synthesis: towards sub-cycle optical waveforms," *Laser & Photonics Reviews*, vol. 9, no. 2, pp. 129–171, 2015.

[106] C. Bourassin-Bouchet, M. M. Mang, I. Gianani, and I. A. Walmsley, "Mutual interferometric characterization of a pair of independent electric fields," *Opt. Lett.*, vol. 38, no. 24, pp. 5299–5302, Dec 2013.

[107] M. M. Mang, C. Bourassin-Bouchet, and I. A. Walmsley, "Simultaneous spatial characterization of two independent sources of high harmonic radiation." *Opt. Lett.*, vol. 39, p. 6142, 2014.

[108] P. D. Baksh, M. Odstrčil, H.-S. Kim, S. A. Boden, J. G. Frey, and W. S. Brocklesby, "Wide-field broadband extreme ultraviolet transmission pty-

chography using a high-harmonic source," *Opt. Lett.*, vol. 41, no. 7, pp. 1317–1320, 2016.

[109] C. L. Porter, M. Tanksalvala, M. Gerrity, G. Miley, X. Zhang, C. Bevis, E. Shanblatt, R. Karl, M. M. Murnane, D. E. Adams, and H. C. Kapteyn, "General-purpose, wide field-of-view reflection imaging with a tabletop 13 nm light source," *Optica*, vol. 4, no. 12, pp. 1552–1557, 2017.

[110] C. J. Saraceno, F. Emaury, O. H. Heckl, C. R. E. Baer, M. Hoffmann, C. Schriber, M. Golling, T. Südmeyer, and U. Keller, "275 w average output power from a femtosecond thin disk oscillator operated in a vacuum environment," *Opt. Express*, vol. 20, no. 21, pp. 23 535–23 541, Oct 2012.

[111] F. Emaury, A. Diebold, C. J. Saraceno, and U. Keller, "Compact extreme ultraviolet source at megahertz pulse repetition rate with a low-noise ultrafast thin-disk laser oscillator," *Optica*, vol. 2, no. 11, pp. 980–984, Nov 2015.

[112] A. D. Shiner, C. Trallero-Herrero, N. Kajumba, H.-C. Bandulet, D. Comtois, F. Légaré, M. Giguère, J.-C. Kieffer, P. B. Corkum, and D. M. Villeneuve, "Wavelength scaling of high harmonic generation efficiency," *Phys. Rev. Lett.*, vol. 103, p. 073902, Aug 2009.

[113] F. Köttig, F. Tani, C. M. Biersach, J. C. Travers, and P. S. Russell, "Generation of microjoule pulses in the deep ultraviolet at megahertz repetition rates," *Optica*, vol. 4, no. 10, pp. 1272–1276, Oct 2017.

[114] M. Gebhardt, C. Gaida, T. Heuermann, F. Stutzki, C. Jauregui, J. Antonio-Lopez, A. Schulzgen, R. Amezcua-Correa, J. Limpert, and A. Tünnermann, "Nonlinear pulse compression to 43 w gw-class few-cycle pulses at 2 micrometre wavelength," *Opt. Lett.*, vol. 42, no. 20, pp. 4179–4182, Oct 2017.

[115] P. Jaworski, F. Yu, R. R. Maier, W. J. Wadsworth, J. C. Knight, J. D. Shephard, and D. P. Hand, "Picosecond and nanosecond pulse delivery through a hollow-core negative curvature fiber for micro-machining applications," *Opt. Express*, vol. 21, no. 19, pp. 22 742–22 753, Sep 2013.

[116] Y. Mairesse, O. Gobert, P. Breger, H. Merdji, P. Meynadier, P. Monchicourt, M. Perdrix, P. Salières, and B. Carré, "High harmonic xuv spectral phase interferometry for direct electric-field reconstruction," *Phys. Rev. Lett.*, vol. 94, p. 173903, 2005.

[117] O. Pedatzur, A. Trabattoni, B. Leshem, and et al., "Double-blind holography of attosecond pulses," *Nature Photon*, vol. 13, pp. 91–95, 2019.

[118] S. Fuchs, M. Wünsche, J. Nathanael, J. J. Abel, C. Rödel, J. Biedermann, J. Reinhard, U. Hübner, and G. G. Paulus, "Optical coherence tomography with nanoscale axial resolution using a laser-driven high-harmonic source," *Optica*, vol. 4, no. 8, pp. 903–906, 2017.

[119] D. Popmintchev, C. Hernández-García, F. Dollar, C. Mancuso, J. A. Pérez-Hernández, M.-C. Chen, A. Hankla, X. Gao, B. Shim, A. L. Gaeta, M. Tarazkar, D. A. Romanov, R. J. Levis, J. A. Gaffney, M. Foord, S. B. Libby, A. Jaron-Becker, A. Becker, L. Plaja, M. M. Murnane, H. C. Kapteyn, and T. Popmintchev, "Ultraviolet surprise: Efficient soft x-ray high-harmonic generation in multiply ionized plasmas," *Science*, vol. 350, no. 6265, pp. 1225–1231, 2015.

[120] J. M. Rodenburg, *Advances in Imaging and Electron Physics*, 2008, vol. 150.